4.7 Gas system

The gas system is developed for stable controlling of a gas pressure and monitoring a gas pressure and a its purity in the chamber. As discussion in Subsection 4.7.1, gas purity is critical for the systematic uncertainties. Thus, all connections are using VCR and assembling of the system is done in CLASS 1000 clean room. The acceptable leak rate of welding points of the system is 4.0×10^{-10} Pa $\cdot$ m^3/s. Krypton gas is transferred from the system to the gas chamber by flexible metal tube of the length is 5 m and the thickness is 1/4 inch.

4.7.1 Gas sampling

In order to avoid chemical reactions and depolarizing collisions, we should carefully take care of the purity of Krypton gas. Especially, the cross section for a muonium $-$ O^2 depolarizing electron spin exchange collision is very large ($\approx 5 \times 10^{-16}$ cm^{-2}) (see Table 4.7). The muon polarization P can be determined from the angular distribution

molecule	interaction	σ at 0.52 T (unit = 10^{-16} cm^2)	σ_{SE} (unit = 10^{-16} cm^2)
NO_2	$NO_2 + M \rightarrow NO + OM$	≤ 23	$\cdots$
O_2	Spin exchange	5.4(3)	5.9(6)
NO	Spin exchange	3.2(2)	7.1(1)
C_2H_4	$C_2H_4 + M \rightarrow C_2H_4M$	0.29(16)	$\cdots$
H_2, N_2, SF_6	$\cdots$	≥ 0.01	$\cdots$

Table 4.7: Muonium (M)-molecule cross sections [11, 12].

of the decay positrons and is assumed to vary with time t as

$$P(t) = P_0 \exp(-\lambda_2 t), \tag{4.7}$$

where P_0 is the initial polarization of the muons which form muonium. If the collision depolarization mechanism is an electron-spin exchange process, as is expected for a paramagnetic molecule, then the theory of the muon depolarization can be given in

terms of a density matrix formulation of the equations for the populations of the four HFS levels. The dependence of λ_2 on H is found to be

$$\lambda_2 = \lambda_{20}/(1+x^2)^{\frac{1}{2}}, \tag{4.8}$$

in which λ_{20} is the depolarization rate for $H = 0$. λ_{20} of collision with oxygen is measured as [12]

$$\lambda_{20}/n \approx 3 \times 10^{-16}\mathrm{cm}^3/\mu\mathrm{s}, \tag{4.9}$$

where n is the number of interacting molecules per cm^3. This equation suggests that the effect of contamination is maximum in zero field experiment. Assuming a 1 ppm contamination of oxygen in 1 atm krypton gas, λ_2 at zero field is calculated as

$$\lambda_2 \approx 8.1 \times 10^3 \ /\mathrm{s} \tag{4.10}$$

A figure 4.59 shows a P_0 dependence on oxygen contamination. As shown in this figure, the contamination of oxygen should be less than a ppm.

The gas system has 6 sampling bottles which can be release independently from the system during a measurement. By measurement of sampling gas using a Q-mass (quadrupole mass spectroscopy), purity of the gas can be measured at the level of ppm. Requirement of a gas purity is discussed in Subsection 4.7.1.

4.7.2 Pressure guage

The transition frequencies of muonium measured in a gas vary with the gas density due to the distortion of the muonium wavefunction in collision. At a constant temperature, two-body collisions between a muonium atom and a krypton atom cause a shift which is proportional to the krypton pressure at fixed volume [60]. Also three-body interaction between muonium atom and two krypton atoms yield a shift proportional to the square to the krypton pressure at fixed volume [61]. The shift in the transition frequency is described as

$$\nu_{ij}(P) = \nu_{ij}(0)(1 + a_{ij}P + b_{ij}P^2). \tag{4.11}$$

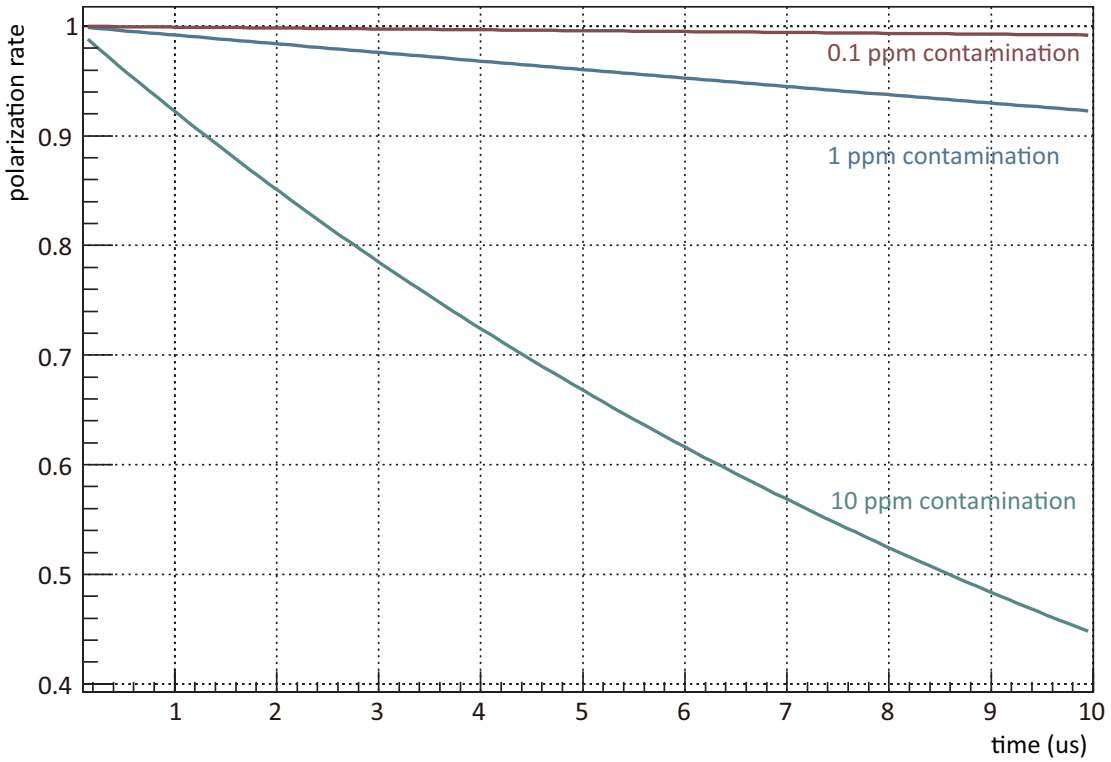

Figure 4.59: A P_0 dependence on oxygen contamination. The contamination of oxygen should be less than a ppm.

b is obtained by earlier experiment at LAMPF [62] as

$$b = (9.7 \pm 2.0) \times 10^{-14}\ \mathrm{Torr}^{-2}. \tag{4.12}$$

a is also obtained by latest experiment at LAMPF [4] as

$$a_{12} = -8.669(26) \times 10^{-6}\ \mathrm{atm}^{-1}, \tag{4.13}$$

$$a_{34} = -7.665(25) \times 10^{-6}\ \mathrm{atm}^{-1}. \tag{4.14}$$

Gas pressure is measured by the capacitance gauge (M-342DG-13). It has a measuring range of 1.33 kPa with an uncertainty of 0.20 % of reading. Moreover, the silicon gauge (RPM4-AD) is also plan to use. It has a measuring range of 1.6 kPa with an uncertainty of 0.020 % of reading.

The uncertainty from a gas pressure is described in Section 5.6.

4.7.3 Relief valve

Low-Pressure Proportional Relief Valve is prepared for safety. Maximum working pressure is 0.2 MPa.

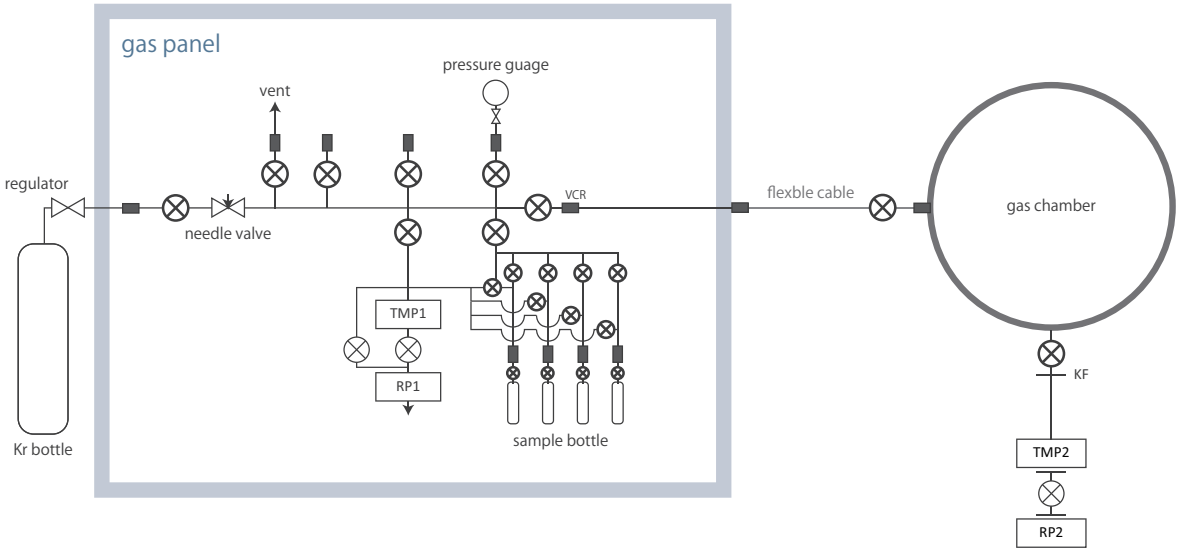

Figure 4.60: A diagram of the gas system.

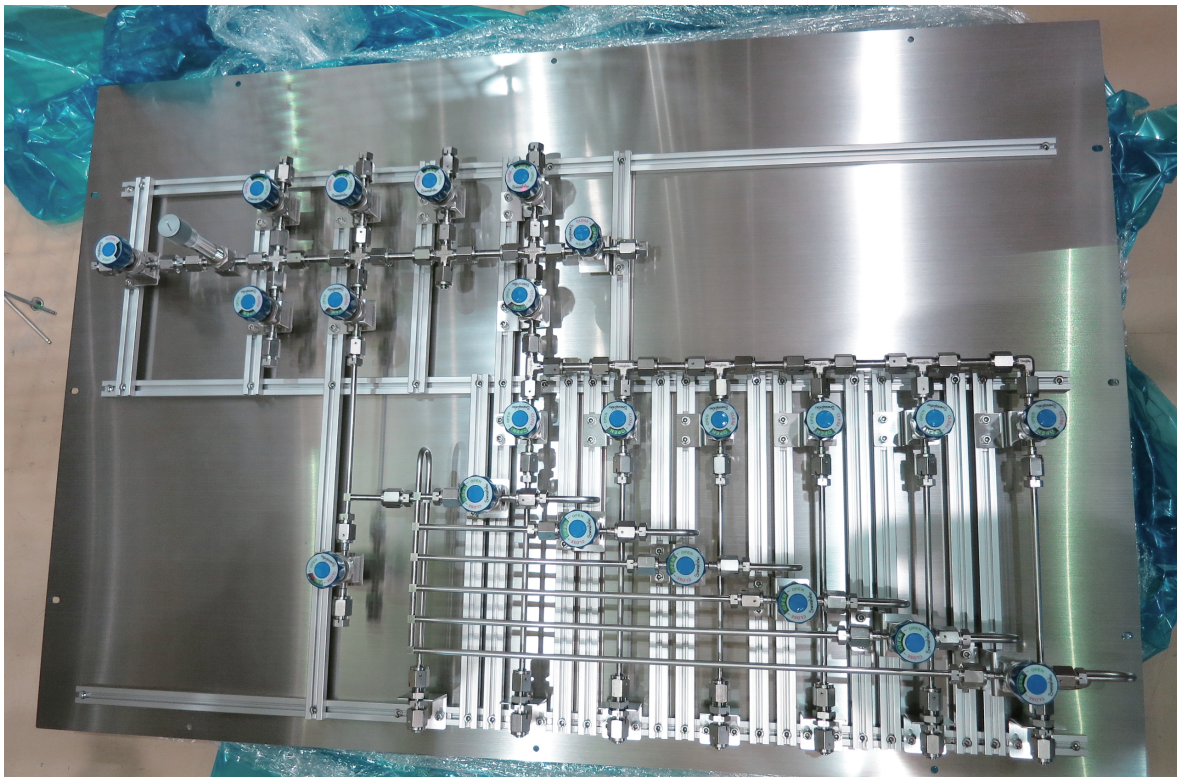

Figure 4.61: A photo of the gas system.

4.8 Magnetic shield for zero field

4.8.1 Measurement of the magnetic field in D2 area

For zero field experiment, a magnetic field in the cavity should be less than 100 nT. Figure 4.62 shows a measurement result of a magnetic field in case of magnet on and off in the experimental area of D Line (D2 area). Magnetic fields in the experimental area are coming from earth magnetism, magnetized poles under the base plate and quadrupole magnets to guide the muon beam. There is decay component of the magnetic field with a height from the base which is caused by the magnetized poles under the base plate as shown in Figure 4.63. From these measurement values, the magnetic field in the area is reproduced by simulations using TRICOMP (Figure 4.64, 4.65).1

4.8.2 structure of magnetic shield

Figure 4.66 shows a schematic view of the magnetic shield with other apparatus. The magnetic shield is composed of 3 layers of 1.5 mmt boxes made of permalloy. Figure 4.67 shows apertures of the shield. These apertures are located symmetrically to care about homogeneity of magnetic field in the shield.

4.8.3 simulation of magnetic shield

Simulation of the effect of apertures of magnetic shield

Figure 4.68 shows a comparison of magnetic fields in the shield between different diameters of the front window of the shield. Compared to the case of 20 cm, Leakage magnetic field from the front window in the case of the diameters are down to 14 cm are negligible compared with the exude magnetic field from plates of the shield.

Simulation of the effect of thickness of the plates

Figure 4.69 shows a comparison of magnetic fields in the shield between different thicknesses of plates of the shield. In this simulation, the relative permeability of the plates

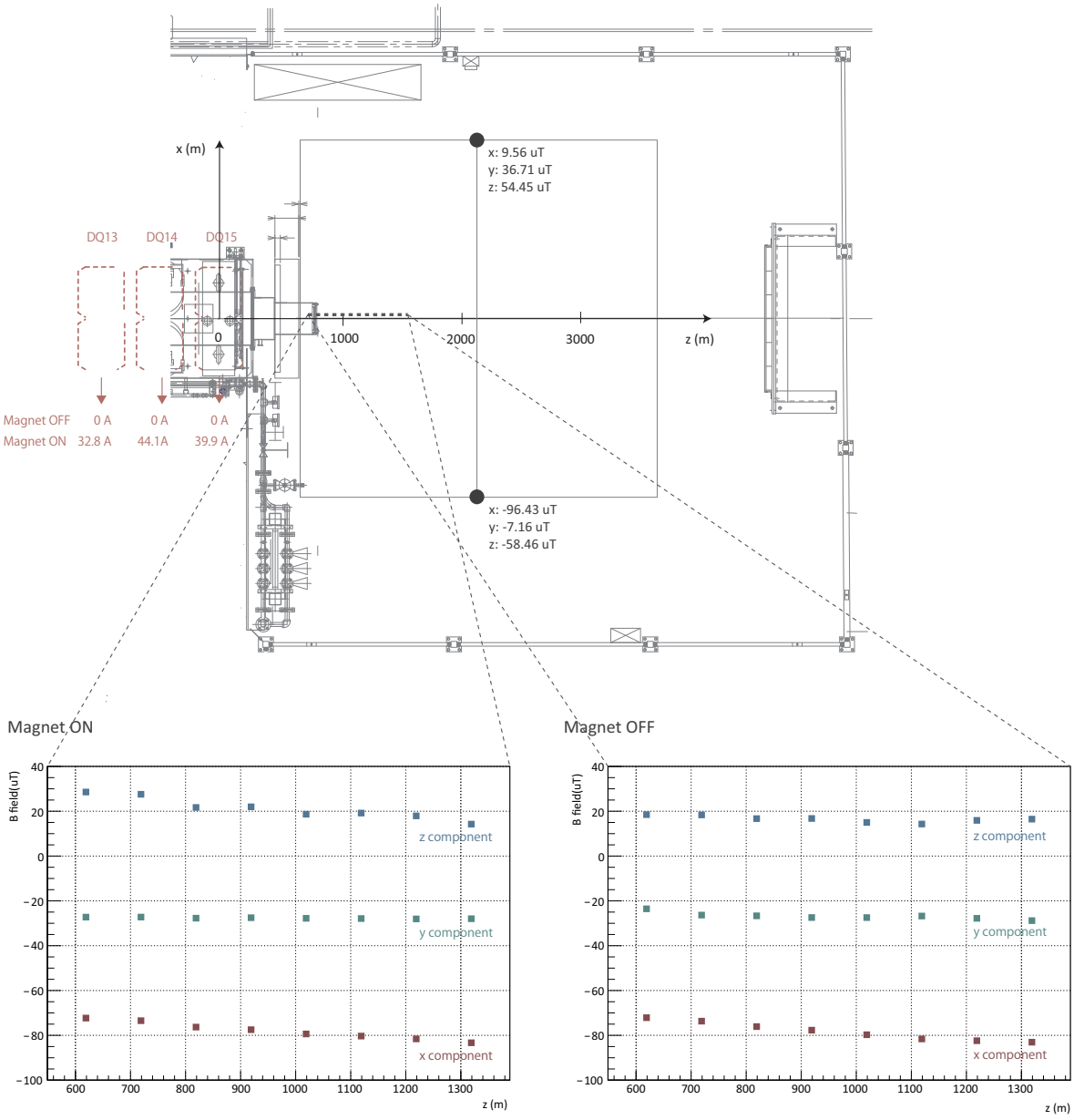

Figure 4.62: Measurement of the magnetic field at D2 area. A left figure shows the magnetic field on beam axis in case magnet on, a right figure shows the magnetic field in case magnet off.

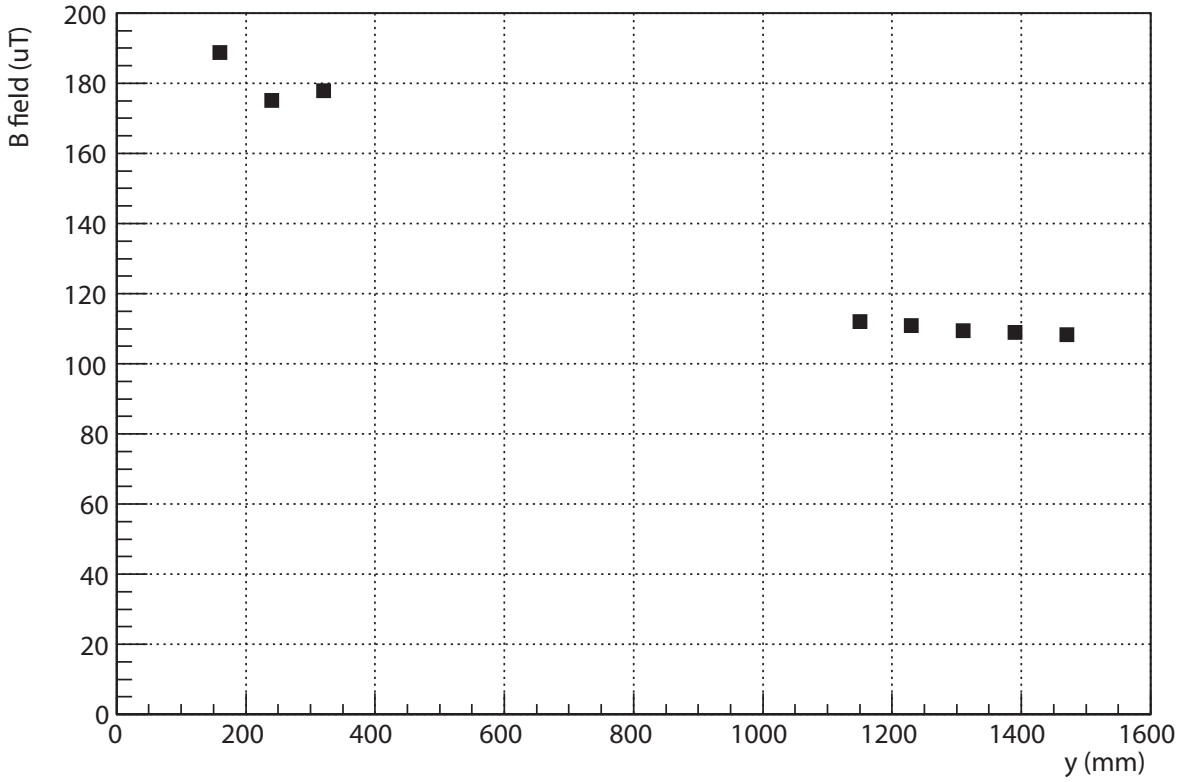

Figure 4.63: The magnetic field at D2 area in the direction of y axis. the origin of the y is defined as a position of the surface of the base plate.

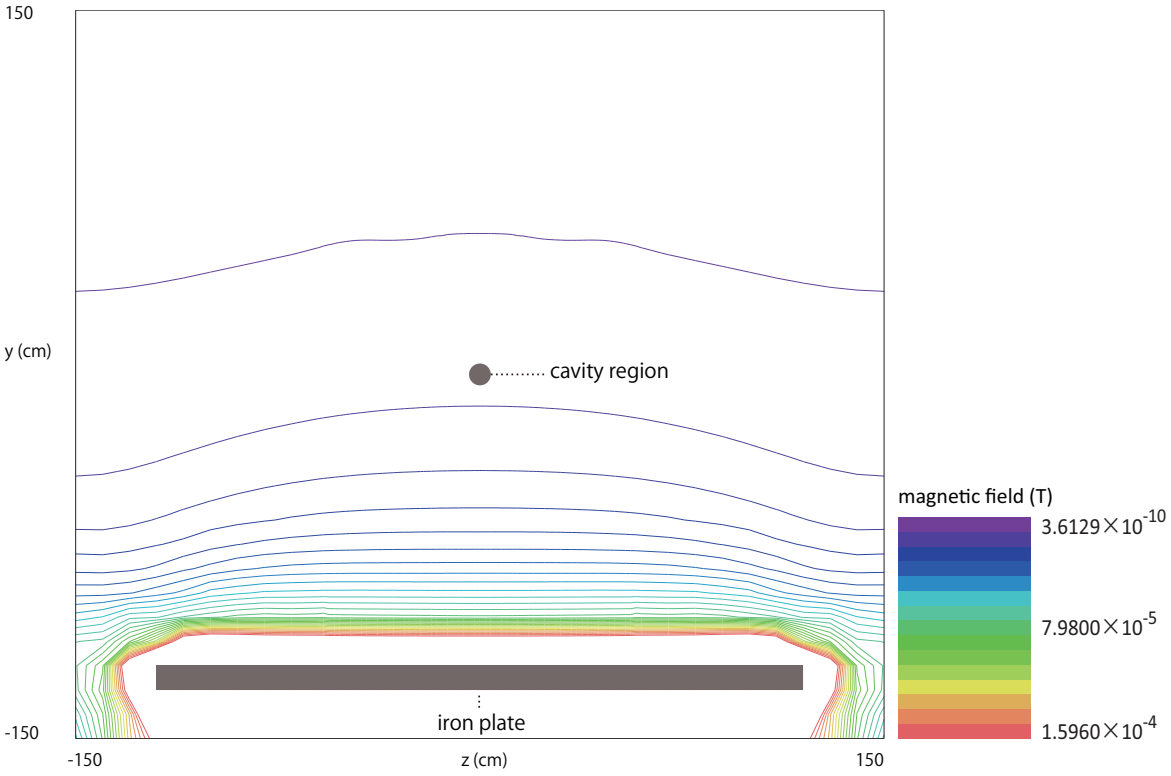

Figure 4.64: A xy cross sectional view of the magnetic field in D2 area generated by simulation. Magnetized poles generate the magnetic field depend on the height from the base plate.

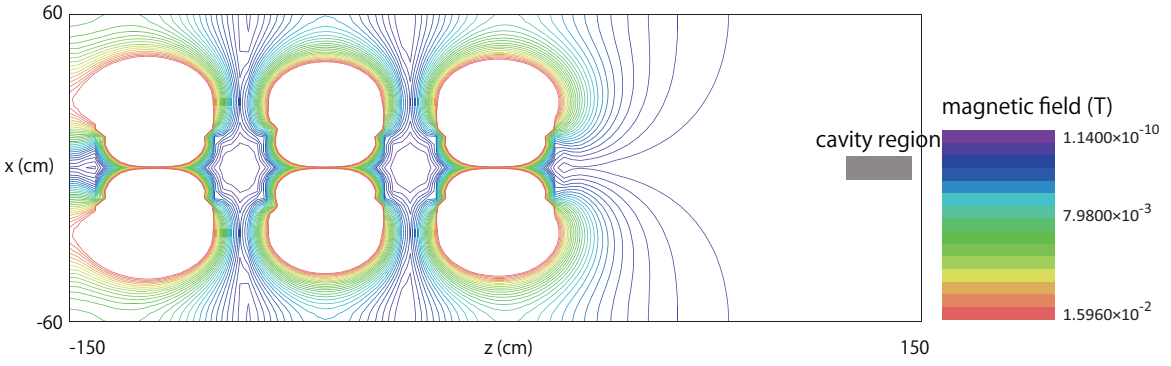

Figure 4.65: A xz cross sectional view of the magnetic field in D2 area generated by simulation. Quadratic magnets generate the magnetic field to guide the muon beam.

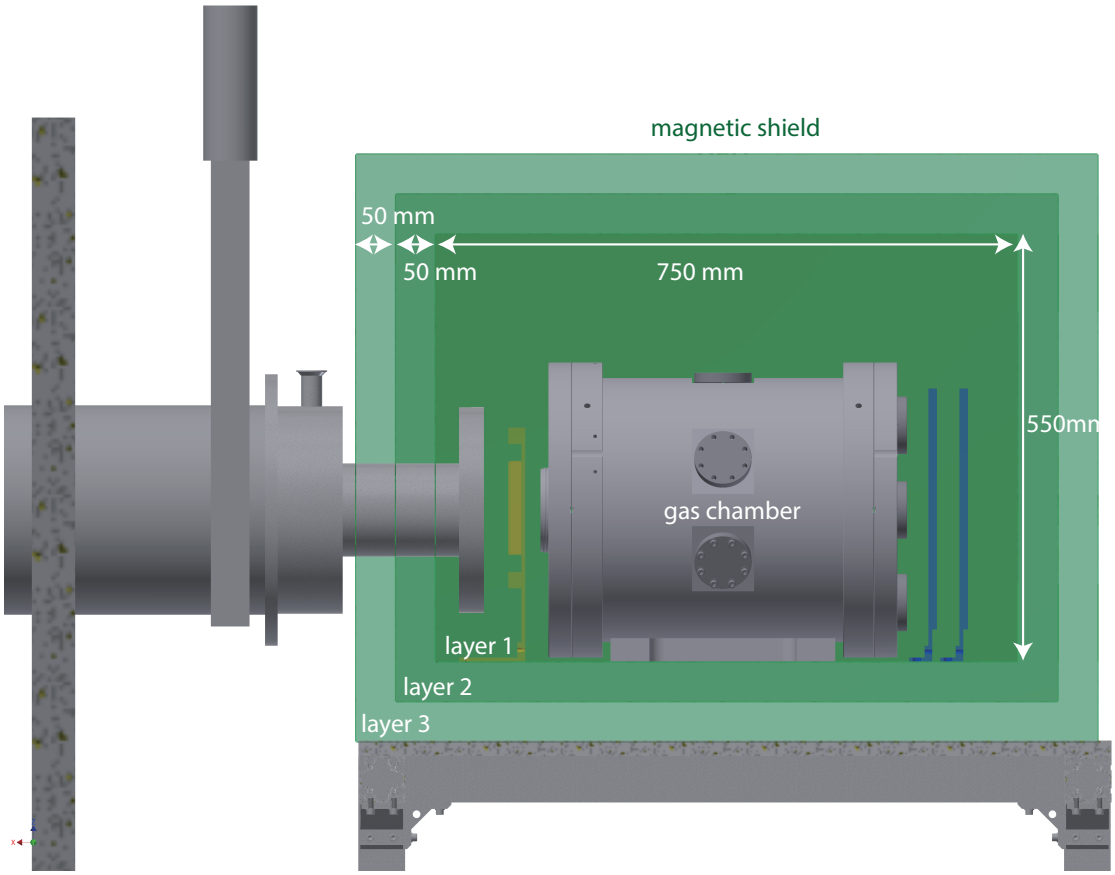

Figure 4.66: A schematic view of the magnetic shield surrounding the gas chamber. The magnetic shield is composed of 3 layers of 1.5 mmt boxes made of permalloy.

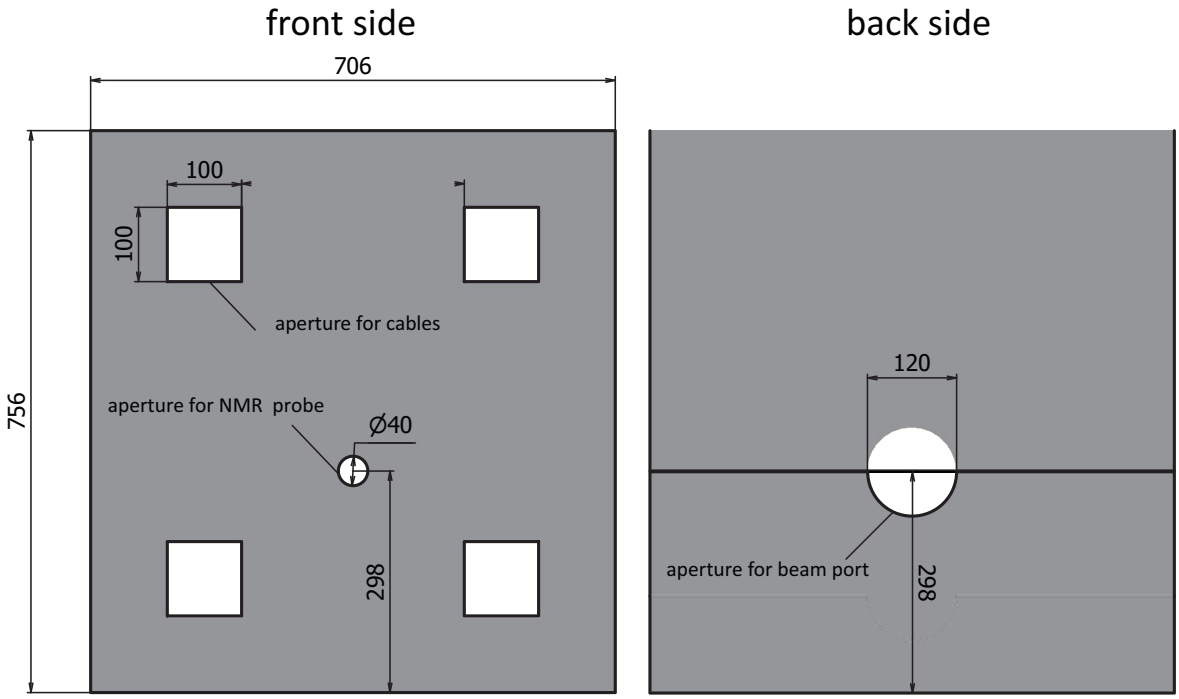

Figure 4.67: Drawings of front panels and a back panel of layer 3. Front panels are separated to upper part and lower part to install the beam duct extension after an installation of the magnetic shield.

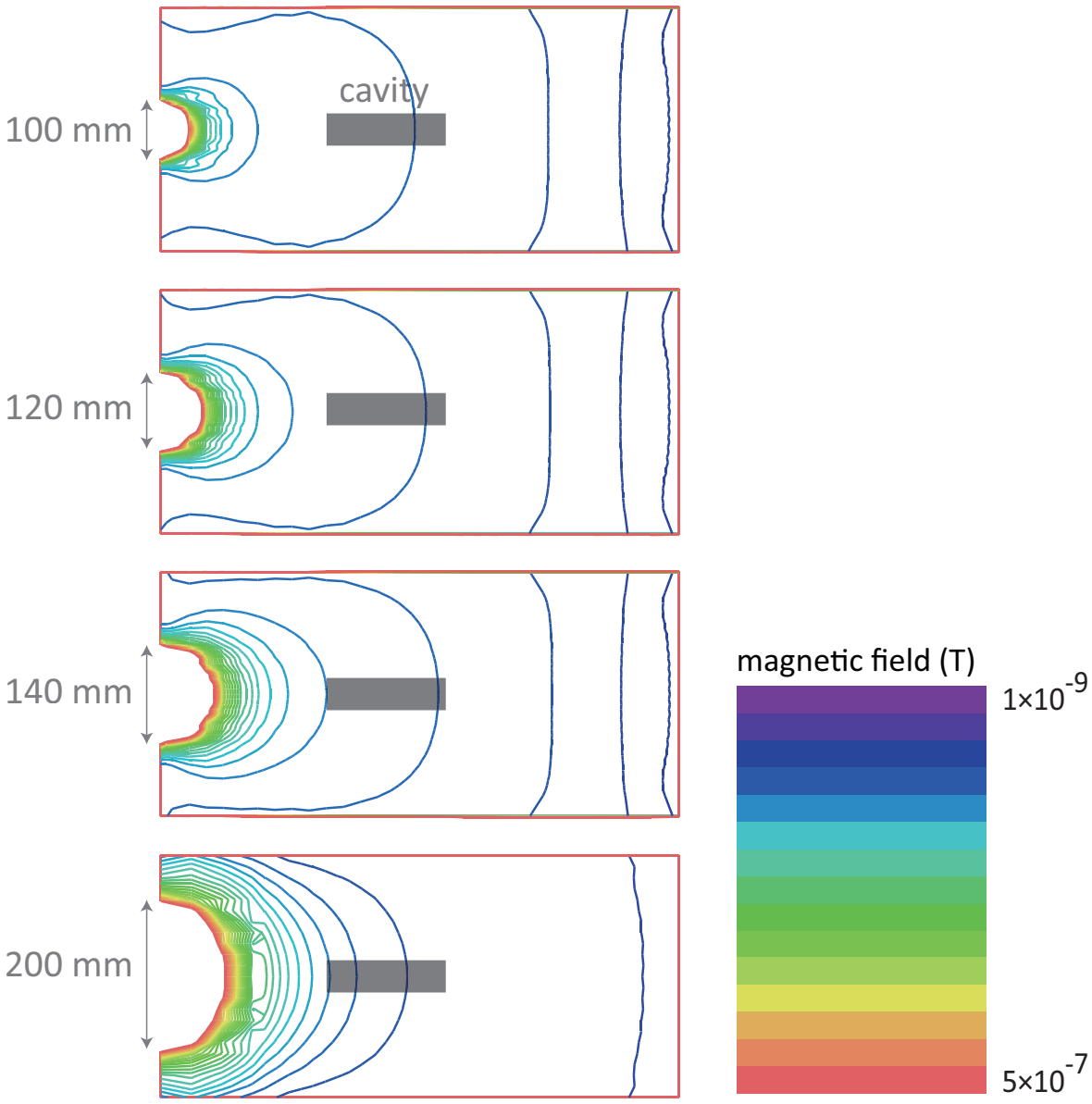

Figure 4.68: A comparison of different diameter of the front window of the magnetic shield. The magnetic shield is composed of 3 layers of 1.5 mmt boxes made of permalloy. In case that the diameter is from 100 mm to 140 mm, a leakage field in the cavity region from the front side is not dominant compared from other sides.

is set to 12000. From this simulation, 1.5 mmt is enough to achieve under 1 mG magnetic field in the shield.

4.8.4 Performance test for the magnetic shield

Performance test for the magnetic shield was held at S1 area. Figure 4.70 shows a setup of the test. Mounting bases for the magnetic shield and the magnetic probe system are installed at the S1 area. The magnetic probe can move independently from the magnetic shield in the range of the length of the shield (750 mm). First, Magnetic fields on the beam axis without the magnetic shield are measured (Figure 4.71). Then the magnetic shield is assembled on the mounting base, and magnetic field with the shield was measured. As shown in this figure, the magnetic field is suppressed at the level of mG in the magnetic shield.

System for a magnetic field scan

Figure 4.72 shows a schematic view of the system for magnetic field scan. The edge of the support rod can be attached and removed two different probe holders, for scan on axis and on cylinder surface.

Mechanism of a magnetic probe A magnetic probe for the measurement is used fluxgate magnetometer for 3 axis (MTI FM-3500). The linearity of the probe is 5 nT (0.5% of F.S.) and the precision is 0.5 nT for each axis. Fluxgate measures a magnetic field on a single axis by using a non-linear response of high-permeability material. Figure 4.73 shows a typical mechanism of a fluxgate. A relation between a magnetization ($M(H)$) and a magnetic field (H) can be expressed as

$$M(H) = \chi_1 H + \chi_2 H^2 + \chi_3 H^3. \tag{4.15}$$

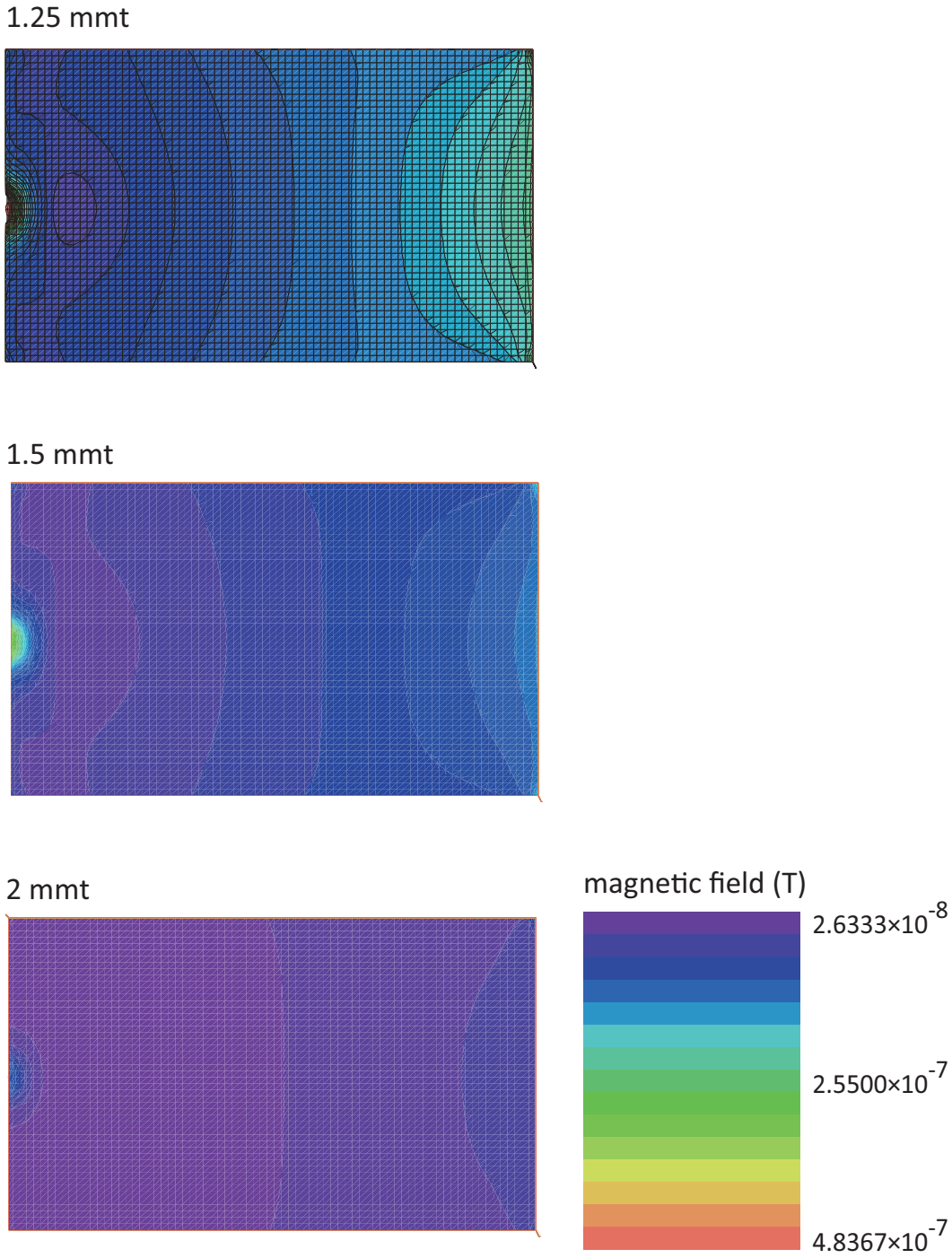

Figure 4.69: A comparison of magnetic fields in the shield between different thicknesses of plates of the shield. In this simulation, the relative permeability of the plates is set to 12000.

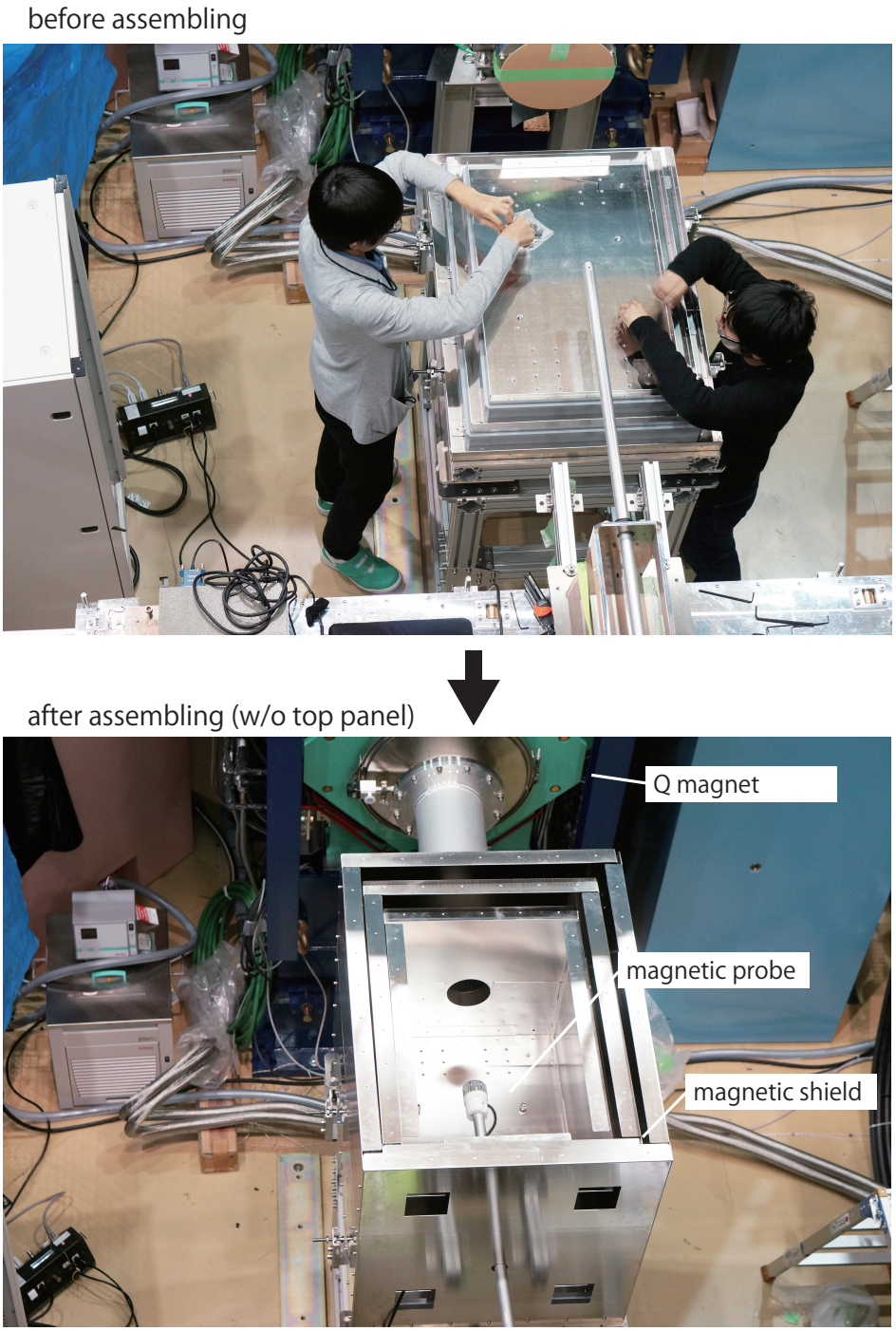

Figure 4.70: A photo of the installation of the magnetic shield and the system for magnetic field scan. Magnetic probes are inserted from the ϕ40 hole on back panels.

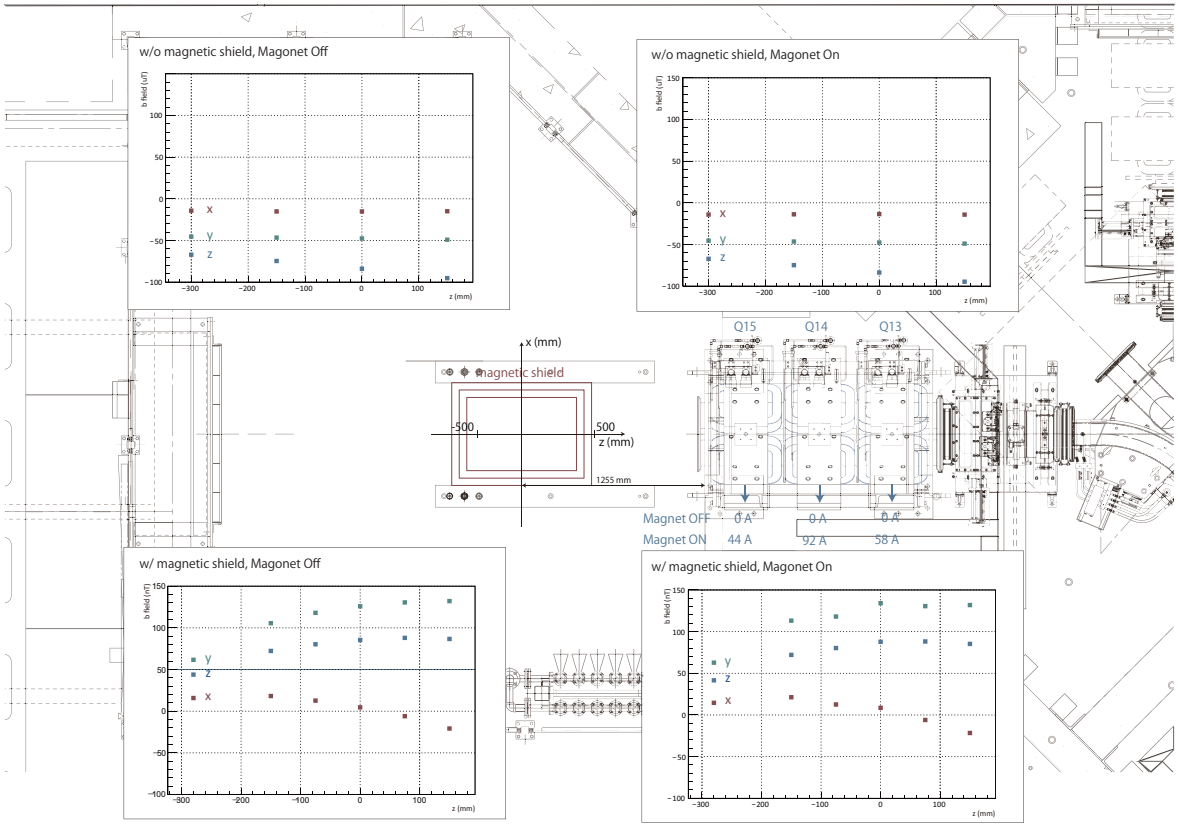

Figure 4.71: A result of the performance test of magnetic shield in S1 area. There is little variation of magnetic fields between magnet on and magnet off. The magnetic shield reduces the external field about one-thousandth.

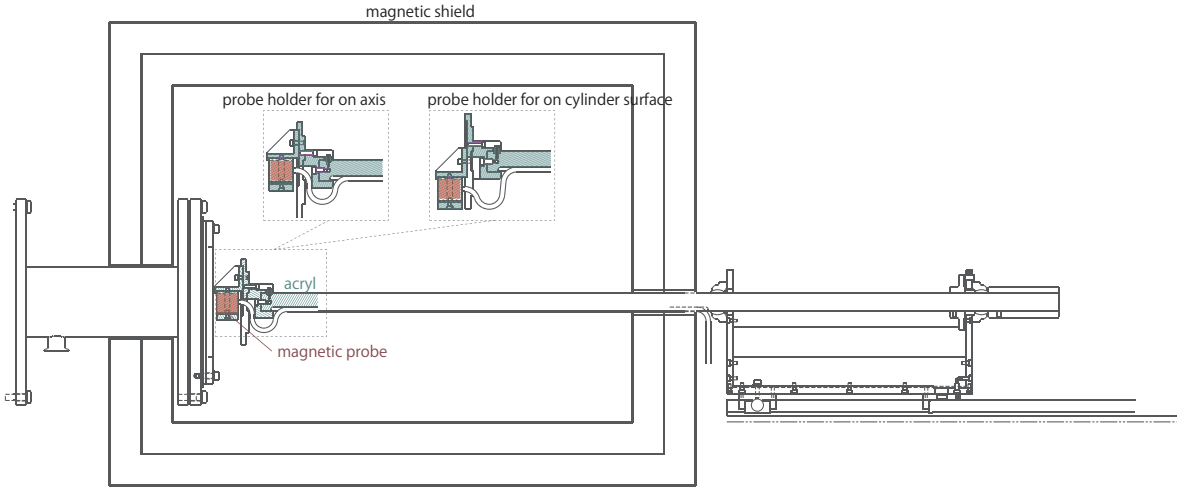

Figure 4.72: A schematic view of the system for magnetic field scan. The edge of the support rod can be attached and removed two different probe holders, for scan on axis and on cylinder surface.

Then the induced electromotive force (E) of 2nd coil from an external magnetic field (H_0) and a magnetic field of 1st coil (H_1) is

$$E = \frac{\mathrm{d}(M(H_0+H_1)+M(H_0-H_1))}{\mathrm{d}t} \tag{4.16}$$

$$= \frac{\mathrm{d}2(\chi_1 H_0+\chi_2 H_0^2+\chi_3 H_0^3+(\chi_1+3\chi_3 H_0)H_1^2)}{\mathrm{d}t} \tag{4.17}$$

$$= 4A(\chi_1+3\chi_3 H_0)\sin(2\omega t). \tag{4.18}$$

If

$$H_1 = A\sin(\omega t), \tag{4.19}$$

then

$$E = C_0\cos(\omega t)+3\chi_3 H_0\sin(2\omega t)+3\chi\sin(\omega t)^2\cos(\omega t). \tag{4.20}$$

By detecting a second order oscillation in 2nd term of the equation, the strength of the external magnetic field H_0 can be obtained.

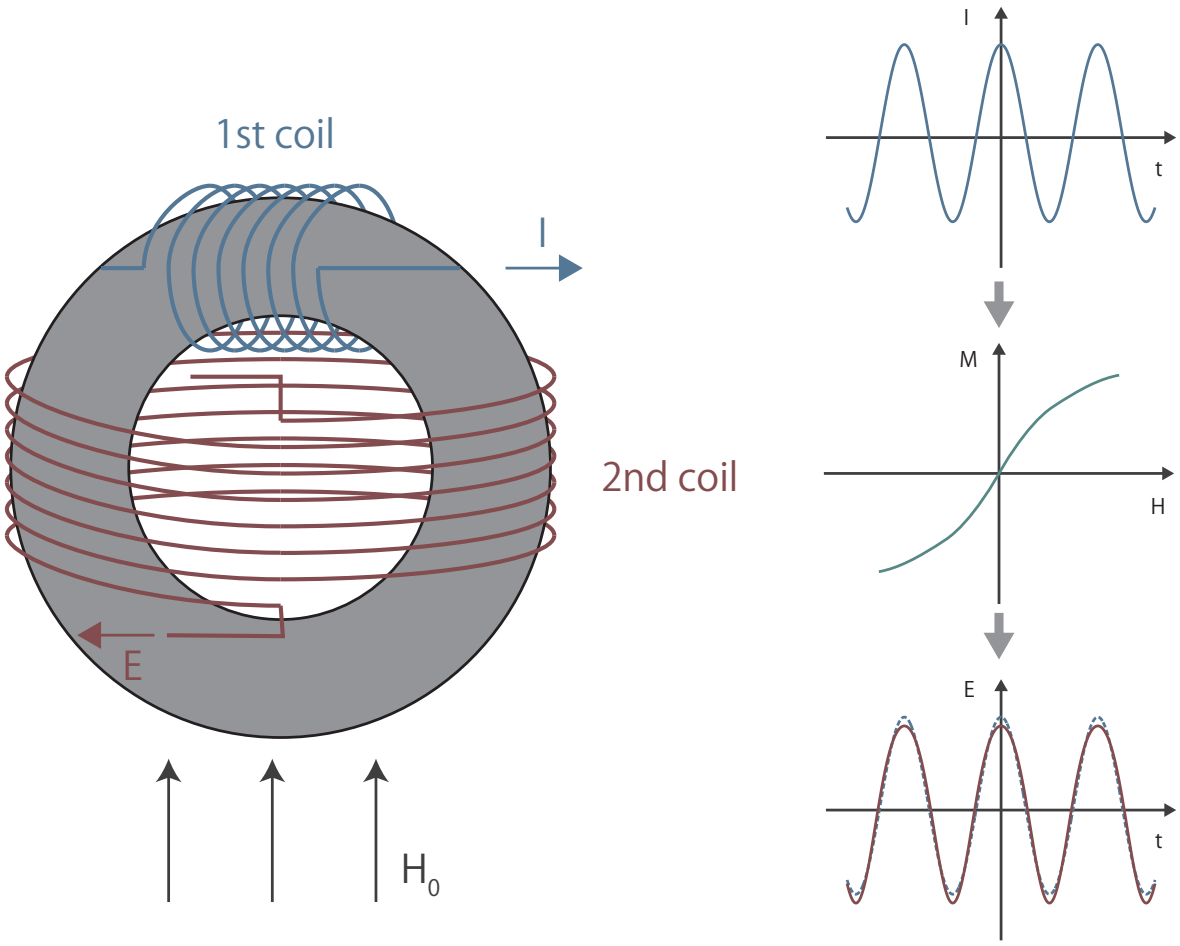

Figure 4.73: A typical mechanism of a fluxgate magnetometer. A fluxgate measures a magnetic field on a single axis by using a non-linear response of high-permeability material.

4.9 Data acquisition system

4.9.1 Data acquisition system for environmental monitoring

Figure 4.74 shows a schematic diagram of the monitoring system for RF system, gas system and magnetometers. These values are taken every minutes and recorded using a Labview software.

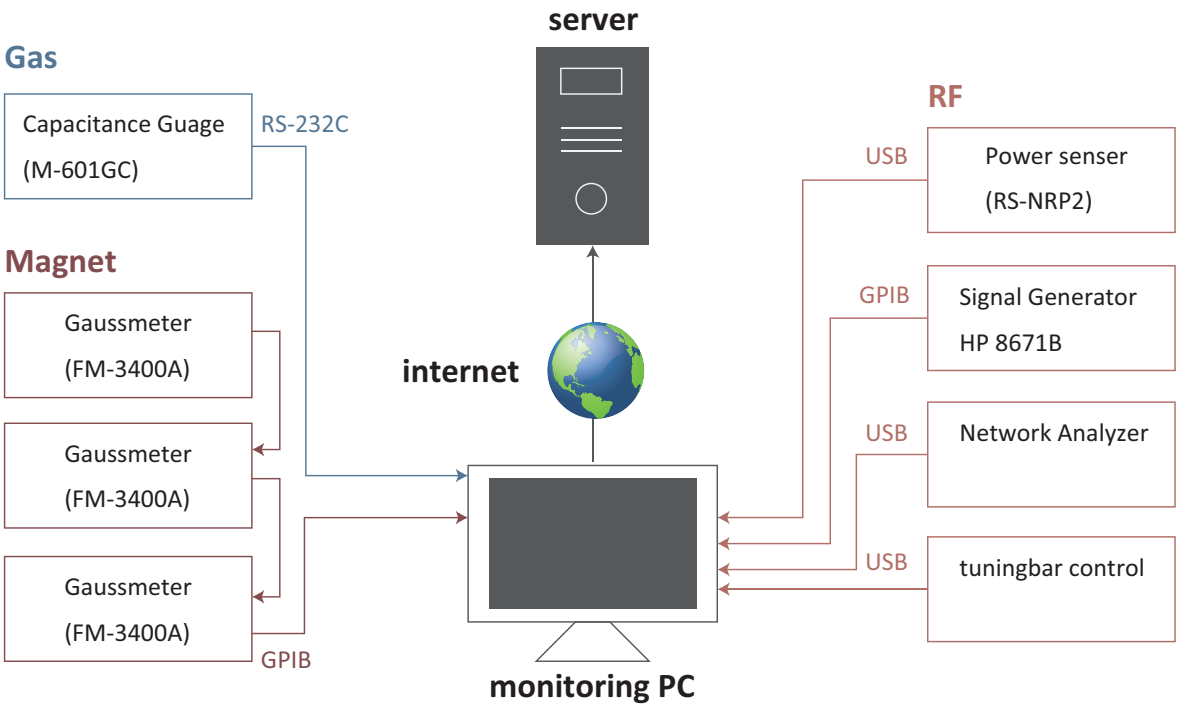

Figure 4.74: A schematic diagram of the monitoring system for RF system, gas system and magnetometers. These values are taken every minutes and recorded using a Labview software.

4.9.2 Data acquisition system for detectors

Data aquision system for detectors is developed by S. Kanda and others. Signals from positron detectors are read by Kalliope (KEK Advanced Liner and Logic board Integrated Optical detector for Positron and Electron) developed by the Electronics

Group and Institute of Material Structure Science (IMSS) of KEK[63]. Data of multi-hit TDC is transferred to the computer by Ethernet.

4.10 Beam monitoring system

Systematic uncertainties from a RF field and a magnetic field are able to be suppressed by analysis by using a field maps and muonium distributions from two different beam monitors.

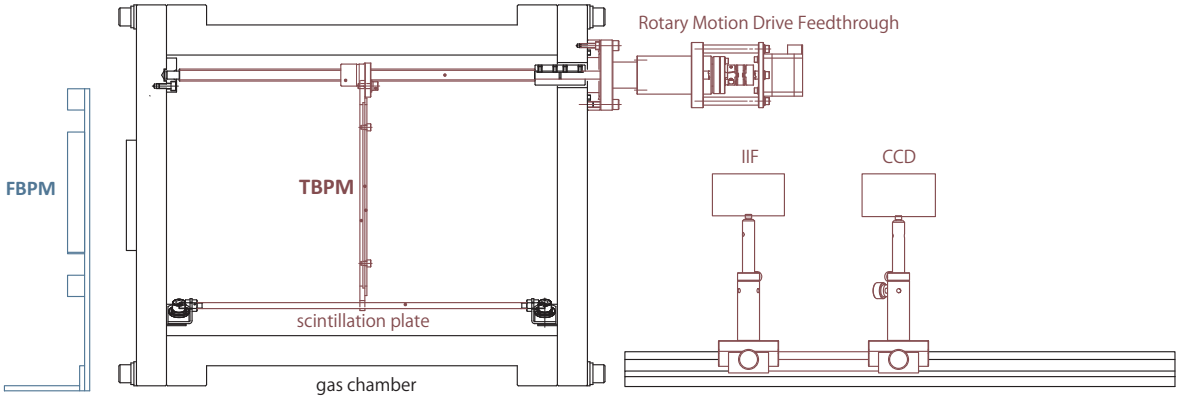

Figure 4.75: A schematic drawing of a beam monitoring system. Before a measurement, 3 dimensional muon stopping distributions in a certain gas pressure are taken by using a TBPM. Fluctuations of distributions are monitored by FBPM during a measurement.

FBPM

2–dimensional muon distribution is measured by a front beam profile monitor (FBPM) simultaneously for monitoring the stability of beam profile and relatively beam intensity during every data taking time developed by S. Kanda and others [91]. FBPM is composed of 2 layers of scintillation fiber arrays. The thickness of the fiber is 100 μm which allow the passage of muons. The detection area is 100 mm $\times$ 100 mm which cover the three standard deviation range of the muon beam.

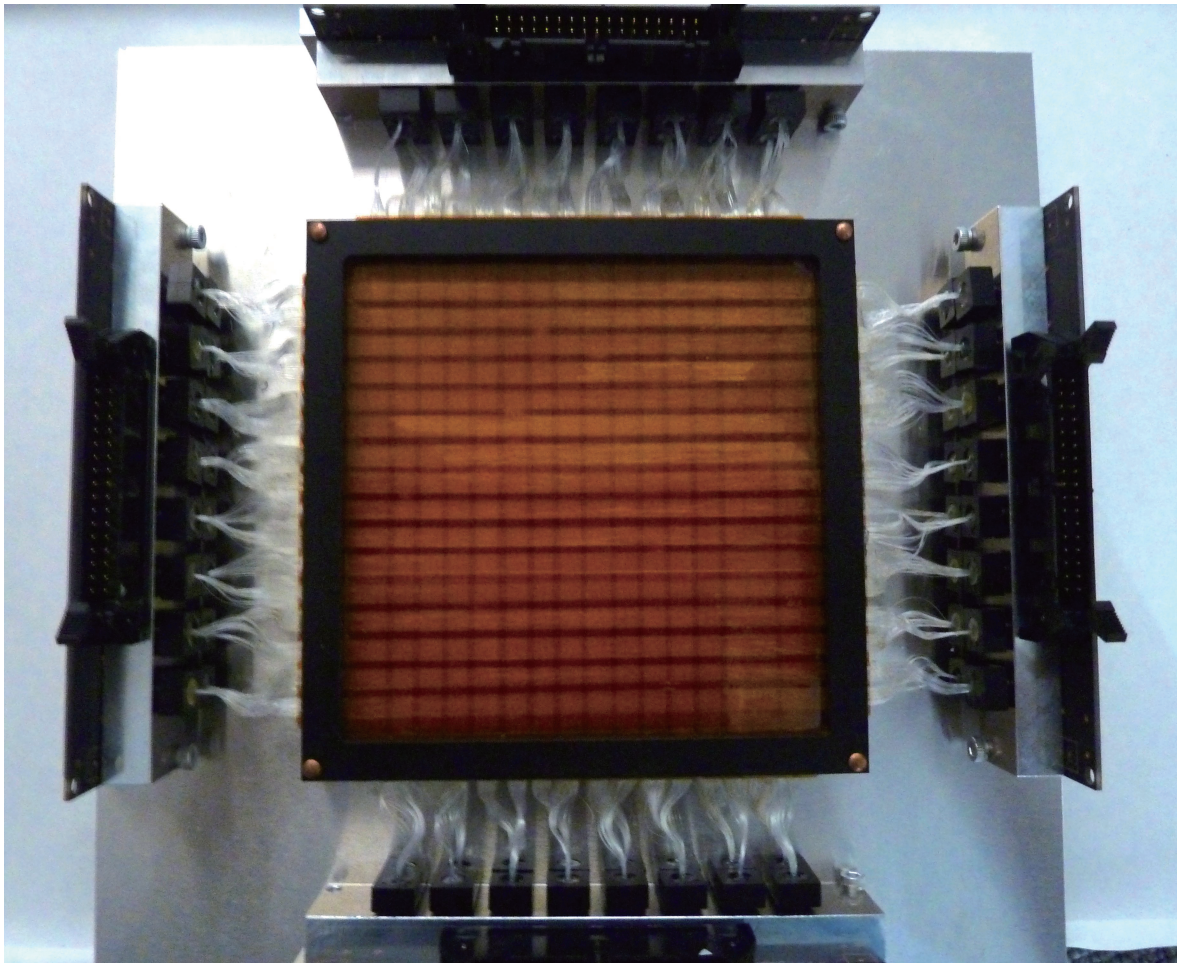

Figure 4.76: A photograph of FBPM.

TBPM

Before taking data, the 3-dimensional muon stopping distribution in the gas chamber is measured by a target beam profile monitor (TBPM) developed by S. Kanda, Y. Ueno and others[64]. Muons pass through in the chamber stop at the scintillation plate at the certain positon on the beam axis. Illuminations maps on the plate is taken by image intensifier (IIF) and CCD which are placed in the rear of the chamber.

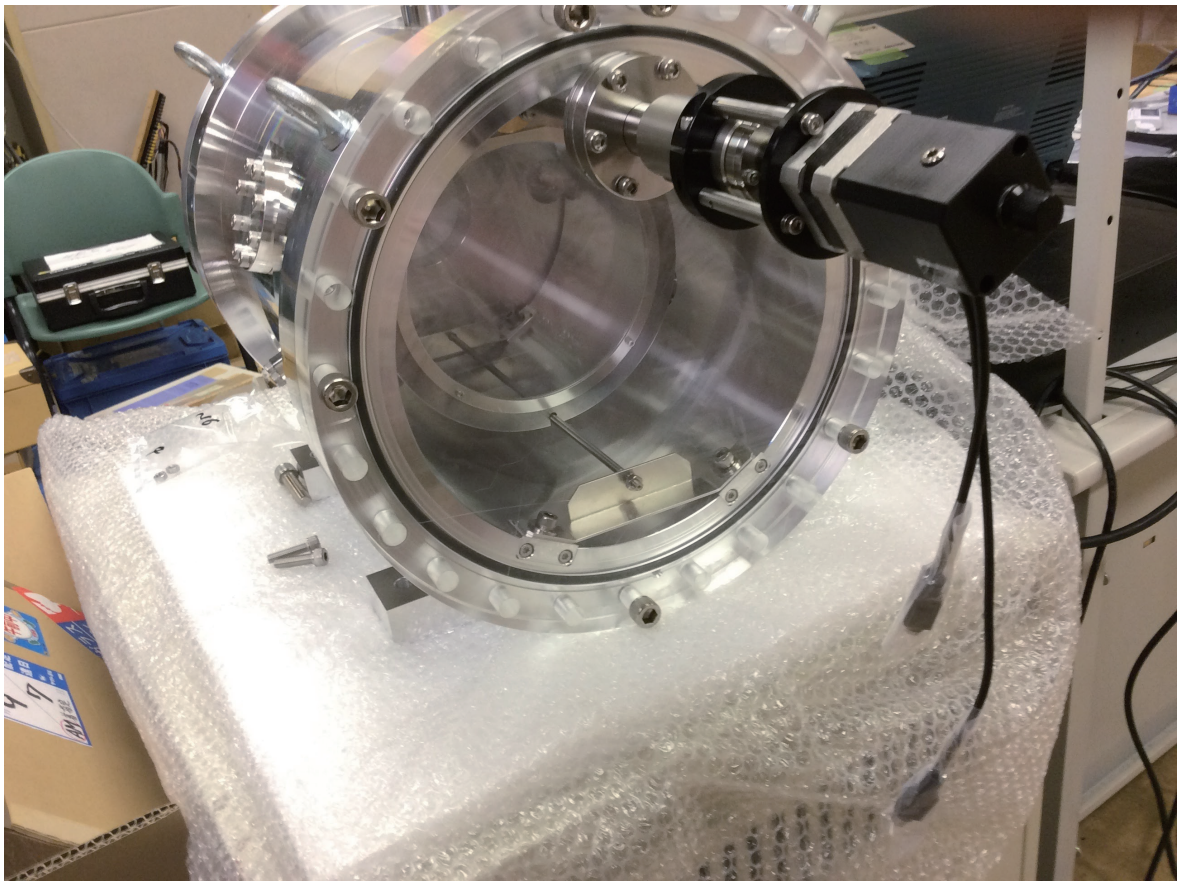

Figure 4.77: A photograph of TBPM.

4.11 Positron Detector

The detector for decay positrons is developed by S. Kanda and others[65]. The Positron detector is composed of 576 channels of segmented scintillators (10 mm × 10 mm ×

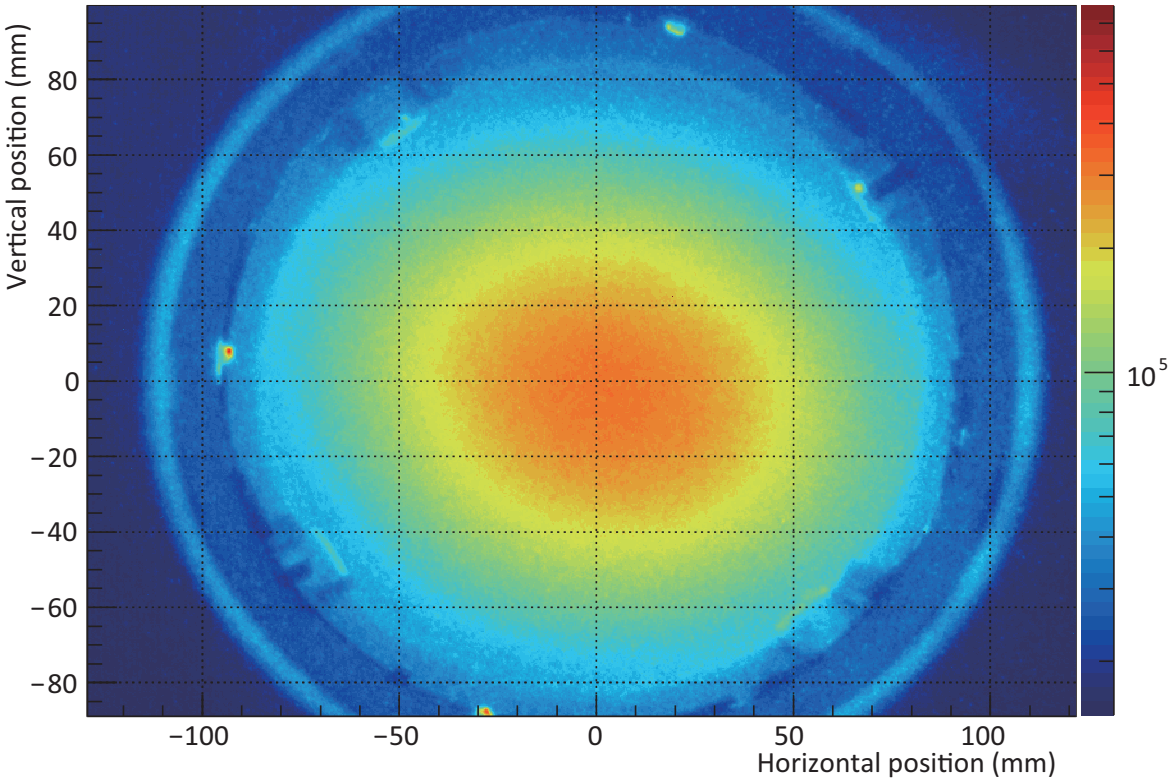

Figure 4.78: A typical measured muon beam profile. The scintillator plate is located on the center of the cavity and the gas pressure is 0.3 atm.

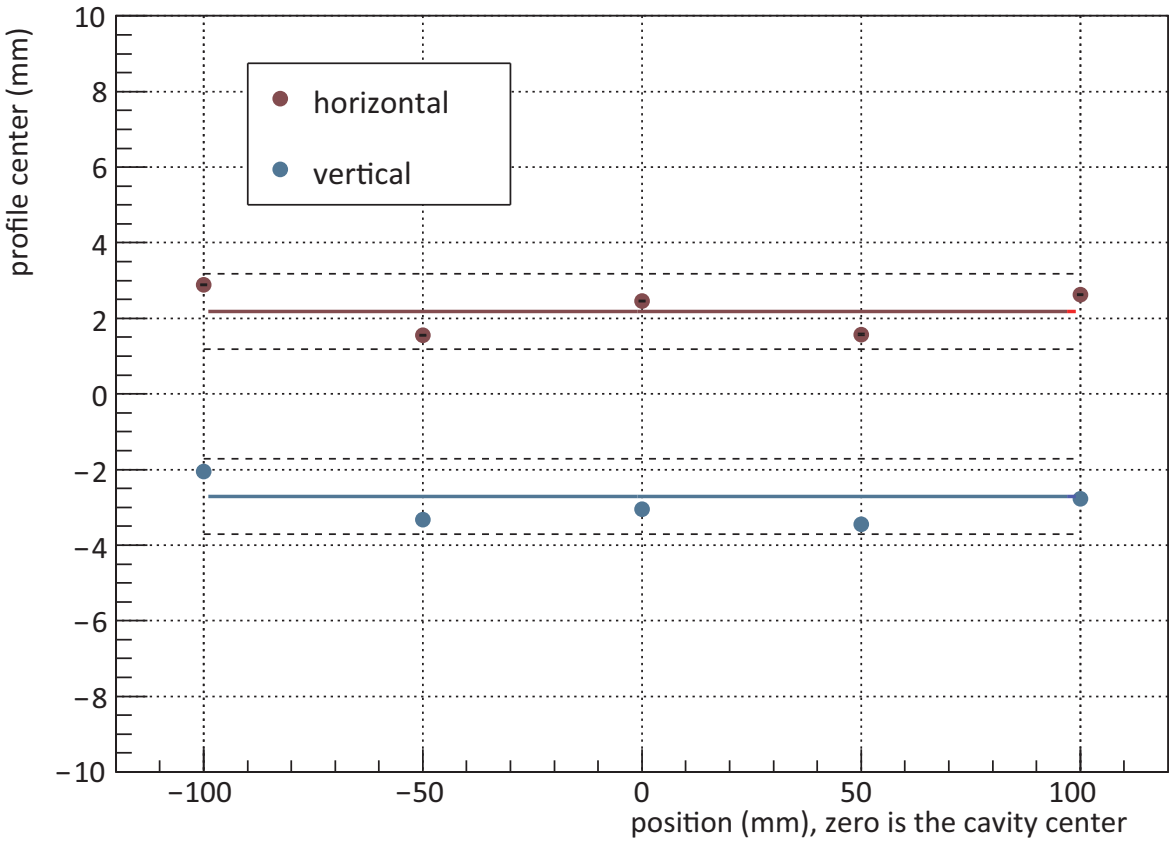

Figure 4.79: A relation between the profile position and the position of the scintillator. The origin point of the position is defined as the cavity center.

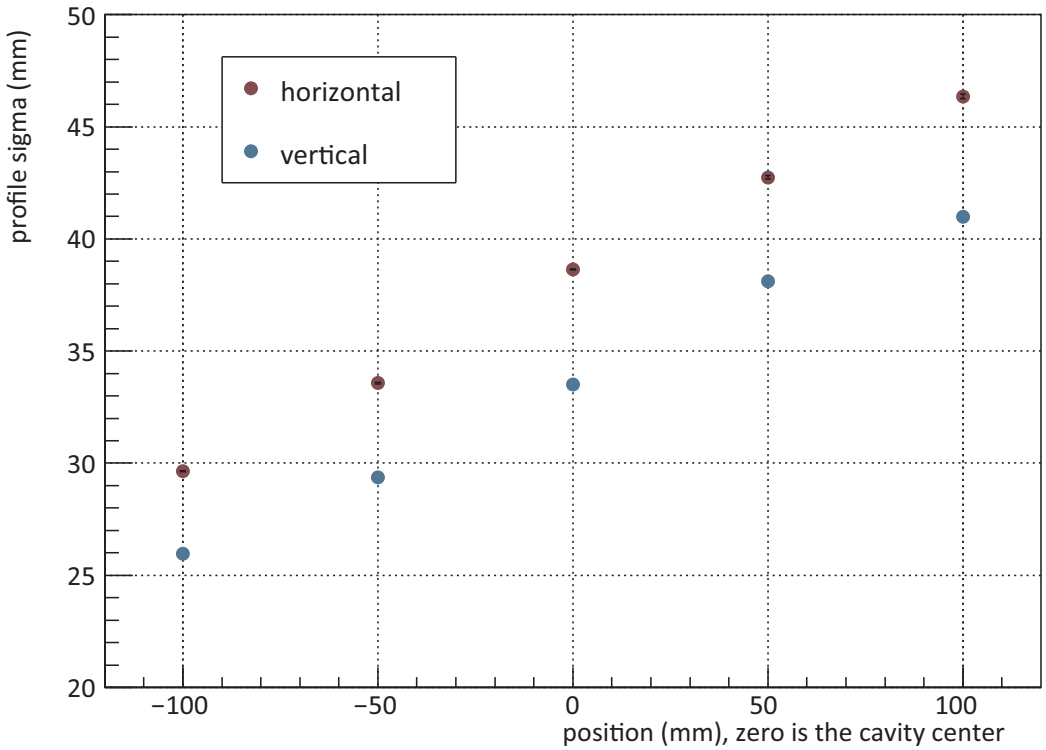

Figure 4.80: A relation between the profile width and the position of the scintillator. The origin point of the position is defined as the cavity center.

3 mmt) directly mounted on Multi-Pixel Photon Counter (MPPC). The detection area is 300 mm × 300 mm.

For measurement at high intensity pulsed muon beam line, it endures in use for high rate positrons such as 3400 e^+.

4.12 Superconducting magnet

The superconducting magnet developed by K. Sasaki and others is used for the high field experiment to apply 1.7 T magnetic field. The magnet provides a magnetic field with a stability of 0.003 ppm/hour. The field homogeneity reaches at the ppm level by using a shimming method. First, measure a magnetic field at 576 points on an ellipsoid surface. Then put iron pieces into pockets surrounding the inner surface of the magnet to correct a variation of a magnetic field.

The uncertainty from magnetic field is discussed in Subsection 5.9.

4.12.1 NMR probe

The magnetic field in the superconducting magnet is measured by the set of NMR (nuclear magnetic resonance) probes. The continuous-wave spectroscopy (CW spectroscopy) is used for this measurement. The NMR spectra is obtained as the RF absorption signal by applying the reference RF and the modulation magnetic field in a certain external magnetic field (Figure 4.82). The magnetic field map is obtained by the set of NMR probes driven by ultrasonic motor, and the fluctuation of the magnetic field during the measurement is monitored by several fixed NMR probes. The systematic uncertainties from NMR probes are discussed in Subsubsection 5.9.1. This system is developed by K. Sasaki, Y. Ueno and T. Mizutani and others.

4.12.2 Shimming

The inhomogeneity of the magnetic field in the superconducting magnet is reduced by mounting a shim plates made of iron on the inner coils. Figure 4.83 shows a positions

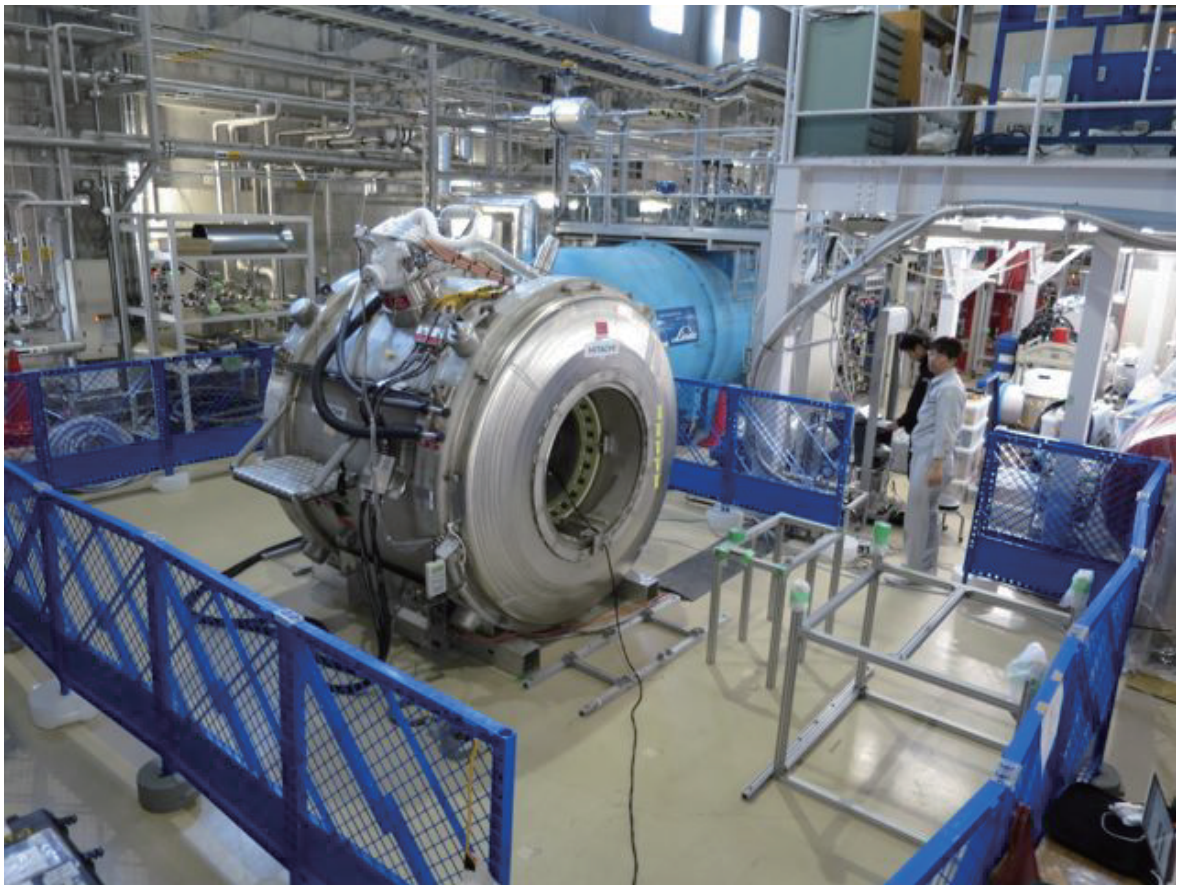

Figure 4.81: A photograph of superconducting magnet.

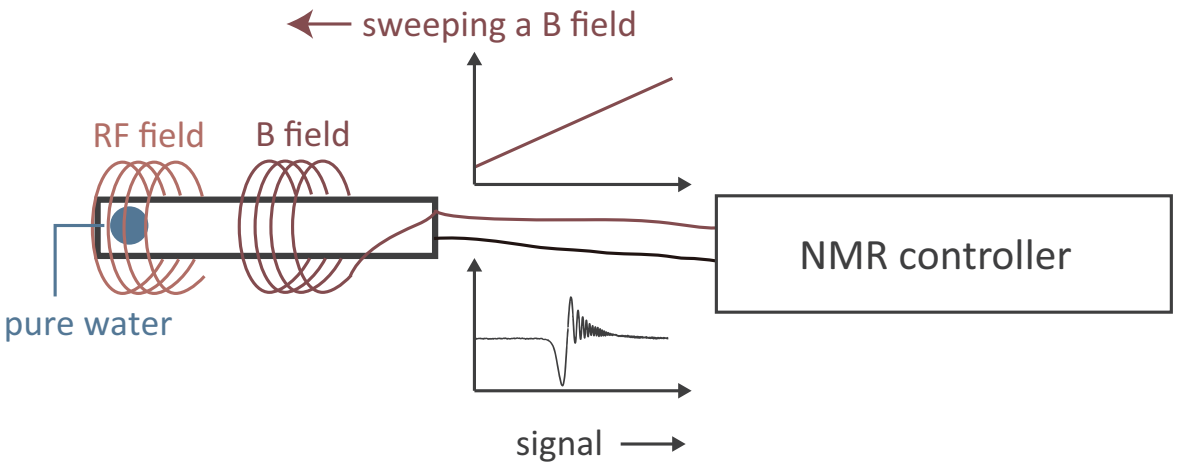

Figure 4.82: An overview of the CW spectroscopy of NMR. The NMR spectra is obtained as the RF absorption signal by applying the reference RF and the modulation magnetic field in a certain external magnetic field. External magnetic field is obtained by the reference magnetic field at the zero-crossing of modulation magnetic field.

to mount shim plates.

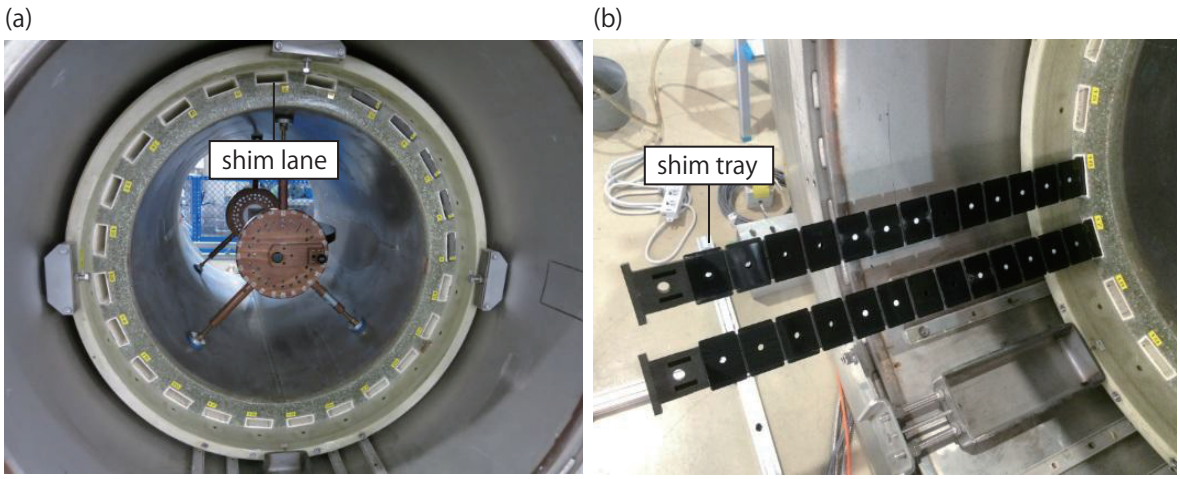

Figure 4.83: Photo of the superconducting magnet and shim trays on the inner surface of the magnet. (a) There are 24 shim lanes at regular intervals. (b) Each shim lanes have 24 shim trays which enable to load up to 13 cm^3.

Chapter 5

Analysis and evaluating uncertainties

The statistical uncertainty and systematic uncertainties are estimated in this chapter. For each kind of uncertainty, a summarized table is given for quantities we measure in the experiment (Table 5.1).

$\delta\nu_{12}$	an uncertainty of the ν_{12} transition in high field experiment
$\delta\nu_{34}$	an uncertainty of the ν_{34} transition in high field experiment Hz
$\Delta\nu_{\mathrm{HF}}$	an uncertainty of Mu HFS value in high field experiment
$\Delta\nu_{\mathrm{ZF}}$	an uncertainty of Mu HFS value in high field experiment
μ_μ/μ_p	an uncertainty of the muon-proton magnetic moment ratio in high field experiment

Table 5.1: A description of the summarized table of uncertainties.

5.1 General approach

We have developed a full Monte Carlo simulation package to reproduce the resonance line shape which will be observed in the experiment. The package tracks the whole process of the experiment which includes the muonium formation in krypton gas, transitions between atomic states via the interaction with a RF field under a magnetic field,

the weak decay of muon which emits a positron, and positron detection by detectors. This package is used to evaluate systematic uncertainties of the experiment, and will be the base for the analysis code for the experimental data.

The simulation package consists of four parts (Figure 5.1). The first part generates the map of muon stopping distribution within experimental apparatus using GEANT4 Monte Carlo package. All apparatus such as beam line magnets and ducts, the front beam profile monitor, the gas chamber filled with krypton gas, the RF cavity within the chamber are all modeled in the code.

The second part generates the map of strength of RF field inside the cavity using CST STUDIO. The physical dimensions and properties of the RF cavity and tuning bars are taken into account in the calculation.

The third part calculates the detection efficiency of a positron emitted following the decay of muon as a function of the initial kinetic energy, direction and the positron muon decay using GEANT4 Monte Carlo package. The code follows the path of the positron from the positon where muon decays to where it stops in (or escapes from) our apparatus under the magnetic field.

The last part curries out a Monte Carlo simulation to determine the observed resonance line shape under as a function of RF frequency using the muon stopping distribution map(Equation 3.13), the RF field map, the positron detection efficiency map. Figure. 5.2 shows time evolutions of different resonance frequencies generated by the tool. Transition probabilities can be calculated by integrating time evolutions from t_1 to t_2. The code tracks the evolution of occupation probabilities of atomic states of a muonium with RF field.

5.2 Fitting method

Systematic uncertainties are estimated from the change of the simulated resonance line shape due to fluctuations of one of experimental conditions. If the variation results the shift of the estimated value, it is listed as the systematic uncertainty. If the variation results the widening of the confidence interval of the estimated value, the broadening

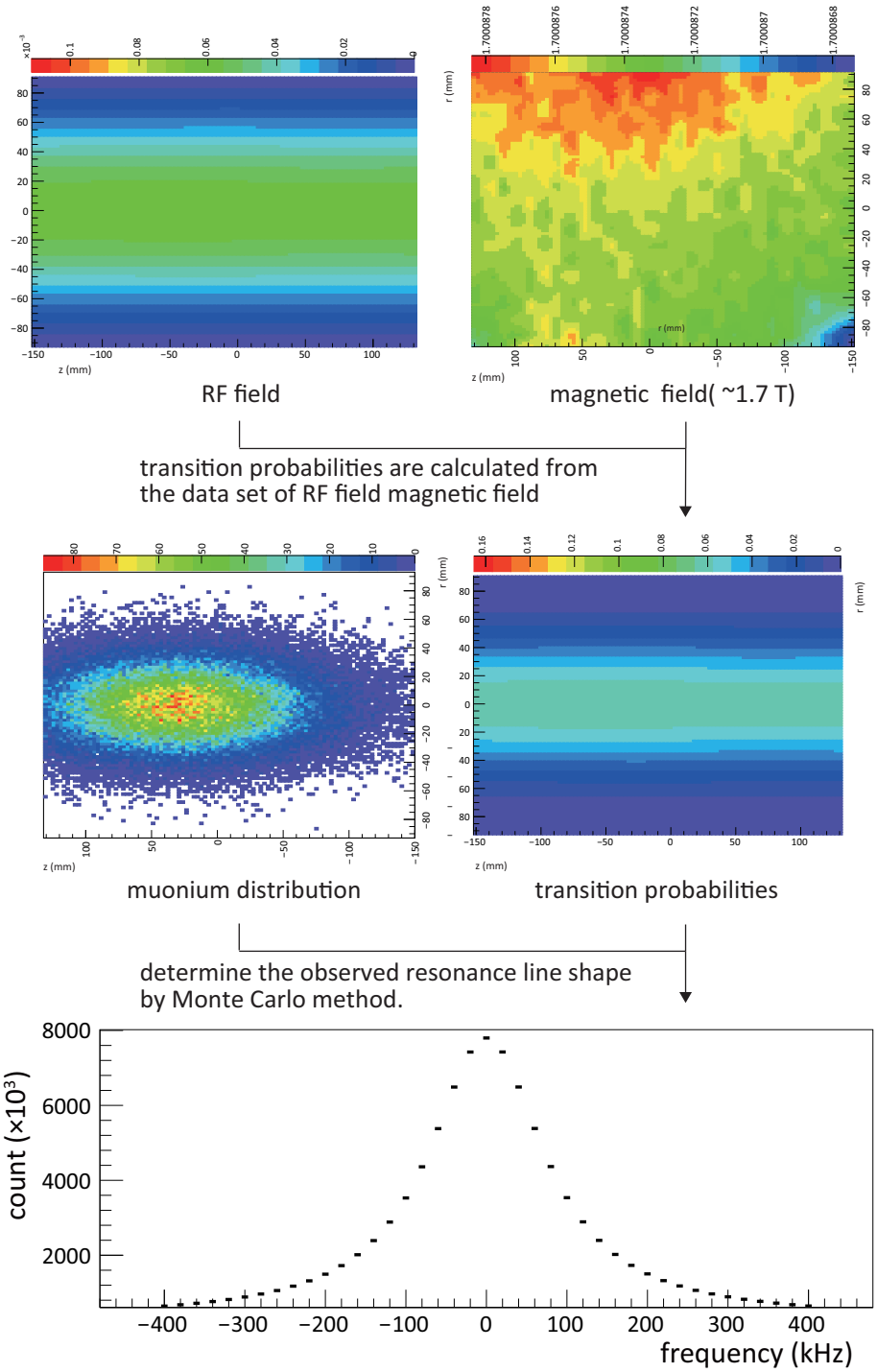

Figure 5.1: A diagram of the simulation package. Probabilities of transitions are calculated by using data sets of a magnetic field, a RF field. Then the observed resonance line shape is determined by the Monte Carlo method.

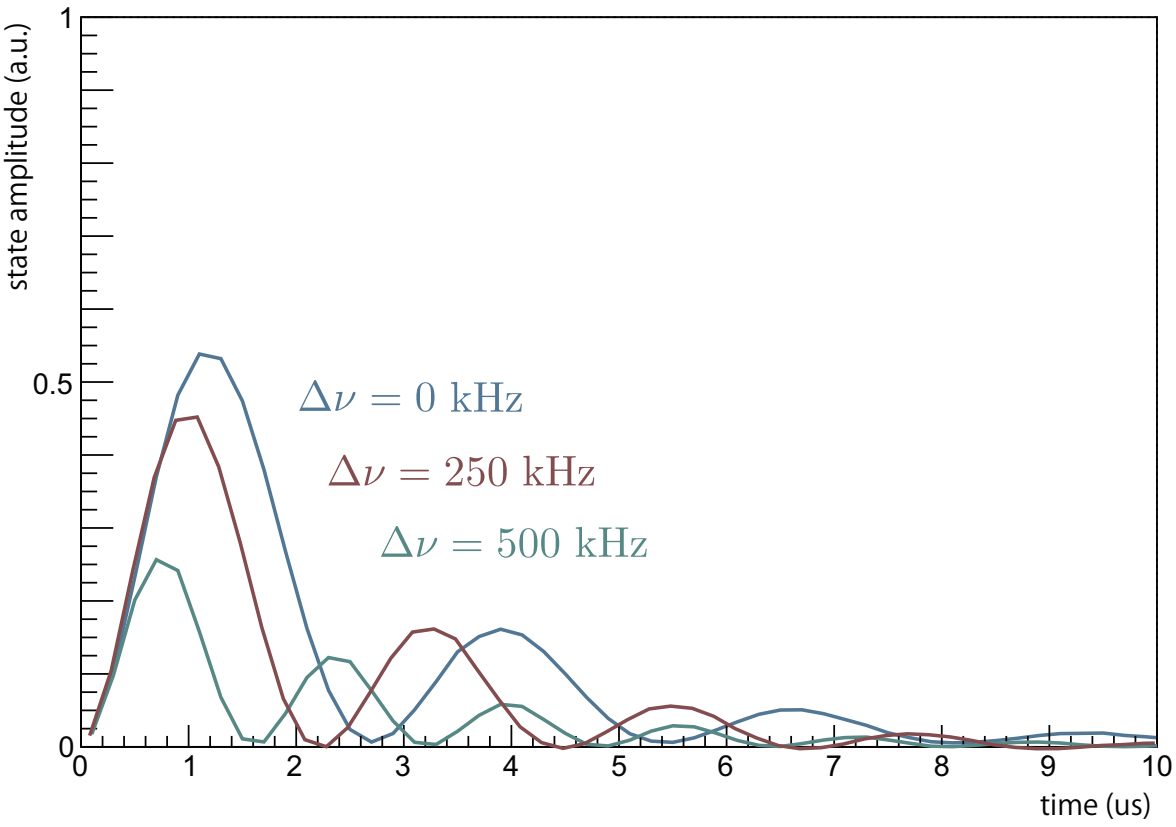

Figure 5.2: Typical time evolutions in case of the difference between the transition frequency and the resonance frequency (Δ_ν) is 0 kHz(blue line), 250 kHz(red line), 500 kHz(green line).

is listed as the systematic uncertainty. In following sections, we look at the functions to fit the simulated resonance line shape.

5.2.1 conventional resonance line

The simplest function to fit the resonance line shape would be a Lorentzian function as shown in Equation 3.15,

$$S(\omega) = N\frac{2|b|^2}{\omega'^2 + 4|b|^2 + \gamma^2}, \tag{5.1}$$

where $|b|^2$ is RF power. Though, this function gives poor fitting because the muonium atoms interact with RF field of different strength, depending on its position. Figure 5.3, shows a time evolution with constant strength of the RF and the magnetic field and distributed RF and magnetic field. According to this figure, the function to fit the resonance line shape is required to be taken into account the relaxation of the time evolution from the distributed RF field.

The fitting improves when the function is a convolution of the Lorentzian function and RF power distribution map over. Thus, more proper function for resonance line shapes by using a conventional method is

$$S(\omega) = \int_{b_{\min}}^{b_{\max}} N(b)\frac{2|b|^2}{\omega'^2 + 4|b|^2 + \gamma^2}\mathrm{d}b \tag{5.2}$$

Figure 5.4 shows a comparison of chi squares of Equation 5.1 and Equation 5.2. Thus Equation 5.2 enables proper fittings for resonance line shapes.

5.2.2 oldmuonium resonance line

In case of oldmuonium method, the fitting function is convolution of Equation 3.14 with the histogram of the RF power as

$$S(\omega) = \int N(b)\frac{2|b|^2}{\Gamma^2}(e^{-\gamma t_1}(1 - (\cos\Gamma t_1 - \frac{\Gamma}{\gamma}\sin\Gamma t_1)\frac{\gamma^2}{\Gamma^2+\gamma^2}) \tag{5.3}$$

$$-\frac{2|b|^2}{\Gamma^2}(e^{-\gamma t_2}(1 - (\cos\Gamma t_2 - \frac{\Gamma}{\gamma}\sin\Gamma t_1)\frac{\gamma^2}{\Gamma^2+\gamma^2})) \tag{5.4}$$

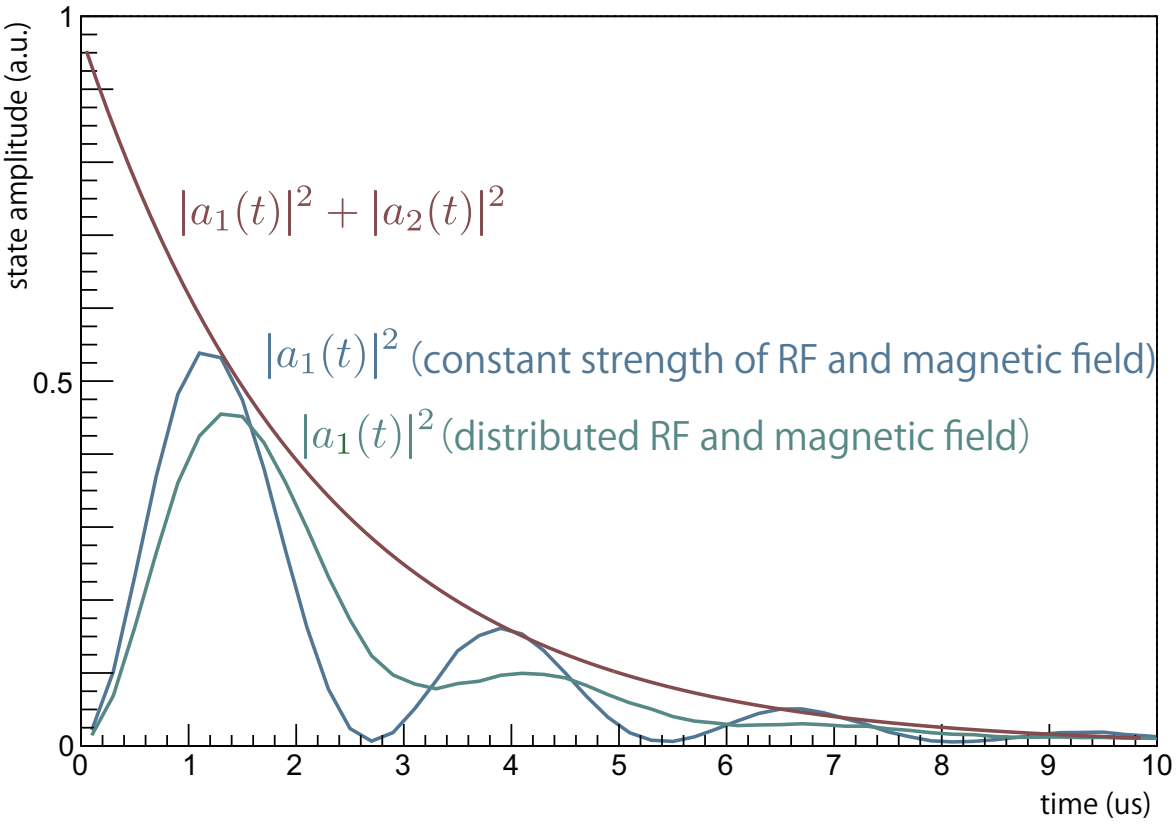

Figure 5.3: Typical time evolutions of a sum of state amplitudes $|a_1(t)|^2 + |a_2(t)|^2$ (red line), a state amplitude $|a_1(t)|^2$ with constant strength of the RF and the magnetic field(blue line), and an integrated state amplitude $|a_1(t)|^2$ with distributed RF and magnetic field (green line) obtained by the simulation package. There is a relaxation effect by distribution of a RF field and a magnetic field in case of distributed muoniums.

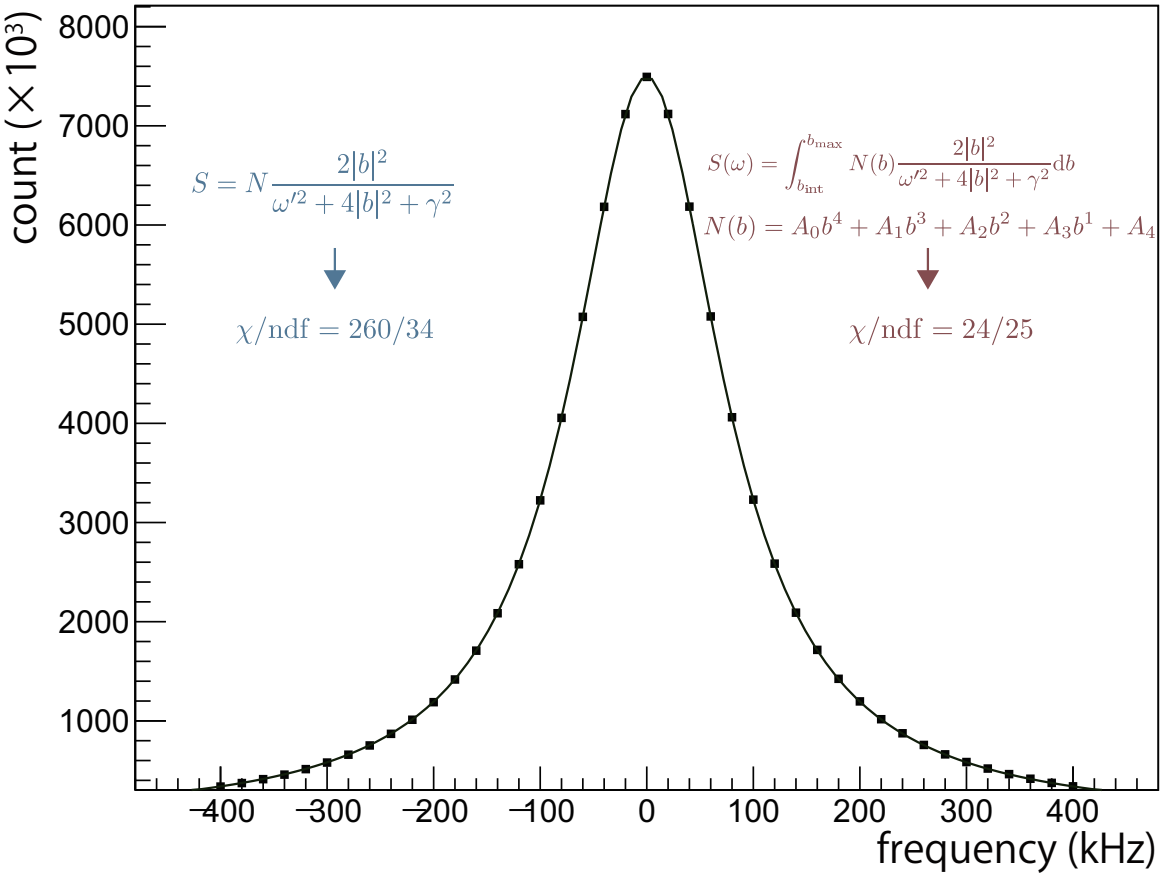

Figure 5.4: Comparison of chi squares of Equation 5.1 and Equation 5.2.

5.3 Statistical uncertainties

A statistical uncertainty can be improved by optimizing the t_1 and t_2 of Equation 3.14. Figure 5.5 shows a resonance line shape in case of $t_1 = 0$ and $t_2 = \infty$ which is called "conventional method" and upper of this figure show time evolutions of state amplitudes of each points.

Figure 5.6 shows a resonance line shape in case of $t_1 = 6$ μs and $t_2 = 7$ μs which is called "oldmuonium method". Signal ratios of each points are proportional to value of integral of time evolutions from t_1 to t_2. As Equation 3.13 shown, the time evolution is determined by the strength of microwave. Thus, a linewidths of a resonance line can be reduced by optimizing t_1 and t_2.

Figure 5.7 shows a relation between statistical uncertainties by using the oldmuonium method and t_1 in case of $t_2 - t_1 = 1$ μs. The horizontal line shows a statistical uncertainty using conventional method by using same number of muons. It assumes that scan range is 400 kHz and number of scan points is 21. The number of muonoiums to use of each points is 10^8. The line broadening from the microwave increase the statistical uncertainty in case of low t_1. On the other hand, since the number of observed muonium is decreased in case of high t_2, the statistical uncertainty is increased even the linewidth is narrow.

Figure 5.8 shows relation between t_1 and the center value of the resonance lines. It assumes the same scan range and the statistics as Figure 5.7. The red band shows the uncertainty bar of the average value of 6 results using the old muonium method from $t_1 = 0$ μs to $t_1 = 10$ μs. As a result, the uncertainty by using a conventional method is 18 Hz and by using an oldmuonium method is 9.4 Hz which is superior to a conventional one. Moreover, the average value of 6 results using the old muonium method which is so called time-slicing method enable to improve uncertainty such as 4.9 Hz.

The intensity of H Line is 1×10^8/s and D line is 1.5×10^7/s. The number of decay positrons per a muon is 0.7 % obtained by the result of GEANT4[7] simulation. Then the statistical uncertainty is under 5 Hz by measurement in high field for a week at

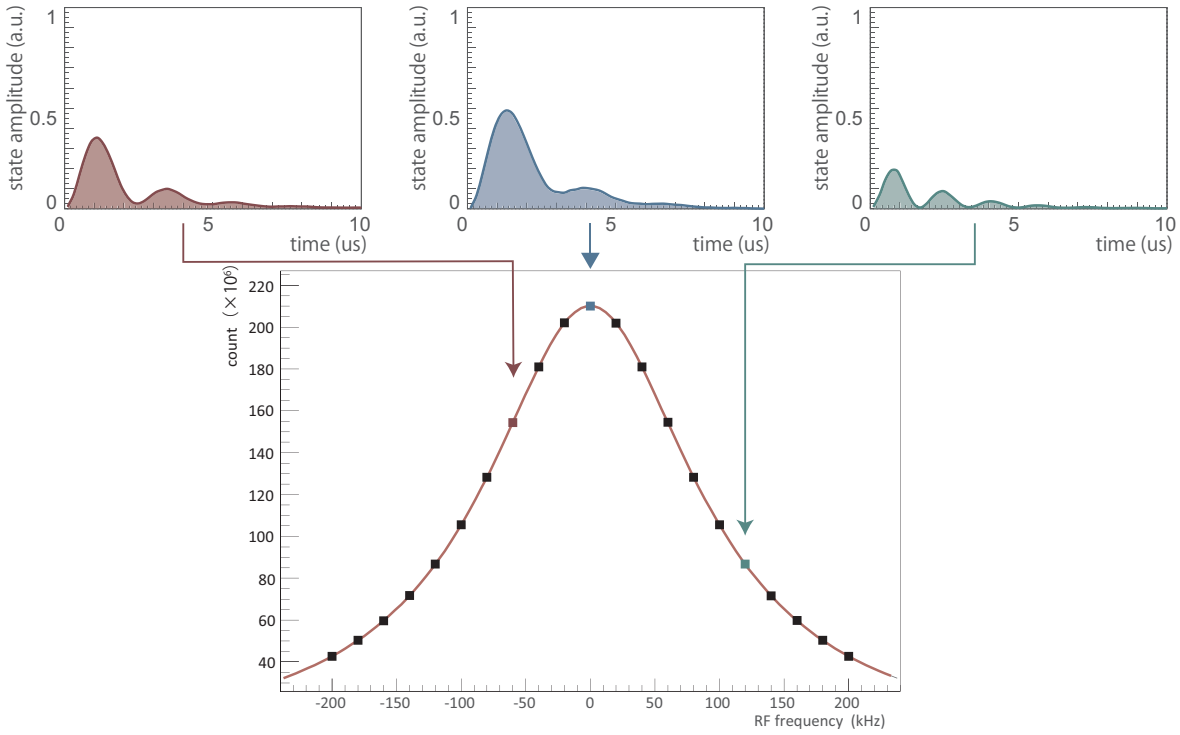

Figure 5.5: A typical resonance line shape using a conventional method obtained by the simulation package. The total number of muons are 10^8 at each frequency points. Total counts of decay positrons are proportional to the integrated values of state amplitude from $t = 0$ to $t = \infty$.

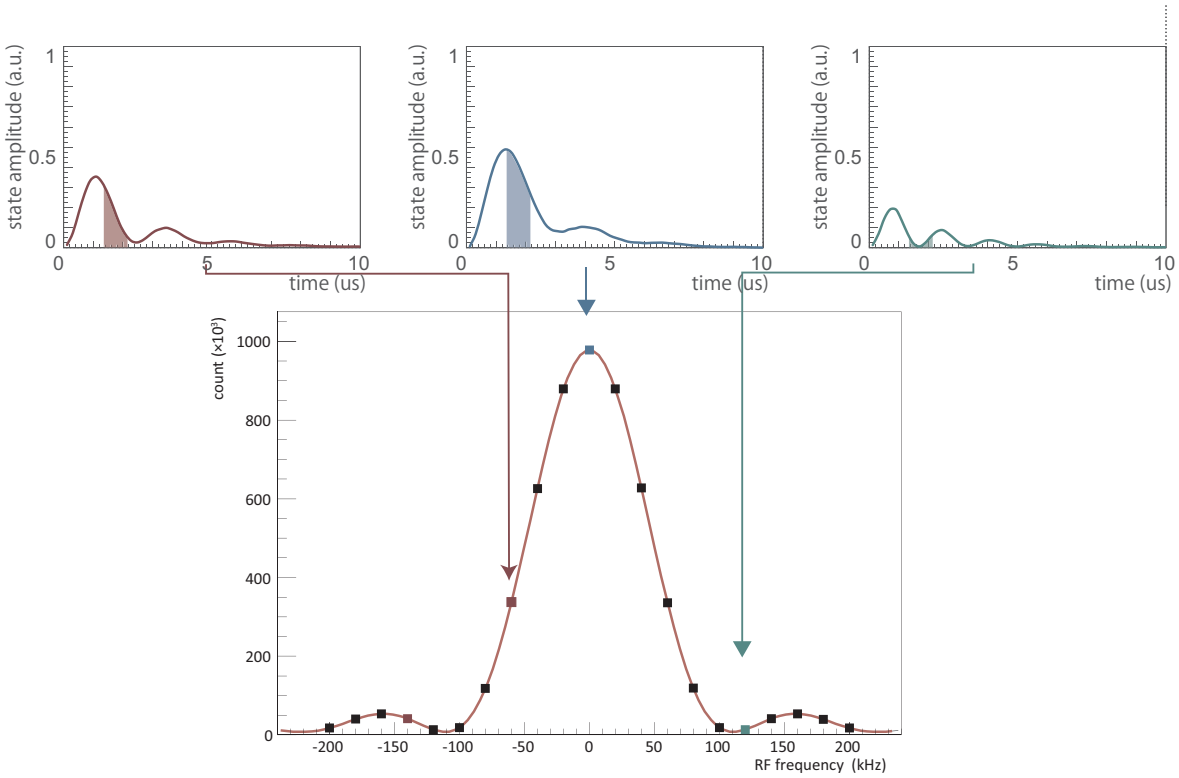

Figure 5.6: A typical resonance line shape using an oldmuonium method obtained by the simulation package. The total number of muons are 10^8 at each frequency points. Total counts of decay positrons are proportional to the integrated values of state amplitude from $t = t_1$ to $t = t_2$. Even the total counts are decreased, FWHM of the peak is narrower than the peak obtained by using a conventional method.

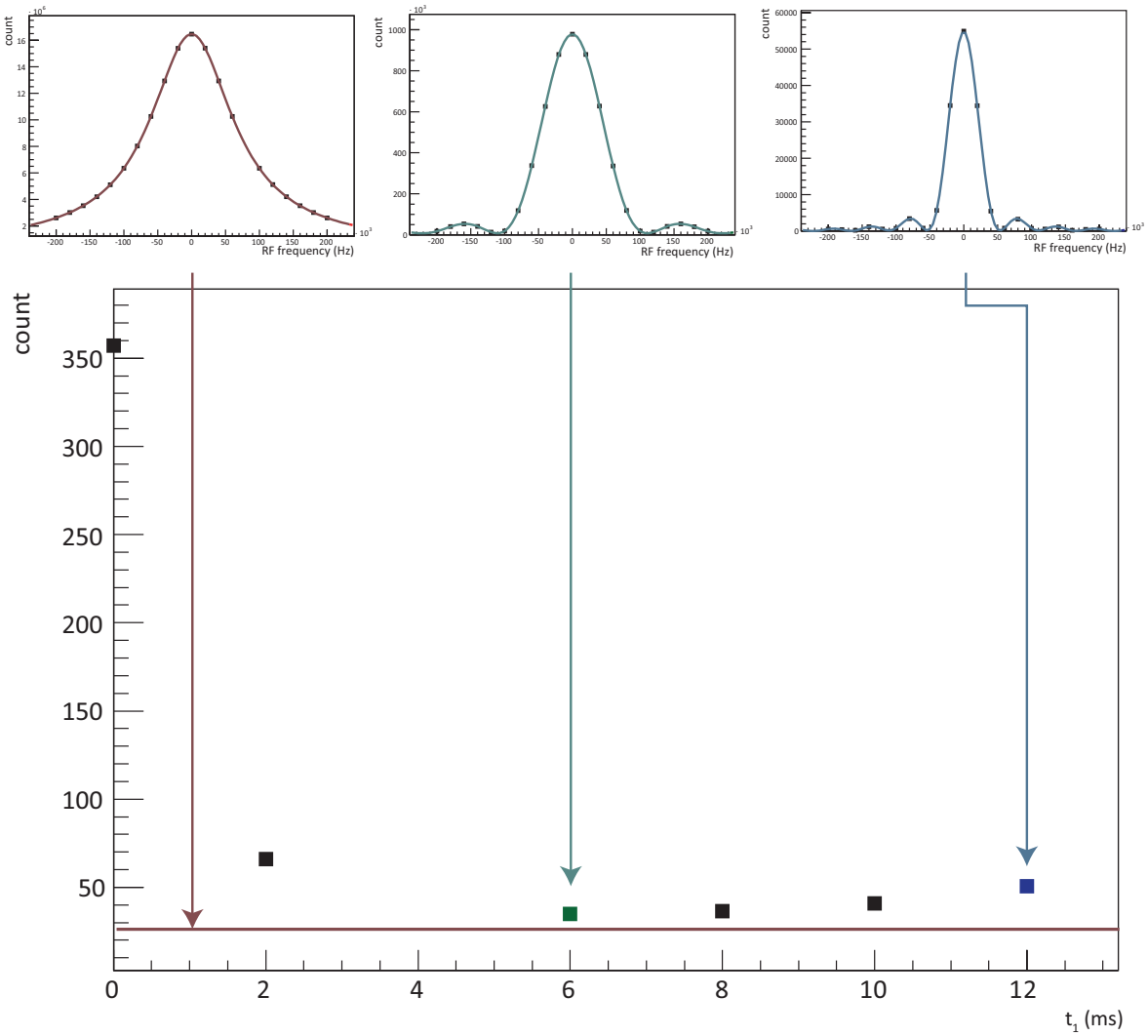

Figure 5.7: Relation between statistical uncertainties by using the oldmuonium method and t_1 in case of $t_2 - t_1 = 1$ μs. They assume that scan range is 400 kHz and number of scan points is 21. The number of muonoiums to use of each points is 10^8. The horizontal line shows a statistical uncertainty using conventional method by using same number of muons.

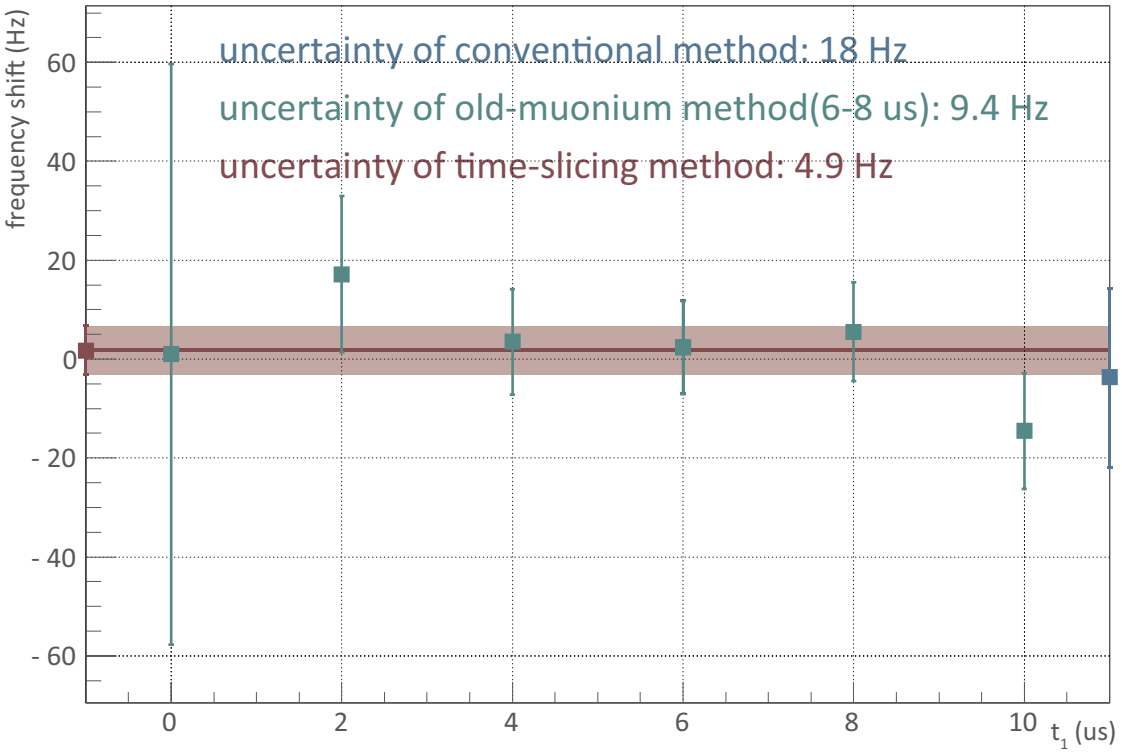

Figure 5.8: Comparison of statistical uncertainty between the conventional method and the oldmuonium method. A blue point show the resonance frequency obtained by the conventional method. Green points show the resonance frequencies obtained by the oldmuonium method with 2 μs time interval at each t_1 and the red band shows the uncertainty bar of the average value of 6 results using the old muonium method from $t_1 = 0$ μs to $t_1 = 10$ μs which is so called time-slicing method.

H Line including both ν_{12} and ν_{34}. Also, the statistical uncertainty is under 20 Hz by measurement in zero field for a day at D Line.

$\delta\nu_{12}$	3.5 Hz
$\delta\nu_{34}$	3.5 Hz
$\Delta\nu_{\mathrm{HF}}$	5 Hz
$\Delta\nu_{\mathrm{ZF}}$	20 Hz
μ_μ/μ_p	15 ppb

Table 5.2: Statistical uncertainty

5.4 Uncertainty from RF power

5.4.1 Evaluation at LAMPF experiment

As equation 3.15, the resonance line shape of conventional method ($t_1 = 0, t_2 = \infty$) can be expressed as

$$S = \frac{2|b_0^2|}{4\pi^2\alpha'^2x^2 + 4|b_0^2| + \gamma^2}, \tag{5.5}$$

where x is a difference between resonance frequencies and transition frequencies. The stability of the RF power in LAMPF experiment is 0.01% and they assumed that the fluctuation of RF power is proportional to the resonance frequencies such as

$$|b_0|^2 \to |b_0|^2(1 + kx). \tag{5.6}$$

Then Equation 5.5 is

$$S' = \frac{2|b_0|^2(1 + kx)}{4\pi^2\alpha'^2x^2 + 4|b_0|^2(1 + kx) + \gamma^2}. \tag{5.7}$$

By using approximation $|kx| << 1$,

$$S' \approx \frac{2|b_0^2|}{4\pi^2\alpha'^2(x + k'|b_0^2|)^2 + 4|b_0^2| + \gamma^2}. \tag{5.8}$$

By comparison between Equation 5.5 and Equation 5.8, $k'|b_0^2|$ expresses the frequency shift by fluctuation of the RF power and it is 2 Hz by substituting to 0.01 %. There are following two problems for this discussion.

1. Validity of approximation even they express the frequency shift by 1st order of k in Equation 5.8.

2. $k'|b_0^2|$ does not expresses the shift of the center value of the fitting function of the resonance line, but the peak of it.

To consider about first item, plotting Equation 5.5 and Equation 5.7. by using same parameters of LAMPF experiment (Figure 5.9). It shows that they underestimate the frequency shift from 8 Hz to 2 Hz.

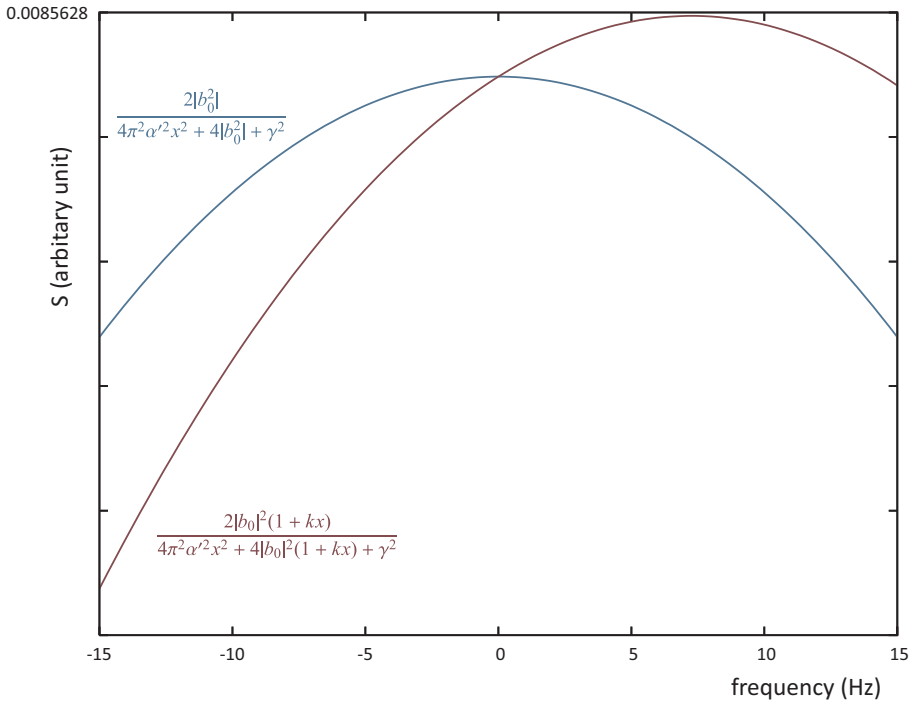

Figure 5.9: A comparison between Equation 5.5 and Equation 5.7. 8 Hz of shift is caused by 0.1 % fluctuation of the RF power.

5.4.2 Uncertainty from RF power

By using the simulation tool, uncertainty from RF power in this experiment is evaluated in this subsection. As described in 4.5.4, RF power is able to be stabilized within 0.02 %. Figure 5.10 shows systematic uncertainties from RF power depend on scanning frequencies. As shown in B, monotonically increasing of RF power within 1 % distort the resonance line shape. Due to this, the systematic uncertainty is 609 Hz. On the other hand, if the random sequence is used for the RF scanning as D, the systematic uncertainty is negligible.

$\delta\nu_{12}$	2 Hz
$\delta\nu_{34}$	2 Hz
$\Delta\nu_{\mathrm{HF}}$	3 Hz
$\Delta\nu_{\mathrm{ZF}}$	3 Hz
μ_μ/μ_p	9 ppb

Table 5.3: Systematic uncertainty from RF power

5.5 Fluctuation of RF field by tuning bars

The RF field in the cavity is fluctuated by the displacement of tuning bars. Fig 5.11 and Fig 5.12 shows a histogram of RF power $|b|^2$ affect to each muons in the cavity in case of displacements of tuning bar are 0 mm and 1 mm. The number of muons are 5.0×10^6 and RF fields are calculated by CST STUDIO[8]. Since peak position of both RF field and muonium distribution is located on the center axis of the cavity, this histogram is almost a monotonically increasing. However there is a small dip at $|b|^2 = 1.2 \times 10^{13}$.

Figure 5.11 shows color maps of each ranges of $|b|^2$. TM110 mode has one node along the radial direction, one node along the angular direction and no nodes along the axial direction. A weak RF field nearby nodes is shown in color map A and a strong

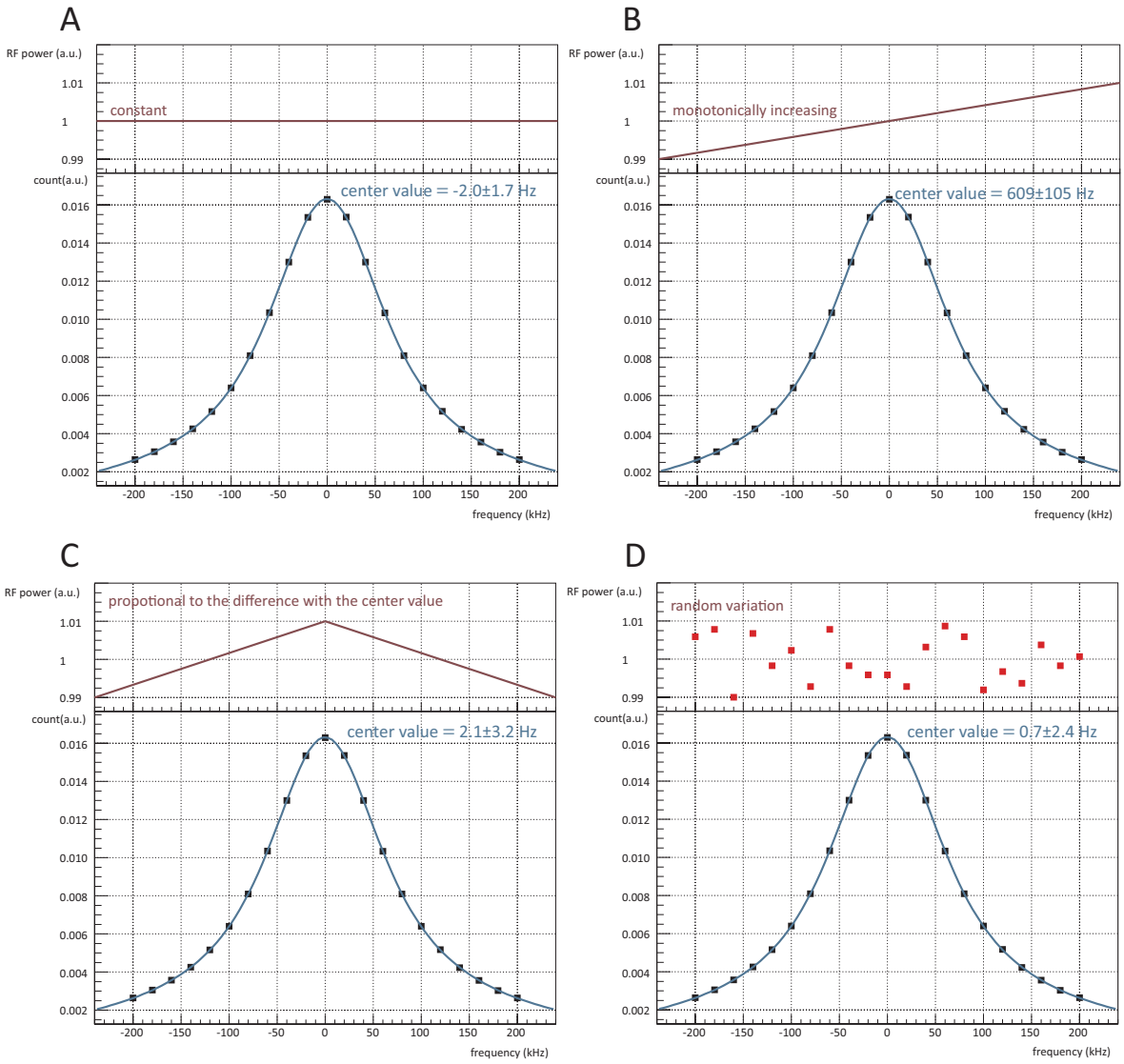

Figure 5.10: Relations between variations of RF power and systematic uncertainties. As shown in B, monotonically increasing of RF power within 1 % distort the resonance line shape. Due to this, the systematic uncertainty is 609 Hz. On the other hand, if the random sequence is used for the RF scanning as D, the systematic uncertainty is negligible.

RF field around the center of the axis is shown in color map C. In color map B, there is a dip caused by the widest area of a RF field of certain power.

Let's consider the case that tuning bar displace from 0 mm to 1 mm during a RF resonance scan. If the resonance lines are fitted by assuming a single RF field map, systematic uncertainty is 180 Hz. By assuming that the uncertainty from the fluctuation of RF field is proportional to the displacement of tuning bars, uncertainties are calculated as Table 5.4.

$\delta\nu_{12}$	4 Hz
$\delta\nu_{34}$	4 Hz
$\Delta\nu_{\mathrm{HF}}$	6 Hz
$\Delta\nu_{\mathrm{ZF}}$	4 Hz
μ_μ/μ_p	17 ppb

Table 5.4: Systematic uncertainty from RF field fluctuation

5.6 Gas pressure

Transition frequencies are changed by the variation of Hamiltonian through the collisions with Kr atoms. Since a collision rate is proportional to a density of the Kr gas, shifts of transition frequencies are expresses as

$$\nu_{ij}(P) = \nu_{ij}(0)(1 + a_{ij}P + b_{ij}P^2), \tag{5.9}$$

where $\nu_{ij}(0)$ is a transition frequencies in vacuum. Transition frequencies in vacuum can be extrapolated from values in certain gas pressures P_1 and P_2. Uncertainties from gas pressure is coming from both quadratic term ($b_{ij}P^2$) and a precision of a pressure gauge.

Quadratic coefficient b_{ij} is determined in a previous experiment as

$$b = (9.7 \pm 2.0)^{-15}\ \mathrm{Torr}^{-2}[62]. \tag{5.10}$$

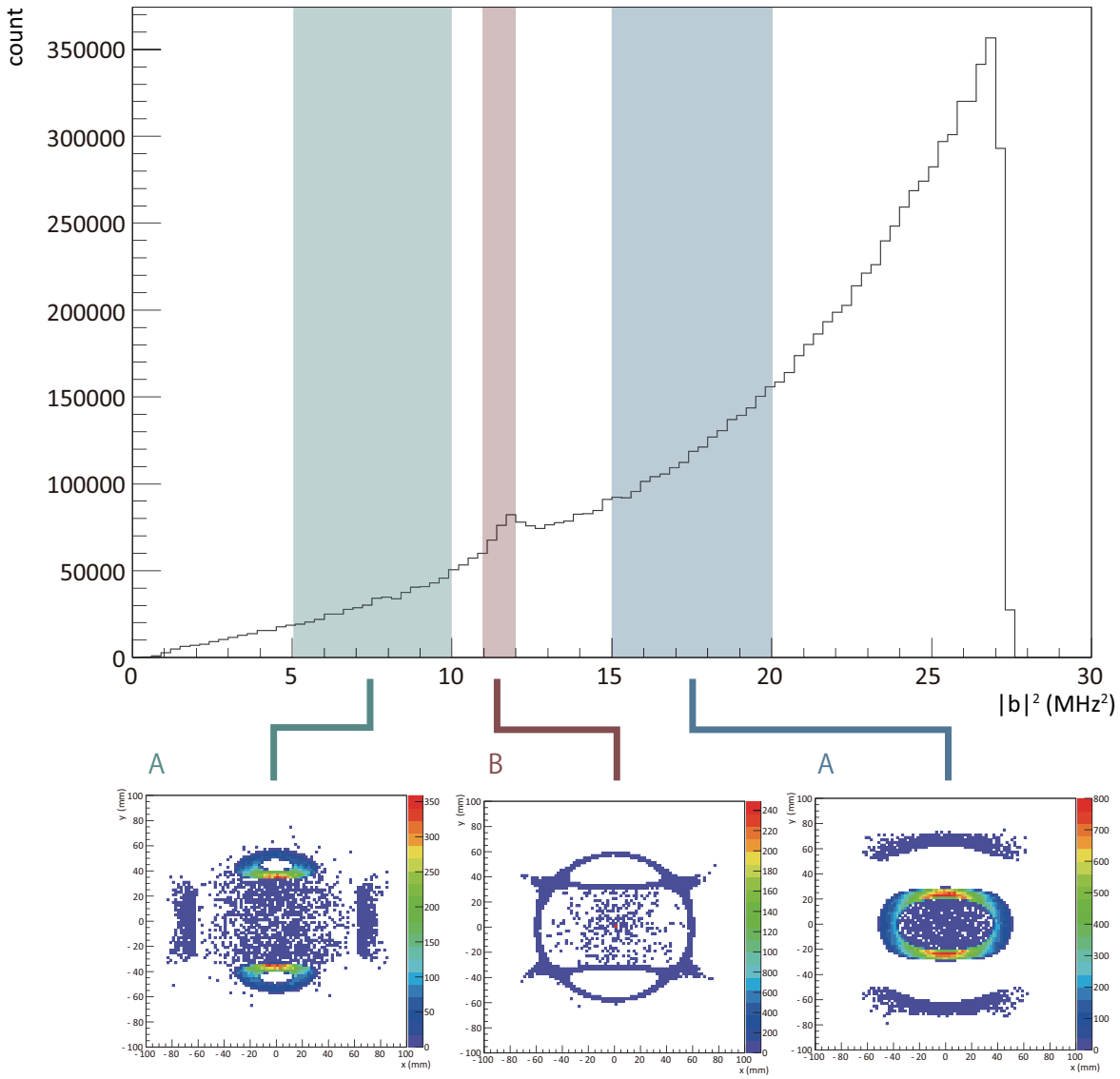

Figure 5.11: A histogram of RF power ($|b|^2$) in case the displacement of the tuning bar is 0 mm. The number of muons are 5.0×10^6 and RF fields are calculated by CST STUDIO[8]. Color maps shows a muonium distributions which feel certain range of the RF power.

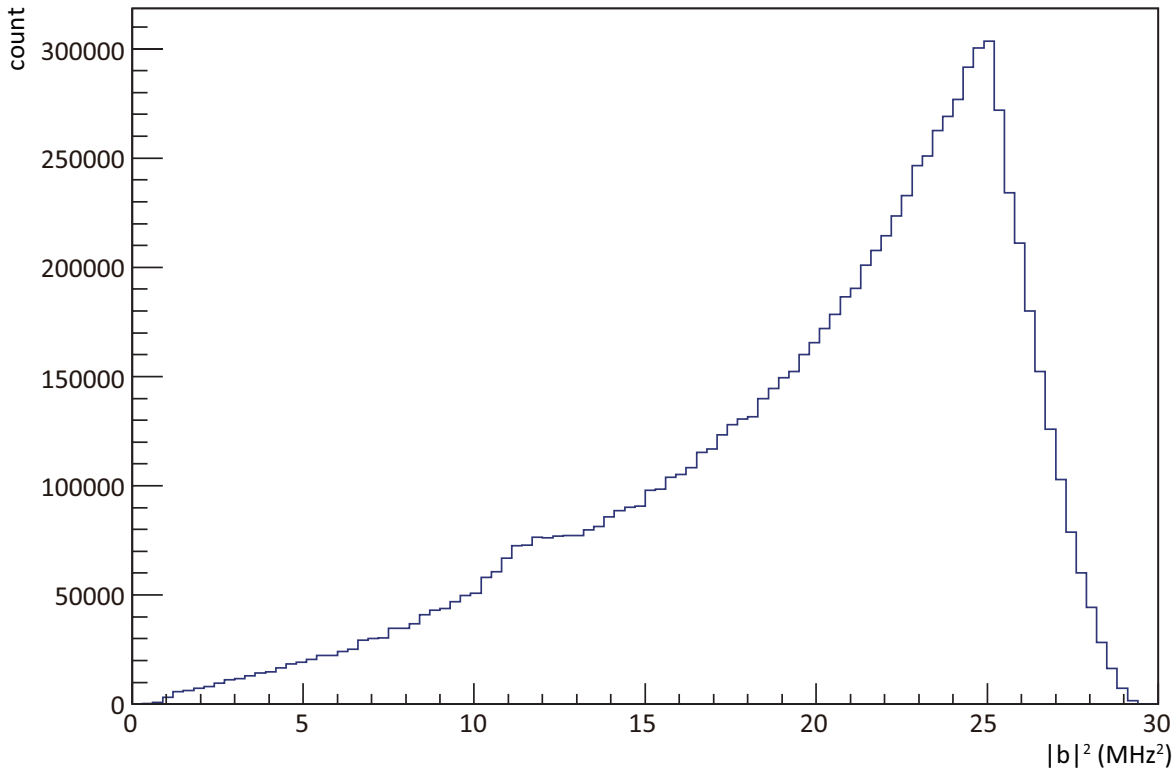

Figure 5.12: A histogram of RF power ($|b|^2$) in case the displacement of the tuning bar is 1 mm. The number of muons are 5.0×10^6 and RF fields are calculated by CST STUDIO[8].

The capacitance gauge (CANON ANELVA M-342DG-13) is prepared for the measurement. The precision of the gauge is 0.20 % of reading. Moreover, the silicon gauge (FLUKE RPM4-AD) is plan to prepare for the precise measurement. The precision of the gauge is 0.02 % of reading. Figure 5.13 shows a how the quadratic term and the precision of the gauge affect to an extrapolation. There are systematic uncertainties from a precision of pressure gauge and a quadratic shift.

Figure 5.14 shows a relation between P_2 and uncertainties. P_1 is fixed to 0.3 atm which is lower limit to stop muons in the cavity. It shows that the uncertainty from capacitance gauge is relatively large compared from the quadratic shift. Figure 5.15 is zoom up of Figure 5.14. It shows that the optimized P_2 value is about 0.9 atm in case of using a silicon pressure gauge.

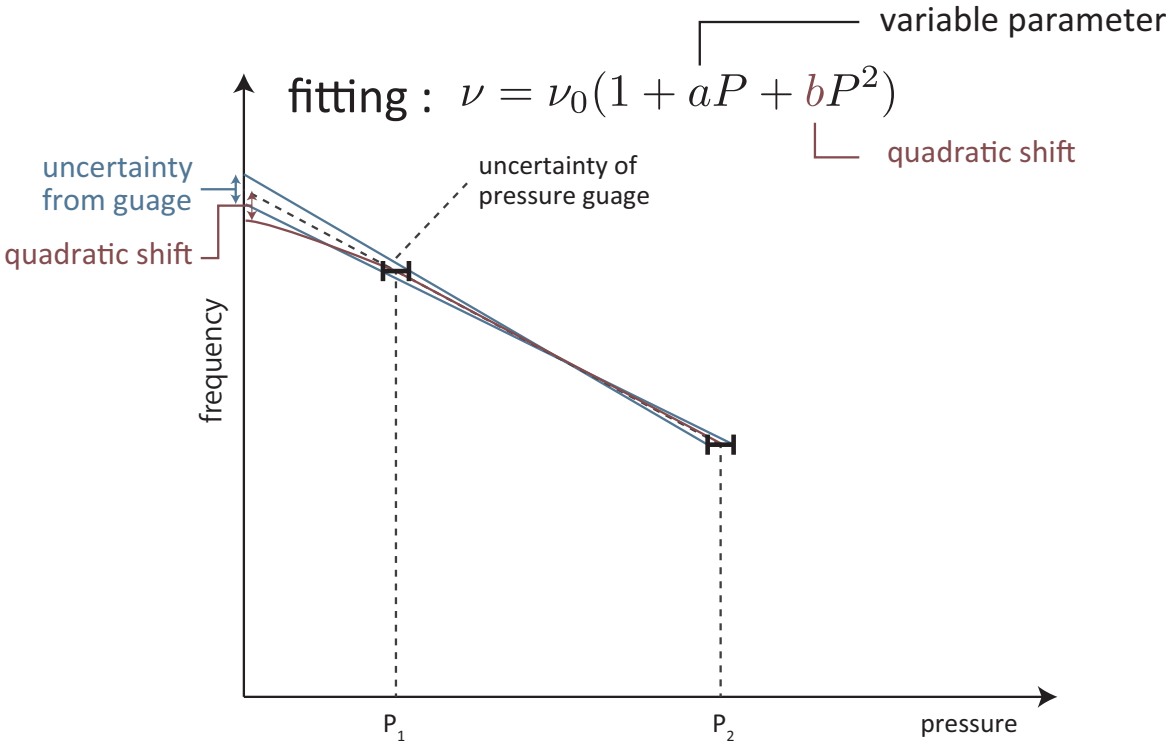

Figure 5.13: A relation between a gas pressures and transition frequencies. A transition frequency can be obtained by extrapolation using values in different gas pressures. There are systematic uncertainties from a precision of pressure gauge and a quadratic shift.

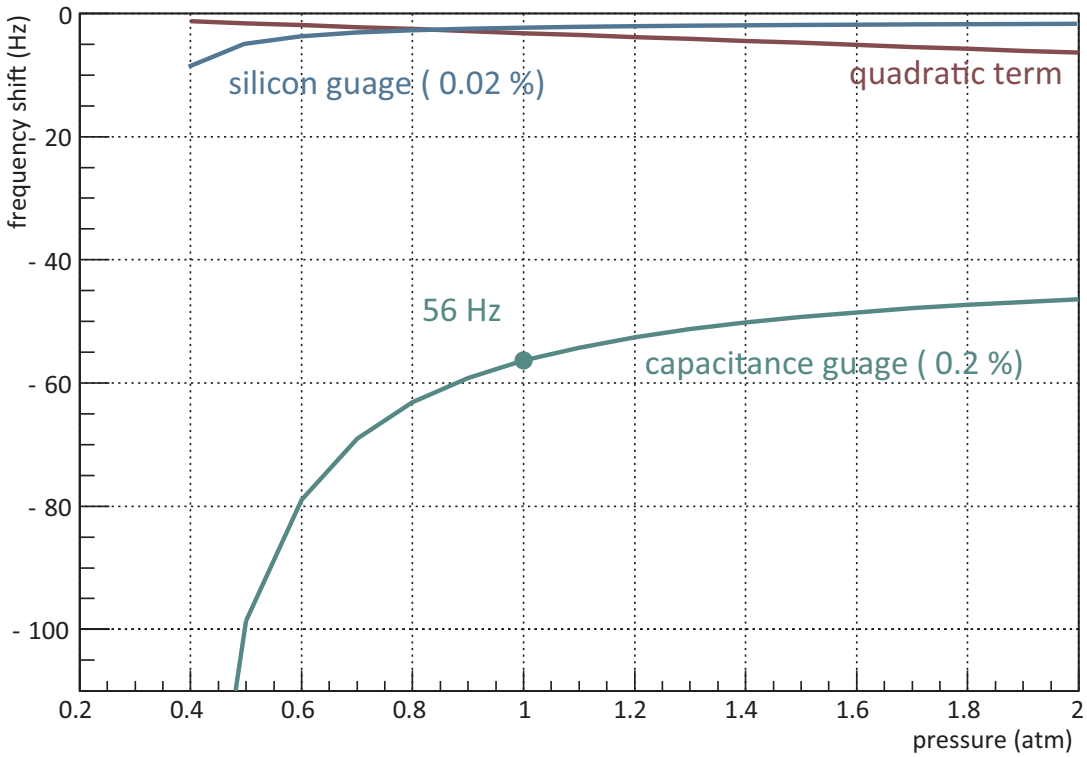

Figure 5.14: A relation between P_2 and uncertainties. P_1 is fixed to 0.3 atm which is lower limit to stop muons in the cavity with collision. The uncertainty from capacitance gauge is relatively large compared from the quadratic shift.

5.7 Temperature

Uncertainties from temperature results from two following parts (Figure 5.16). The first part is by atomic interaction with krypton gas. It was suggested that the shift results from a competition between the attractive-long-range (van der Waals) interaction decreases the electron density at the nucleus, and the repulsive-short-range (Pauli exclusion principle) part of the interatomic potential increases the electron density. This part gives vertical error bars to data points of Figure 5.16. In the case of collision between hydrogen and Argon gas, the shift is expressed as

$$(1/\nu_0)(\delta\nu/\rho) = A + B(T - T_0). \tag{5.11}$$

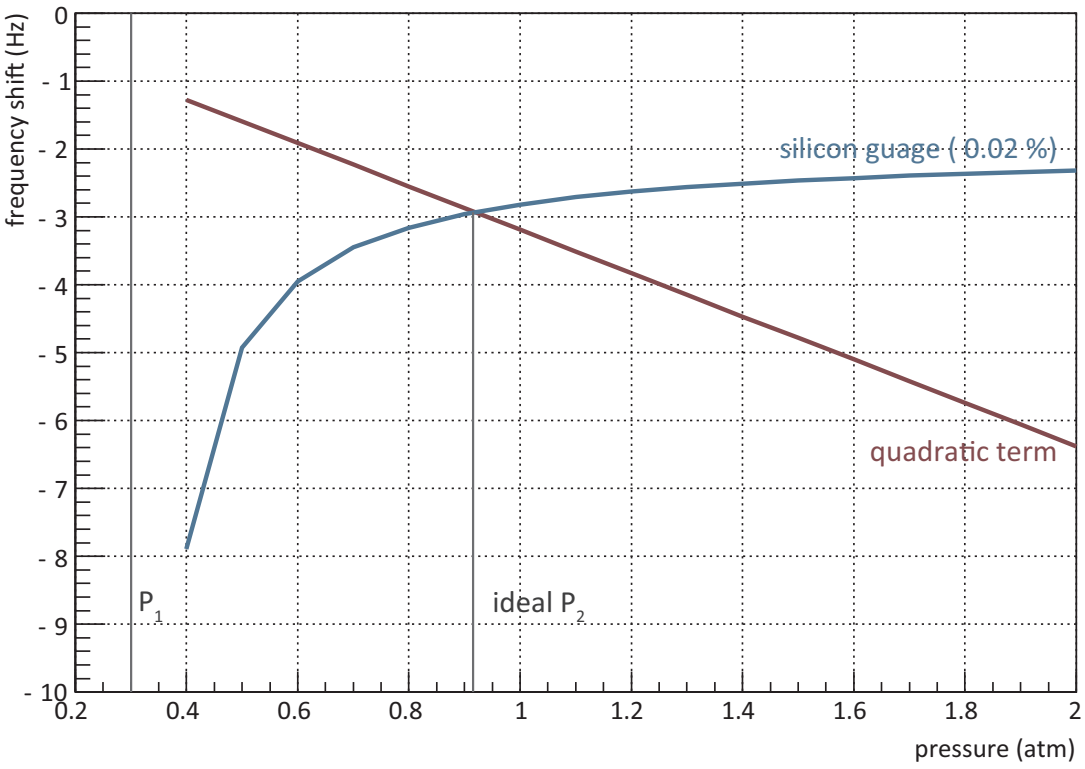

Figure 5.15: A zoom up of Figure 5.14. The optimized P_2 value is about 0.9 atm in case of using a silicon pressure gauge.

$\delta\nu_{12}$	4 Hz
$\delta\nu_{34}$	5 Hz
$\Delta\nu_{\mathrm{HF}}$	9 Hz
$\Delta\nu_{\mathrm{ZF}}$	9 Hz
μ_μ/μ_p	19 ppb

Table 5.5: Systematic uncertainty from gas pressure

A and B was obtained at Yale University [66] as

$$A = (-4.800 \pm 0.006) \times 10^{-9}\ \mathrm{Torr}^{-1}\ (0\ ^\circ\mathrm{C}), \tag{5.12}$$

$$B = (+0.956 \pm 0.011) \times 10^{-11}\ ^\circ\mathrm{C}^{-1}\mathrm{Torr}^{-1}\ (0\ ^\circ\mathrm{C}). \tag{5.13}$$

The secound part is from a variation of gas density by a temperature. We use pressures at 0 °C corresponded to gas densities calculated by monitored gas pressures and temperatrures. The pressure at 0 °C is calculated the real gas equation

$$(P + \frac{n^2 a_v}{V^2})(V - nb_v) = nRT. \tag{5.14}$$

The van der Waals constant are

$$a_v = 0.2325\ \mathrm{barL}^2/\mathrm{mol}, \tag{5.15}$$

$$b_v = 0.0396\ \mathrm{L/mol}[67]. \tag{5.16}$$

This part gives horizontal error bars to data points of Figure 5.16.

Figure 5.17 shows uncertainties of ν_{12} transition in high field experiment from density variation and atomic collision. Horizontal axis is the P_2 and P_1 is fixed to 0.3 atm. From this figure, the precision of the monitored temperature should be down to 0.01 K.

Stability of temperature in the chamber is achieved at the level of 0.1 K by both air circulation by air cooled chillers and water cooling surrounding the cavity. Both zero field and high field experiment, we plan to set 4 wires resistance temperature detectors and monitor at several points on the outer surface of the cavity. The precision of 0.01

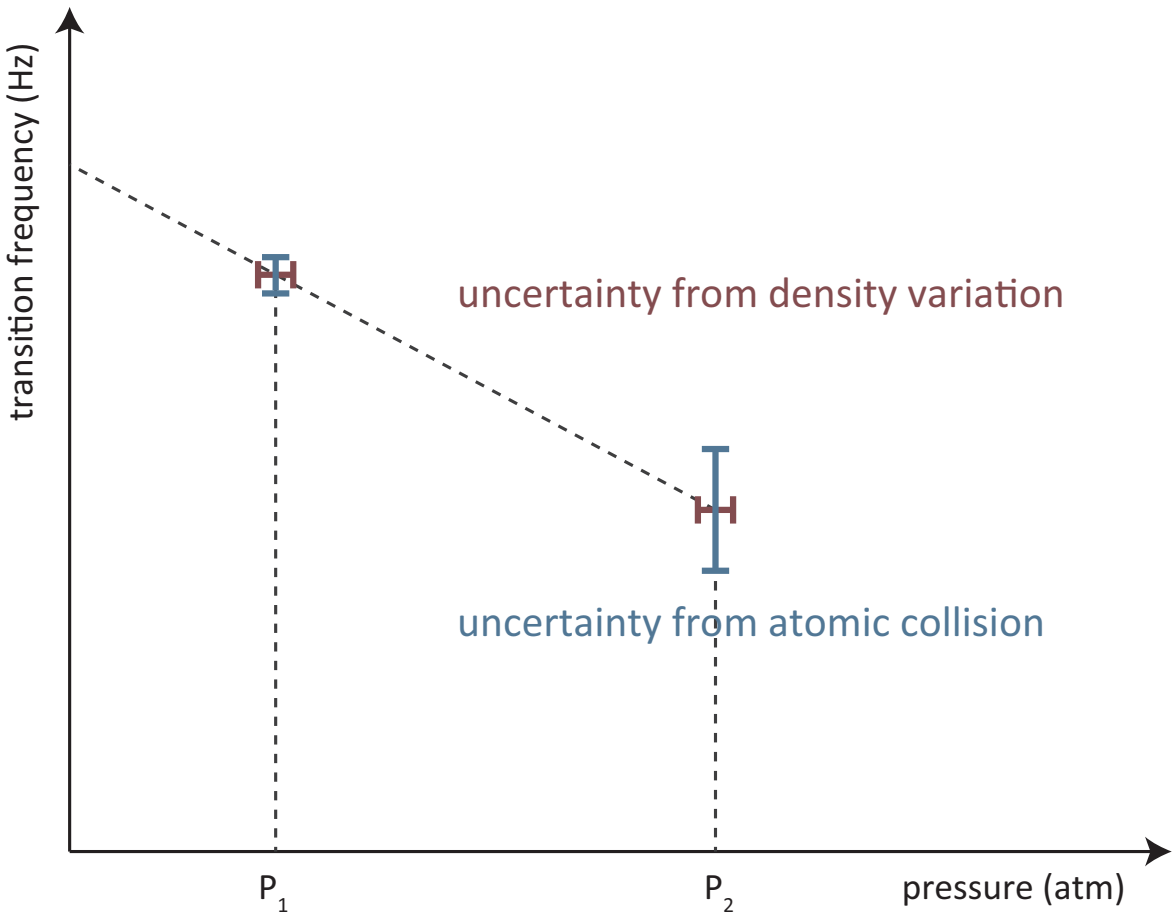

Figure 5.16: The uncertainty from temperature fluctuation has two sources, from density variation and from an atomic collision.

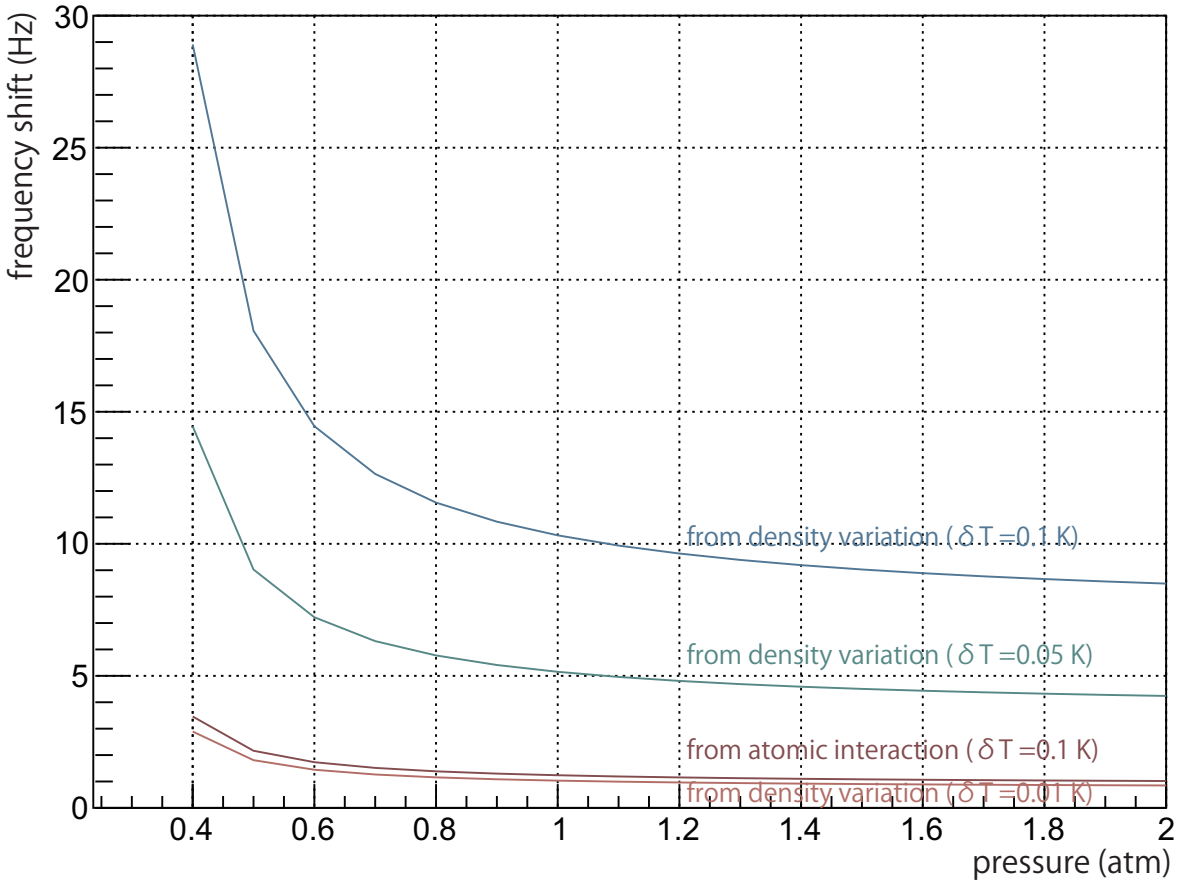

Figure 5.17: Frequency shifts from a density variation and an atomic interaction. Horizontal axis is the P_2 and P_1 is fixed to 0.3 atm.

K is enable by a commercial product such as CAB-F201, then the uncertainties from temperature can be summarized as Table 5.6.

$\delta\nu_{12}$	2 Hz
$\delta\nu_{34}$	3 Hz
$\Delta\nu_{\mathrm{HF}}$	4 Hz
$\Delta\nu_{\mathrm{ZF}}$	5 Hz
μ_μ/μ_p	11 ppb

Table 5.6: Systematic uncertainty from temperature

5.8 Muonium distribution

The muon stopping distribution is monitored by beam monitoring system. The 3-dimentional distribution can be obtained by TBPM at the precision of centimeter, the 2-dimentional projection is obtained by FBPM at the precision of millimeter (Subsection 4.10). The uncertainty from variation of muonium distribution during a RF frequency scan is estimated by using the simulation package. Figure 5.18 shows results of the estimation. In this estimation, the muonium distributions are assumed as gaussian of radial width is 3 cm and axial width is 6 cm from the result of the beam test (Subsection 4.10). According to this, the systematic uncertainty of a displacement of 1 mm in a radial direction is 4 Hz even in the worst case. Since RF field is uniform in an axial direction, the systematic uncertainty from displacement in an axial direction is negligible.

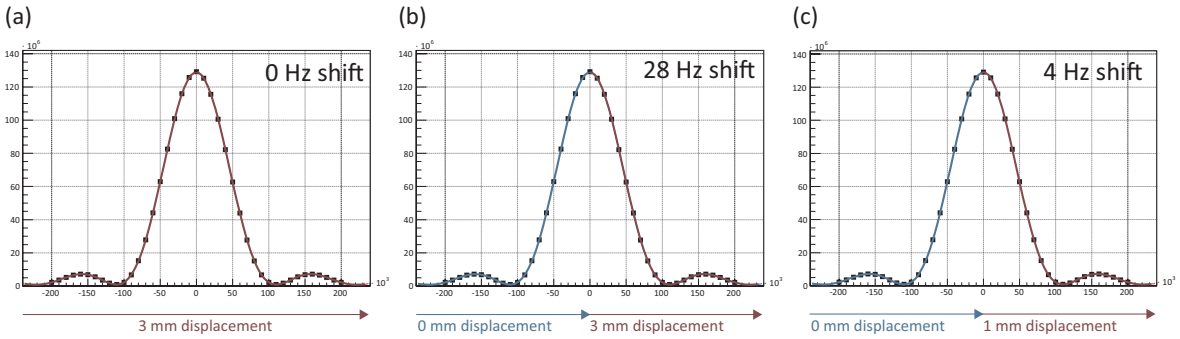

Figure 5.18: Results of the estimation in case of that (a) muonium distributions are constantly displaced of 3 mm in a radial direction, (b) muonium distributions are displaced of 3 mm in a radial direction at higher frequency than the center value, (c) muonium distributions are displaced of 1 mm in a radial direction at higher frequency than the center value.

$\delta\nu_{12}$	4 Hz
$\delta\nu_{34}$	5 Hz
$\Delta\nu_{\mathrm{HF}}$	9 Hz
$\Delta\nu_{\mathrm{ZF}}$	7 Hz
μ_μ/μ_p	127 ppb

Table 5.7: Systematic uncertainty from muonium distribution

5.9 Magnetic field

5.9.1 High field experiment

Dependence of a precision of magnetic probes

Magnetic field in the high field experiment is measured by NMR probe developed by K. Sasaki, Y. Ueno and T. Mizutani and others. (Subsection 4.12.1). We measure the NMR frequency not of free protons but of protons in a sample. The magnetic field at the location of the protons, H_p, deviates from the external field H_0,

$$H_p = (1 - \delta_t)H_0, \tag{5.17}$$

in which δ_t is the shielding constant expressed as

$$\delta_t = \sigma(H_2O) + \delta_b + \delta_p + \delta_s[68], \tag{5.18}$$

where $\sigma(H_2O)$ is from the internal diamagnetic shielding in the water molecule, δ_b is from bulk diamagnetism of the water sample which depends on the shape of the sample, δ_p is from paramagnetic impurities in the water sample, δ_s is from paramagnetic and diamagnetic materials nearby.

The value for $\sigma(H_2O)$ has been measured by comparing the NMR frequency of a spacial pure water sample with the frequency of a hydrogen maser in the same magnetic field as

$$\sigma(H_2O) = 25.680(25) \times 10^{-6}[69], \tag{5.19}$$

at a temperature $T = 25°\mathrm{C}$. The measured temperature dependence of σ is

$$\frac{\mathrm{d}\sigma(H_2O)}{\mathrm{d}t} = -10.36(30) \times 10^{-9}/°\mathrm{C}[70]. \tag{5.20}$$

Shape effect δ_b is improved from the previous experiment by using a cylindrical water container instead of spherical container. The value is estimated by OPERA[71] which is simulation software for magnetic field as -4.525 ppm.

Effect from paramagnetic impurities in the water sample δ_p can be neglected by using a ultra-pure water (Milli-Q by Merckmillipore).

Effects from paramagnetic and diamagnetic materials nearby are 0.08 ppb for Pyrex tube, 0.046 ppb cupper pipe, can be neglected for modulation coil.

On the other hand, the precision of the measured NMR frequency of 60 ppb is limited by the fitting to obtain the phase difference between the NMR signal and the signal of field modulation.

Dependence of a precision of field calculation

Magnetic field distributions after shimming are calculated by assuming certain number of magnetic moments surrounding the muonium distribution. The distribution is in

good agreement with the result of magnetic field scan in a region of spheroid surface (z =380 mm, r= 140 mm) (Figure 5.19).

Dependence of a magnetic field distribution

As shown in Figure 5.19, the peak to peak fluctuation of the magnetic field is 1.3 μT of the region. The systematic uncertainty from the magnetic field distribution can be estimated from the histogram of magnetic field effect on muoniums (Figure 5.20). The result is

$$\Delta\nu_{12} = \pm 7 \text{ Hz}. \tag{5.21}$$

ν_{HF} is obtained by equation $\nu_{\mathrm{HF}} = \nu_{12} + \nu_{34}$, thus the uncertainty of ν_{HF} is not depend on the absolute values of magnetic field in measurement of ν_{12} and ν_{34}.

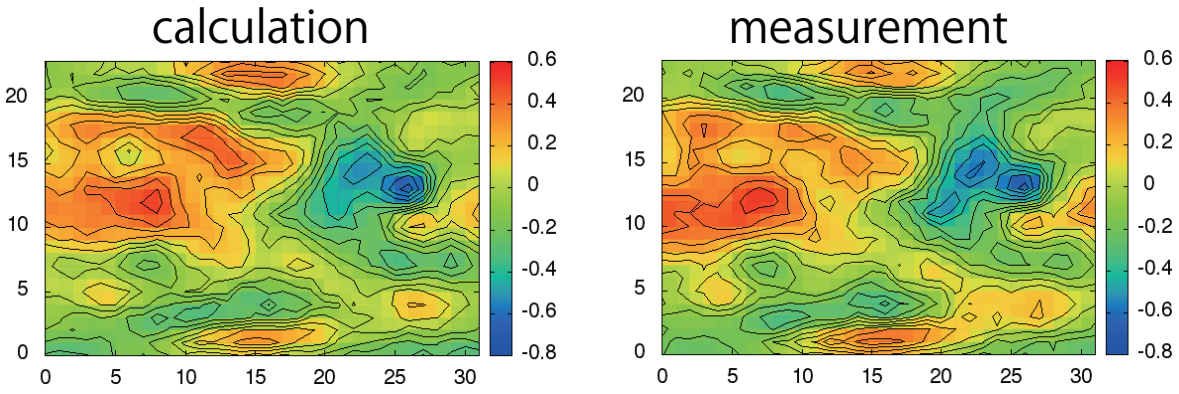

Figure 5.19: Comparison of magnetic field after shimming by calculation and measurement in a region of spheroid surface (z =380 mm, r= 140 mm).

5.9.2 Zero field experiment

Systematic uncertainty from a leakage magnetic field in a magnetic shield can estimate using a field maps by AMAZE simulation (Subsection 4.8.3) and muonium distribution. The systematic uncertainty from the analysis is

$$\Delta\nu = 9.7 \times 10^2 \pm 1.0 \times 10^2 \text{ Hz}. \tag{5.22}$$

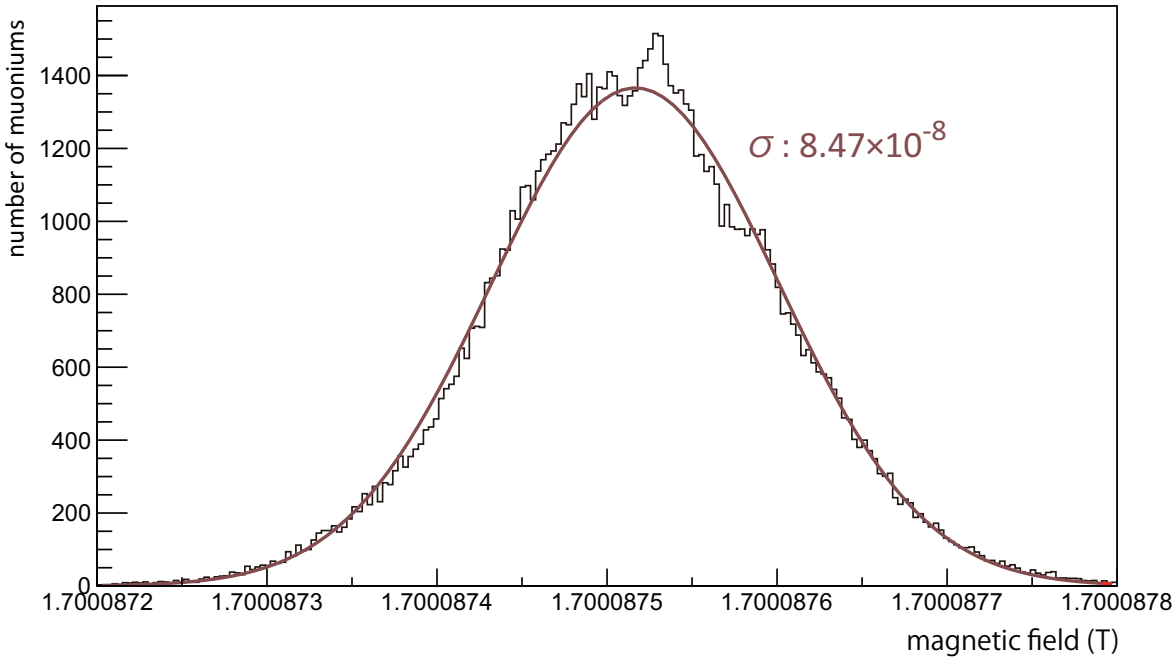

Figure 5.20: A histogram of magnetic field effect on muoniums. The number of the muons for each histograms is 10^9. The red line shows a result of Gaussian fitting and standard deviation is 8.47×10^{-8} T which correspond to 7 Hz frequency shift of ν_{12} transition.

To improve it, correction of using a scanning data of a magnetic field and Breit-Rabi formula (Equation 2.26, 2.27) is effective. Then, remained uncertainties from magnetic field is caused by dependence of a precision of fluxgate and a scan interval of magnetic fields (Figure 5.21).

Dependence of a scan interval of magnetic fields

If we adopt a nearest neighbor method to analyze a magnetic field from scanning result, there is a systematic uncertainty from a scan interval of magnetic fields. If both of scan interval of magnetic fields and muonium distributions are 30 mm, the uncertainty from the scan interval is

$$\Delta\nu = 19 \text{ Hz}. \tag{5.23}$$

Dependence of a precision of a fluxgate

Magnetic fields in the chamber are scanned by a fluxgate before measurements, and fixed monitored during measurements. The precision of fluxgate is 50 nT. The uncertainty from both the scan interval and the precision of a fluxgate is

$$\Delta\nu = 32 \text{ Hz}. \tag{5.24}$$

$\delta\nu_{12}$	11 Hz
$\delta\nu_{34}$	11 Hz
$\Delta\nu_{\mathrm{HF}}$	10 Hz
$\Delta\nu_{\mathrm{ZF}}$	32 Hz
μ_μ/μ_p	48 ppb

Table 5.8: Systematic uncertainty from magnetic field

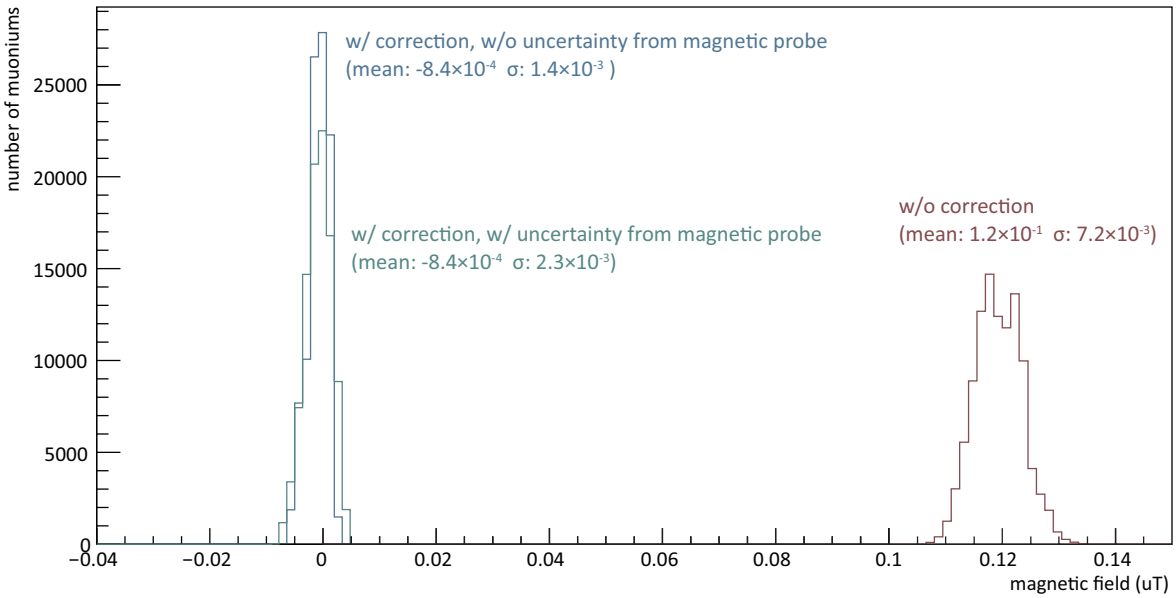

Figure 5.21: Histograms of magnetic field effect on muoniums. The number of the muons for each histograms is 10^9. The Red line shows a histogram without correction, the blue line shows a histogram with correction by the magnetic field scan data of 30 mm interval, but without 50 nT uncertainty from magnetic probe, the green line shows a histogram with correction and uncertainty from magnetic field. Without correction, The sub mG of magnetic field shift the transition frequencies of each muons. With correction by scanning results of the magnetic field improve the shift.

5.10 Summary of uncertainties

Figure 5.22 shows sources of uncertainty for the zero field experiment. Compared with the uncertainty of the latest experiment of 1400 Hz, this measurement can improve the experimental uncertainty by more than a factor of 10. On the other hand , Figure 5.23 shows sources of uncertainty for the high field experiment. it also improve the experimental uncertainty by a factor of 3 from the latest result at LAMPF.

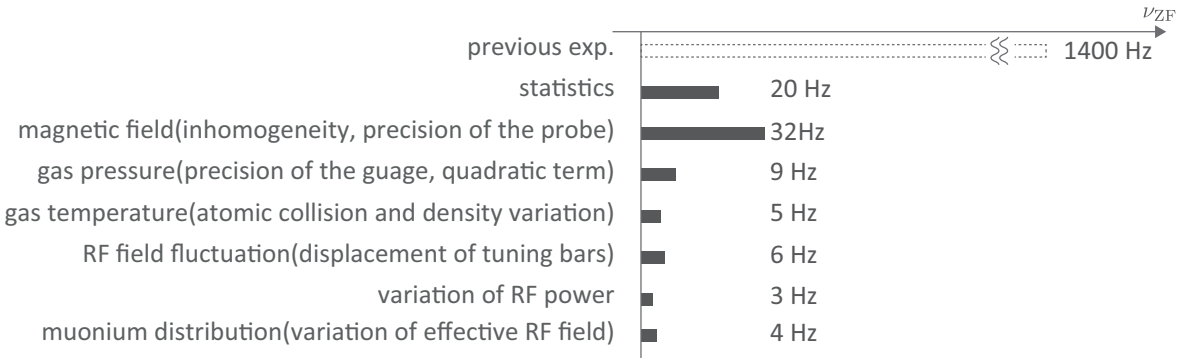

Figure 5.22: Sources of uncertainty for the zero field experiment(ν_{ZF}) are listed.

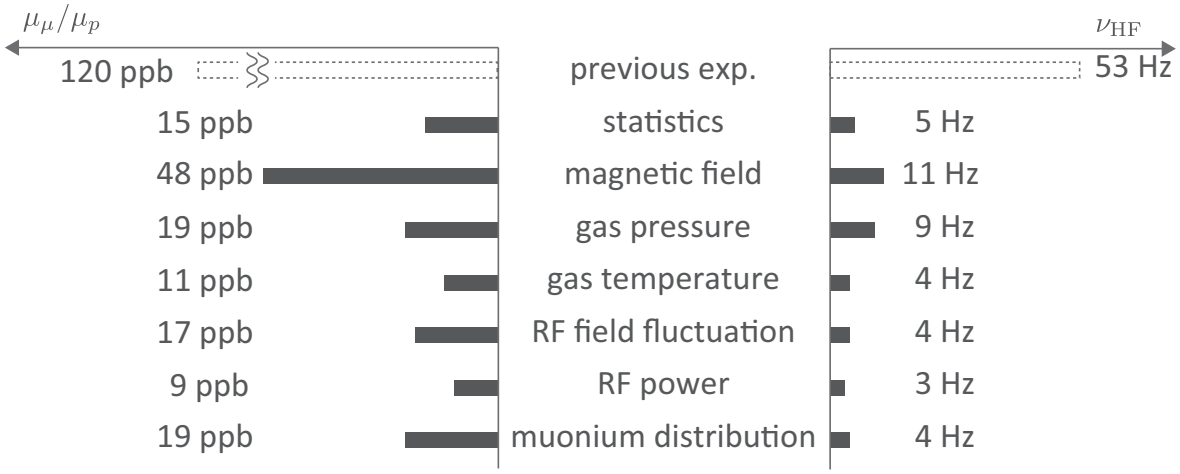

Figure 5.23: Sources of uncertainty for the high field experiment are listed. The left side of the figure shows a uncertainties of μ_μ/μ_p and right side shows a uncertainties of ν_{HF}.

Chapter 6

Discussion and conclusion

6.1 Current Status of the experiment

As described in Chapter 4, the apparatuses for experiments both in zero field and in high field have been constructed fully. As demonstrated in the discussion in Chapter 5, we are confident that all systematic uncertainties are well under control, and one day of beam time at J-PARC MUSE will supersede the precision of latest measurement of muonium HFS in a zero magnetic field. One week of beam time will supersede the precision in a high magnetic field. We had a plan to carry out the zero-field experiment at MUSE D Line in last November, but the beam time was aborted because of a trouble in J-PARC accelerator complex. We envisage the resumption of the experiment in early 2016 after restoration of the delivery of muon beams. The first beam at H Line is expected in late fiscal year 2016. The preparation of the high-field experiment is under way so that we can start the experiment right after the completion of the beam line.

6.2 Future prospects

Two possibilities are currently being considered to improve the systematic uncertainties of the experiment. One possibility is to measure both ν_{12} and ν_{34} transitions in a so-called “magic field”, which is about 1.137 T. Under this magnetic field, the magnetic

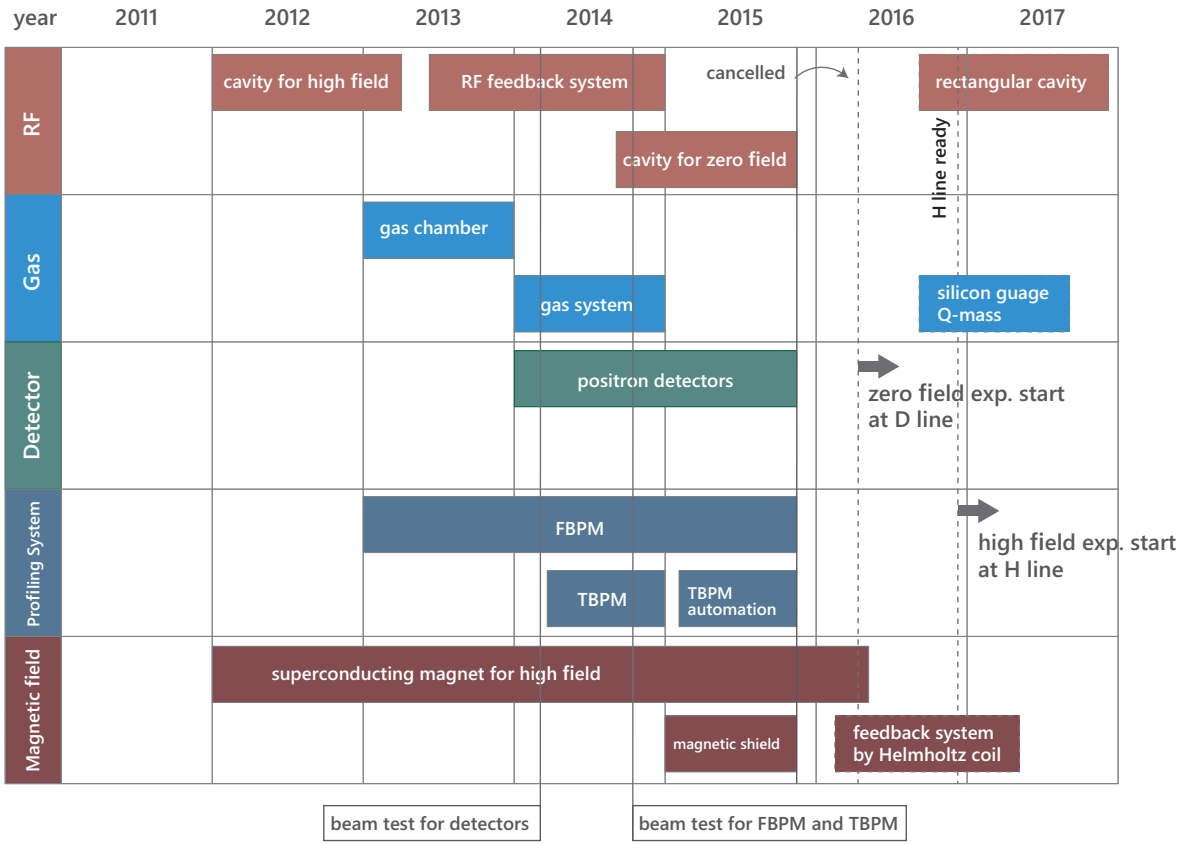

Figure 6.1: A road map of the experiment. Zero field experiment will be start in 2016 and high field experiment in 2017.

field dependences of both ν_{12} and ν_{34} becomes negligible (See Figure 6.2), thus the uncertainty on $\frac{\mu_\mu}{\mu_p}$ from the uncertainty of the field strength disappears as shown in Equation 2.26 and 2.27. We are currently designing a rectangular cavity which have two resonance frequencies which match ν_{12} and ν_{34}, because cylindrical cavities like the one described in Section 4.1 cannot have satisfying resonance modes. Figure 6.3 shows electric fields and magnetic fields of the TM120 and TM210 mode of the rectangular cavity(The TM mnp mode in a rectangular cavity is characterized by three subscripts m, n and p that corresponding to the number of half wave variations in x, y, z). Thus resonance frequencies of TM120 and TM210 can be tuned for both nu_{12} and ν_{34} transition frequencies by adjusting the length and width of the cavity.

If successful, we plan to measure the frequencies under the magic field after the high field experiment. Another possibility is use a mixture of krypton and helium gases as the target to reduce the uncertainty due to the pressure shift. According to a study, the pressure shift of hyperfine splitting of hydrogen atom in helium gas is

$$a_{He} = +3.7 \times 10^9 \text{ mmHg}^{-1}[72], \tag{6.1}$$

which is positive, while the frequency shift in krypton is negative. If the pressure shift for muonium atom is also positive in helium, there is a possibility that by mixing krypton and helium, we can eliminate the pressure shift. Helium is a rare gas, so that depolarization of muonium due to interaction with helium atom is negligible. There is no previous report of pressure shift for muonium atom in helium, so we are currently investigating theoretical models, and possibility to measure it by ourselves.

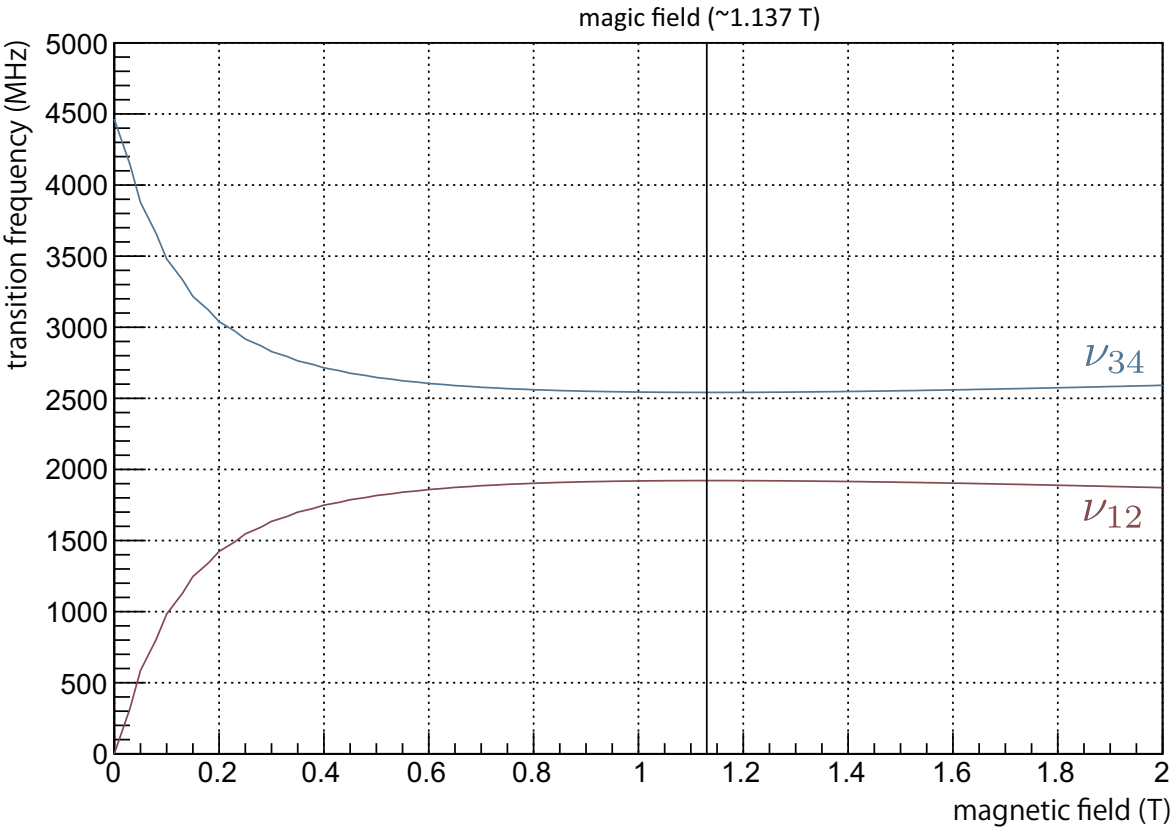

Figure 6.2: A relation between ν_{ij} and a magnetic field. In magic field, measured ν_{ij}(H) is independent to field changes δB.

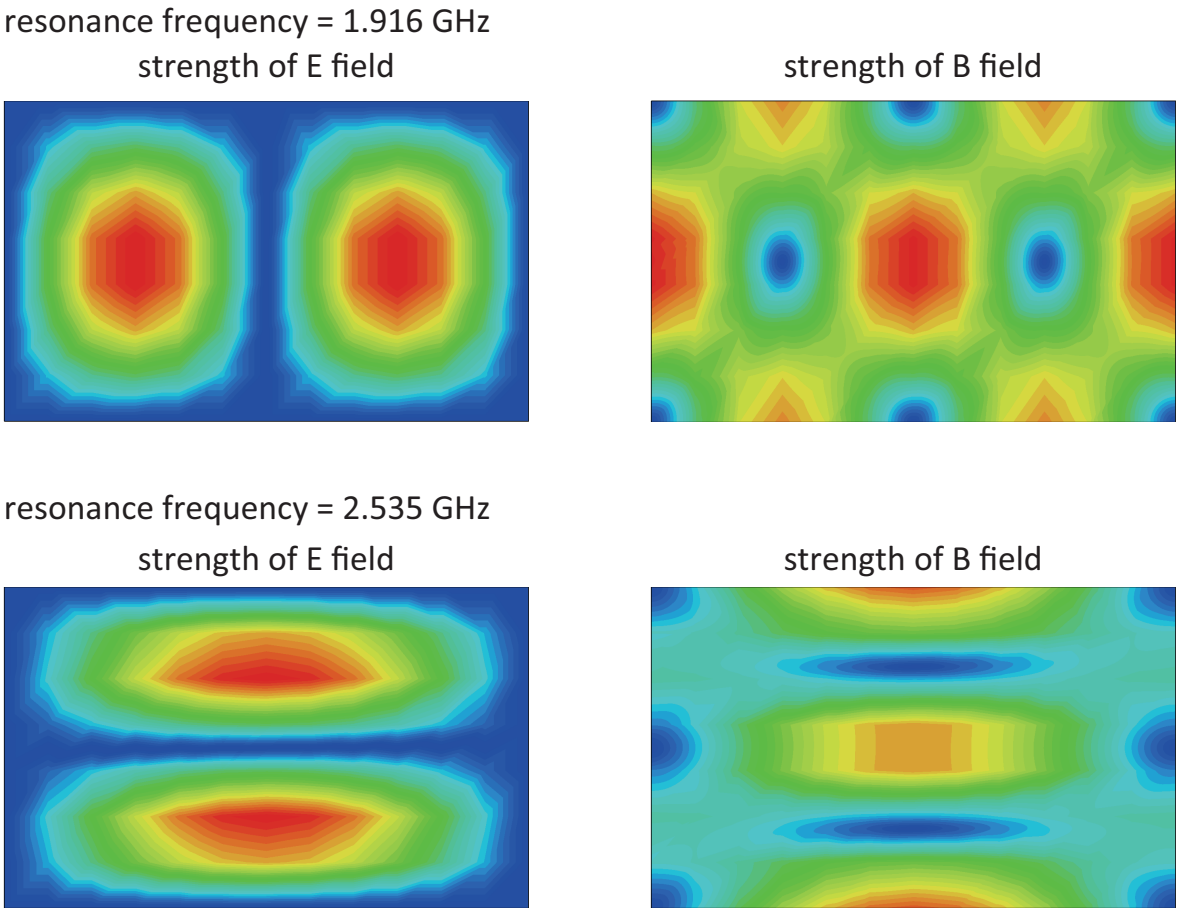

Figure 6.3: Electric fields and magnetic fields of the TM120 and TM210 mode of the rectangular cavity. the length of the cavity is 205 mm and the width is 123 mm to adjust both resonance frequencies of the TM120 and the TM210 to nu_{12} and ν_{34} transition frequencies at 1.137 T magnetic field.

Appendix A

RF fields of the TM110 mode and the TM210 mode

The amplitudes of the microwave electromagnetic field in the cavity are

$$H_r = -H_{110}\frac{J_1(x_{11}\frac{2r}{D})}{x_{11}\frac{2r}{D}}\sin\phi, \tag{A.1}$$

$$H_\phi = -H_{110}J_1'(x_{11}\frac{2r}{D})\cos\phi, \tag{A.2}$$

$$E_z = E_{110}J_1(x_{11}\frac{2r}{D})\cos\phi. \tag{A.3}$$

for the TM110 mode and

$$H_{1r} = -H_{210}\frac{2J_2(x_{21}\frac{2r}{D})}{x_{21}\frac{2r}{D}}\sin 2\phi, \tag{A.4}$$

$$H_{1\phi} = -H_{210}J_2'(x_{21}\frac{2r}{D})\cos 2\phi, \tag{A.5}$$

$$E_z = E_{210}J_2(x_{21}\frac{2r}{D})\cos 2\phi. \tag{A.6}$$

for the TM210 mode, in which H_{mnp} and E_{mnp} are amplitude, r is the radial coordinate and ϕ is the azimuthal angle measured with respect to the position of the input loop.

The microwave power spatial distribution is proportional to

$$H_1^2(r,\phi) = H_{1r}^2(r,\phi) + H_{1\phi}^2(r,\phi). \tag{A.7}$$

and Figure A.1 (A.2) and shows a radial cross sectional view of microwave power of the TM110 (TM210) mode.

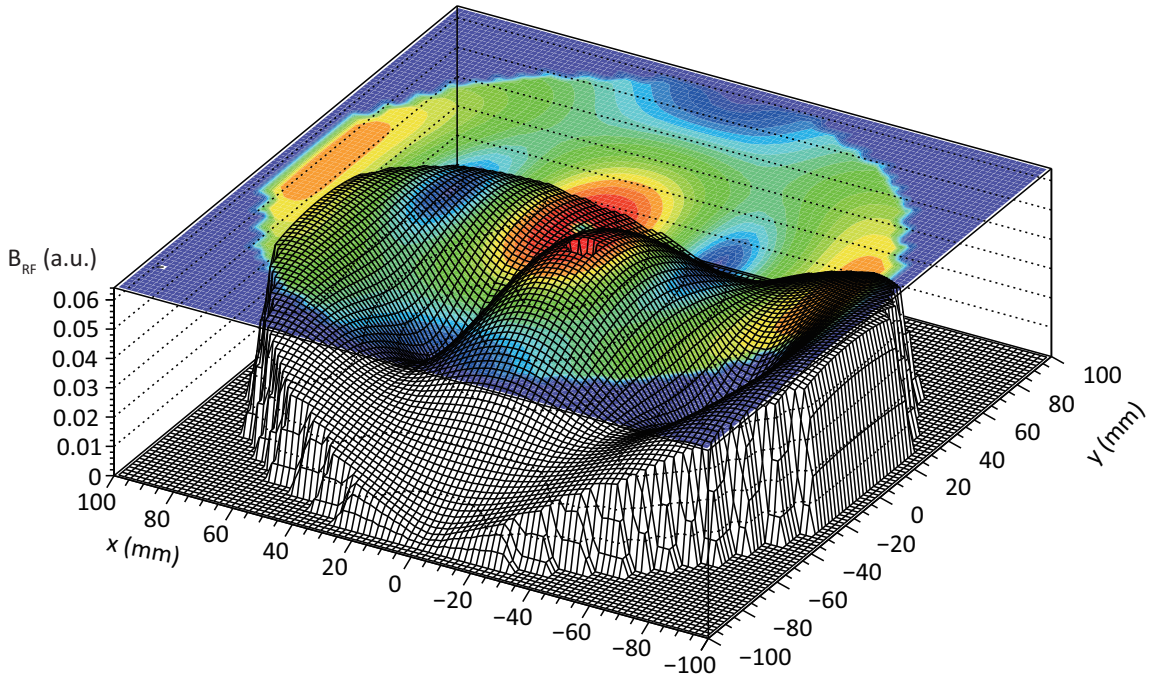

Figure A.1: Radial cross sectional view of microwave power of the TM110 mode.

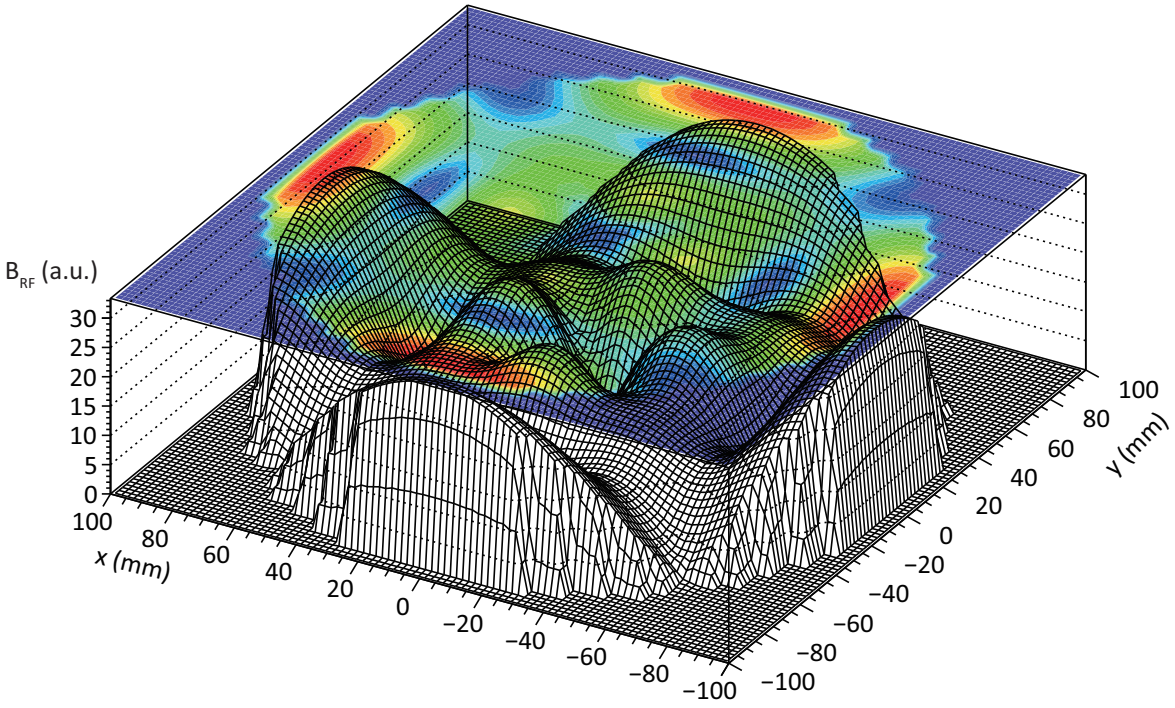

Figure A.2: Radial cross sectional view of microwave power of the TM210 mode.

Appendix B

Network Analyzer

A network analyzer is used for monitoring RF power in the cavity. It measures a reflecting and transmitting power as S-parameter. Frequency range of the network analyzer is 5 Hz to 3 GHz which is enough for this measurement. The input power is set to -10 dBm.

S-parameter

The S-parameter of 2-port network is expressed as

$$\begin{pmatrix} b_1 \\ b_2 \end{pmatrix} = \begin{pmatrix} S_{11} & S_{12} \\ S_{21} & S_{22} \end{pmatrix} \begin{pmatrix} a_1 \\ a_2 \end{pmatrix}, \tag{B.1}$$

where a_n is normalized amplitude of incident wave and b_n that of exiting wave defined as

$$a_i = \frac{V_{Ii}}{\sqrt{Z_R}}, \tag{B.2}$$

$$b_i = \frac{V_{Ri}}{\sqrt{Z_R}}. \tag{B.3}$$

where V_{Ii} is a voltage wave incident on each port, V_{Ri} is a voltage wave reflected from each port and Z_R is a reference impedance. In most cases including this network analyzer, the reference impedance is set to 50 Ω.

S_{mn} represent

- S_{11}: reflection coefficient of input port,
- S_{12}: reverse voltage gain,
- S_{21}: forward voltage gain,
- S_{22}: reflection coefficient of output port.

The measurement using network analyzer takes two steps. At first, input antennas should be tuned for resonance frequencies. It is taken as synonymous with that an input impedance is equivalent to reference impedance at resonance frequencies. Using Equation B.1, B.2 and B.3, the cavity impedance is described as

$$Z_I = Z_R \frac{1 + S_{11}}{(1 - S_1)}, \tag{B.4}$$

where Z_I is a input impedance and Z_R is a reference impedance. Thus coupling of input port is able to confirmed by S_{11}.

Secondly, RF power in the cavity is monitored S_{21} by RF input and output ports. RF power in the cavity is usually expressed as a Q factor which is described in Section B. When a input port couple to the cavity, the Q factor of the cavity is equivalent to Q_{ext} which is described in Section B [73]. Thus RF power in the cavity can be monitored by S_{21}.

Quality factor

Q factor is defined by two ways: in terms of the ratio of the energy and in terms of bandwidth.

Defined in terms of the ratio of the energy

RF energy stored in the cavity is expressed by a Quality factor (Q factor). It is defined as

$$Q = \frac{\omega_0 W}{P}, \tag{B.5}$$

where ω_0 is the resonance frequency, W is the energy stored in the cavity and P is the energy loss rate per unit time from the cavity. Designing the high Q cavity is same meaning as minimization of power losses in the cavity.

There are several types of Q factors:

- unloaded Q (Q_0),
- conductive Q (Q_c),
- external Q (Q_ext),
- dielectric Q(Q_d),
- loaded Q (Q_L).

where Q_c is result from the power loss in the walls which have finite conductivity. The absorbed power due to surface losses is calculated as

$$P_\mathrm{c} = \frac{1}{2}\sqrt{\frac{\pi\mu f}{\sigma}} \int |H|^2 \partial S, \tag{B.6}$$

where σ is the surface current density and f is the resonance frequency. Since the dominant part of the P_c is from the surface current flow between the components of the cavity, joint strength of them is important for high Q factor.

Q_ext is result from power loss through unclosed surfaces (holes) of the cavity. In case of our cavity, there are RF input and output ports and the ports for tuning bars as unclosed surfaces. To avoid the power loss, coupling of the input port which transports RF power should be strong, but the coupling of other RF ports should be weak and the size of the ports for tuning bars should be small as far as possible.

Q_d is result from the power loss in the lossy dielectric material which is described as

$$P_\mathrm{d} = \pi f \tan\delta \epsilon_0 \epsilon_r \int |E|^2 \partial V, \tag{B.7}$$

where ϵ_0 is the vacuum permittivity, ϵ_r is the electric permittivity and $\tan\delta$ is the dielectric tangent (see Section 4.1.5). This equation indicates that the power loss caused by the dielectric material depends on the dielectric tangent, the electric permittivity and the volume of the material. Since the sweep range of the tuning bar depends electric permittivity and the volume the material but not the dielectic tangent, a material which has low dielectirc tangent is good for Q factor.

Unloaded Q (Q_0) which is contained Q_d and Q_c but excluded Q_ext can be found as

$$\frac{1}{Q_0} = \frac{1}{Q_c} + \frac{1}{Q_d} \text{ [58].} \tag{B.8}$$

Loaded Q (Q_L) contained all parts of Q factor can be found as

$$\frac{1}{Q_\mathrm{L}} = \frac{1}{Q_\mathrm{c}} + \frac{1}{Q_\mathrm{ext}} \text{ [58].} \tag{B.9}$$

Thus the energy loss in the cavity is caused by the combination of the surface current on the cavity, microwave absorption by the dielectric material and the power loss through unclosed surfaces of the cavity.

Defined in terms of bandwidth

The other common definition of the Q factor is in terms of bandwidth. RF cavity can be regard as a parallel RLC circuit. A voltage of the parallel RLC circuit is expressed as

$$V(t) = \frac{1}{[R^{-2} + (\omega C - 1/(\omega L))^2]^{1/2}} \exp j(\omega t - \phi). \tag{B.10}$$

P is defined as

$$P = \frac{V^2}{R}. \tag{B.11}$$

According to B.10 and B.11,

$$P = \frac{1}{2} \frac{RV^2}{R^2 + (\omega L - 1/(\omega C))^2}. \tag{B.12}$$

When the consumption energy P is equivalent to half of consumption energy at the resonance point, the following equation holds;

$$\frac{RV^2}{2(R^2 + (\omega L - 1/(\omega C))^2} = \frac{V^2}{4R}. \tag{B.13}$$

FWHM (full width at half maximum) $\Delta\omega$ is calculated by ω_1 and ω_2 satisfy B.13,

$$\Delta\omega = \omega_2 - \omega_1 \tag{B.14}$$

$$= \sqrt{C/L} R\omega_0 = \frac{\omega_0}{Q}. \tag{B.15}$$

Thus Q factor also expresses a FWHM of a RF cavity. As mentioned Section B, Q_L of the cavity is equivalent to Q_{ext} when the cavity and a input port is coupled. The reason is that main part of Q_{ext} is result from the output port, Q_L is able to obtained by a FWHM of a S_{21}.

Calibration of Network Analyzer

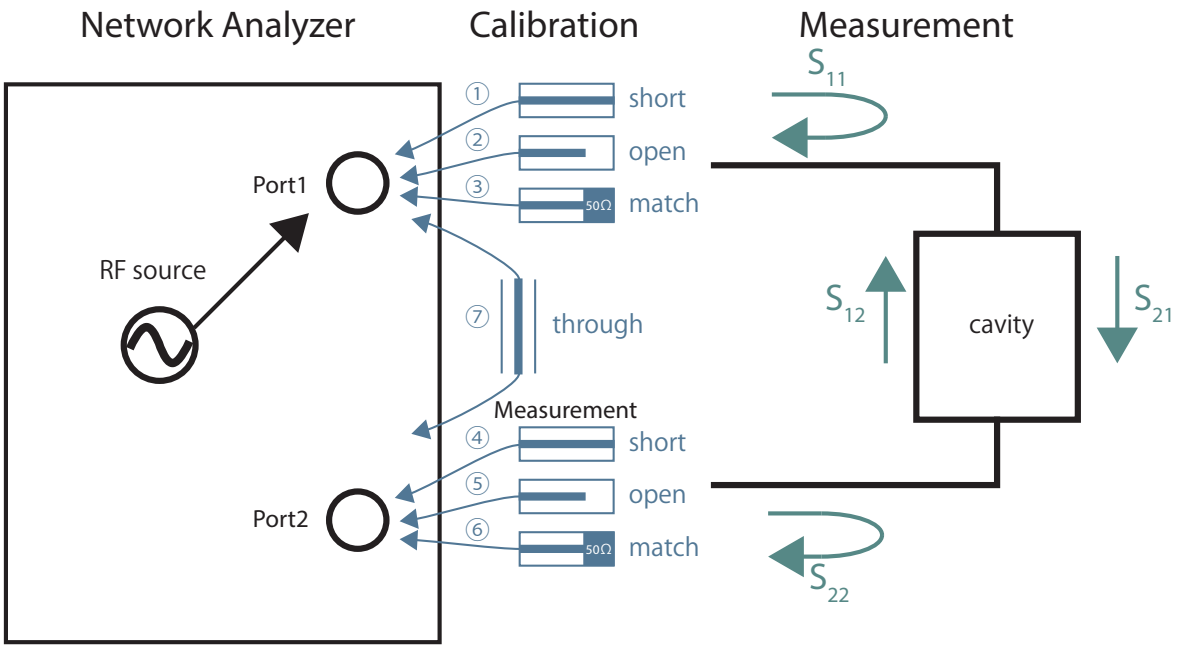

Figure B.1: A process of TOSM calibration and the measurement of S-parameter using the network analyzer.

Network analyzer can be plagued by three types of errors:

1. Systematic errors,
2. Random errors,
3. Drift errors.

And there are 6 types of systematic error:

1. Directivity and crosstalk errors relating to signal leakage,
2. Source and load impedance mismatches relating to reflections,
3. Frequency response errors caused by reflection and transmission tracking within the test receivers.

For preventing these errors, network analyzer should be calibrated each time measuring condition is changed. Random errors vary randomly as a function of time. Main contributor is noises of instruments. It is not solved by calibration. Drift errors occur mainly by variation of temperature and can be reduced by constant recalibration.

TOSM (Through-Open-Short-Match) calibration is a typical type of calibration to determine the 6 systematic error terms for each signal direction. It measures the open, short, and match one port standard on both ports and the through between them (see Figure B.1).

1. Open: Transmission line terminated with open. A reflected voltage keeps in phase with an incident voltage.

2. Short: Transmission line terminated with short. A reflected voltage is opposite phase with an incident voltage.

3. Match: Transmission line terminated with reference impedance. All the incident power is absorbed in the load.

4. Through: Transmission line connected port1 and port2 directly. Through is calibrate an amplitude and phase variation of transmission characteristic.

Appendix C

CST microwave studio

Unlike an ideal cylindrical cavity, simulation using finite element method is needed to evaluate the cavity considering a structure of RF ports and tuning bars. CST microwave studio [8] is a one of such software for the 3D EM simulation of high frequency components. There are several solvers are available. Among them, following two solvers are mainly used.

C.1 Overview of solvers

C.1.1 Eigenmode Solver

The Eigenmode Solver is dedicated to the simulation of closed resonant structures. It is for estimate the electromagnetic field of resonance modes and Q factor (see Chapter B).

C.1.2 Frequency Domain Solver

The general purpose Frequency Domain Solver solves the problem for a single frequency at a time, and for a number of adaptively chosen frequency samples in the course of a frequency sweep. The solution comprises the field distribution as well as the S-parameters (see Appendix B) at the given frequency so that it is appropriate solver

for compared with the line shapes of S-parameter obtained from network analyzer (see Appendix B).

C.2 Dependence of number of mesh

Figure C.1 shows resonance frequencies in a simulation with a different numbers of mesh. Mesh views are shown in Figure C.2. According to both figrures, simulation results with less than about 10^5 meshes are not consistent with measurement, since small components such as RF antennas can not be considered.

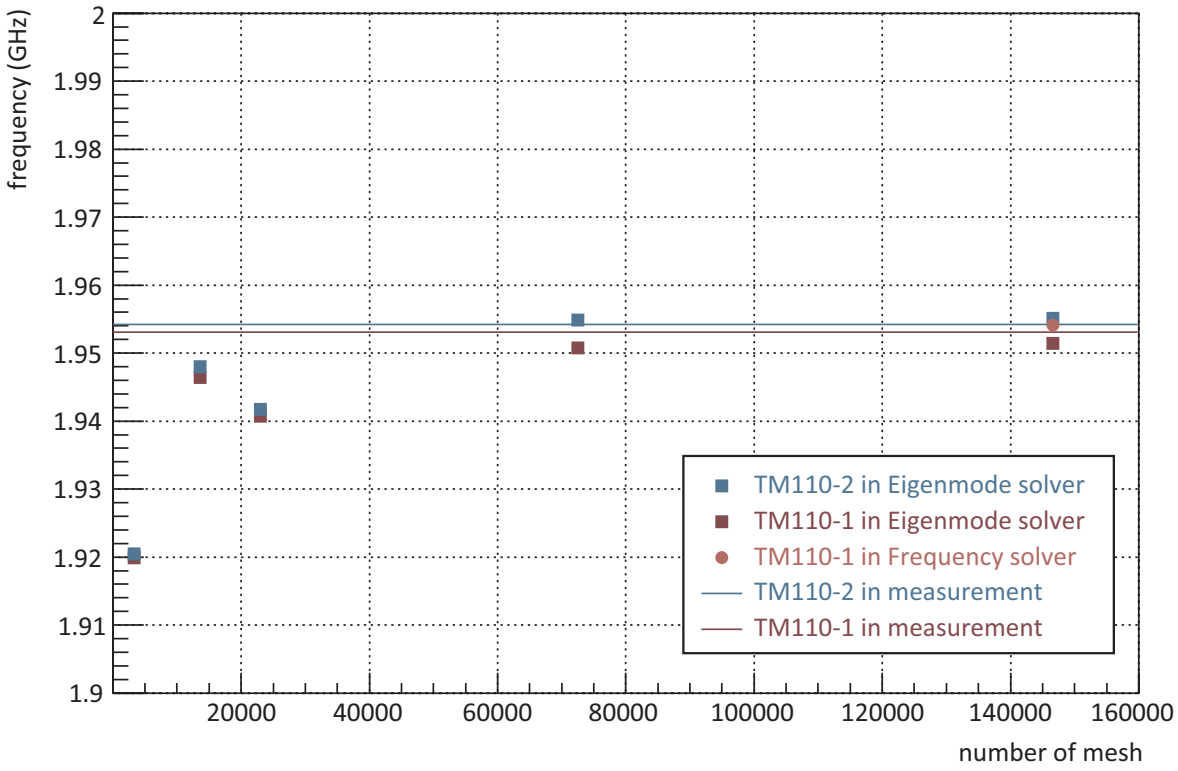

Figure C.1: Resonance frequencies in a simulation with a different numbers of mesh.

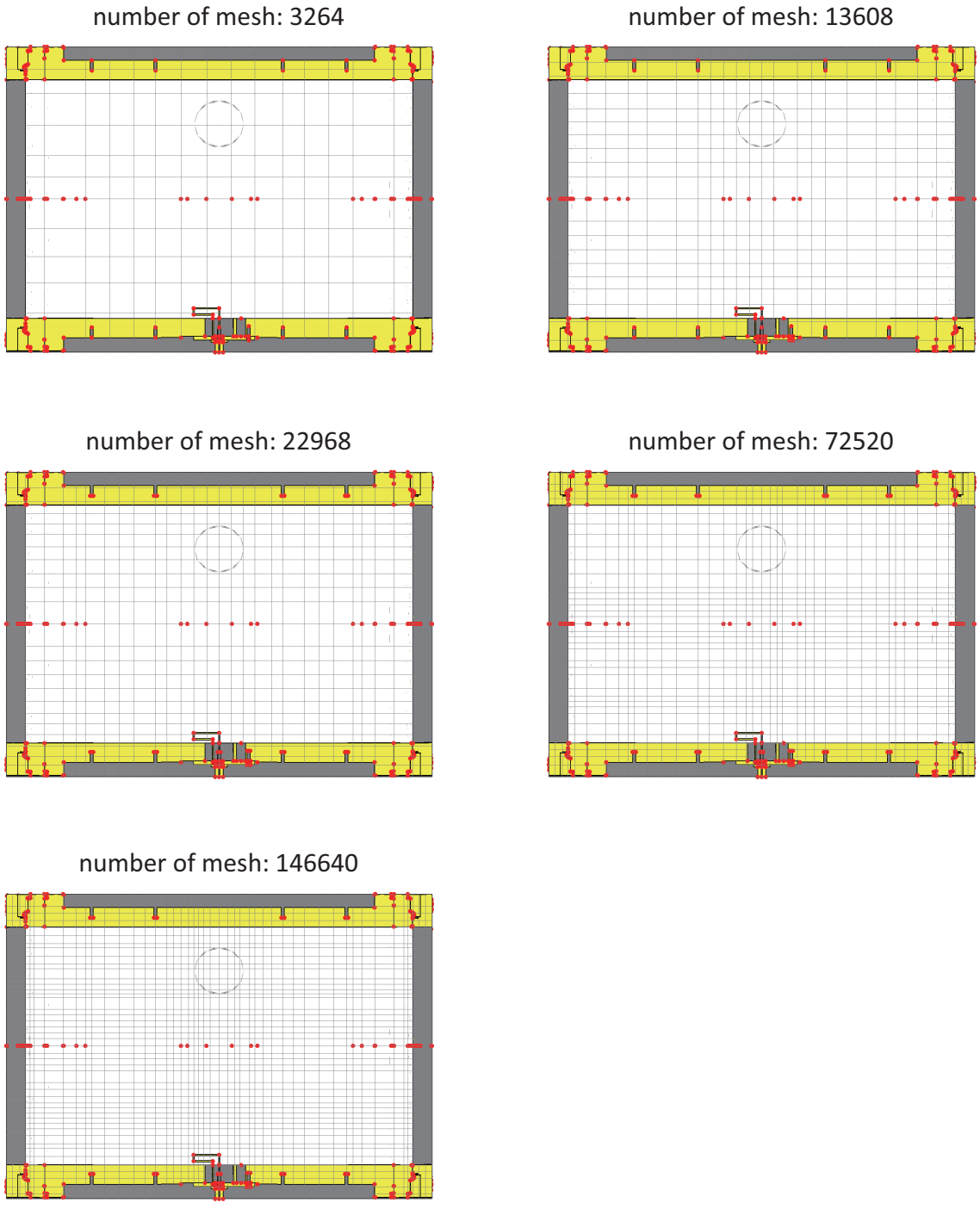

Figure C.2: Mesh views with different numbers of mesh. The geometry is imported from Autodesk Inventor Professional.

Bibliography

[1] P. J. Mohr, B. N. Taylor, and D. B. Newell. CODATA recommended values of the fundamental physical constants: 2010. *Reviews of Modern Physics*, 84:1527–1605, Nov 2012.

[2] K. Hagiwara, R. Liao, A. D. Martin, D. Nomura, and T. Teubner. $(g-2)_\mu$ and $\alpha(M_Z^2)$ re-evaluated using new precise data. *Journal of Physics G*, 38:085003, 2011.

[3] V. W. Hughes, M. G. Perdekamp, D. Kawall, W. Liu, K. Jungmann, and G. z. Putlitz. Test of CPT and Lorentz Invariance from Muonium Spectroscopy. *Physical Review Letters*, 87:111804, Aug 2001.

[4] W. Liu, M. G. Boshier, S. Dhawan, O. v. Dyck, P. Egan, X. Fei, M. Grosse Perdekamp, V. W. Hughes, M. Janousch, K. Jungmann, D. Kawall, F. G. Mariam, C. Pillai, R. Prigl, G. z. Putlitz, I. Reinhard, W. Schwarz, P. A. Thompson, and K. A. Woodle. High Precision Measurements of the Ground State Hyperfine Structure Interval of Muonium and of the Muon Magnetic Moment. *Physical Review Letters*, 82:711–714, Jan 1999.

[5] N. Kawamura, K. Ninomiya, H. Fujimori, Y. Kobayashi, K.Nishiyama, and Muon Sci. Sec. Improvement of Muon Beam Transport at D-line. *KEK-MSL Progress Report 2010*, 2011.

[6] N. Kawamura, MuHFS collab., DeeMe collab., and g-2/EDM collab. Present Status of the H-Line. *MLF ANNUAL REPORT 2013*, 2014.

[7] https://geant4.web.cern.ch/geant4/.

[8] http://www.cst.com/.

[9] V.W.Hughes and G. Putlitz. *Quantum electrodynamics*. Advanced series on directions in high energy physics. World Scientific, 1990.

[10] D. G. Fleming, R. J. Mikula, and D. M. Garner. μ^+ charge exchange and muonium formation in low-pressure gases. *Physical Review A*, 26:2527–2544, Nov 1982.

[11] R. M. Mobley, J. J. Amato, V. W. Hughes, J. E. Rothberg, and P. A. Thompson. Muonium Chemistry II. *The Journal of Chemical Physics*, 47(8):3074–3075, 1967.

[12] R. M. Mobley, J. M. Bailey, W. E. Cleland, V. W. Hughes, and J. E. Rothberg. Muonium Chemistry. *The Journal of Chemical Physics*, 44(11):4354–4355, 1966.

[13] C. G. Parthey, A. Matveev, J. Alnis, B. Bernhardt, A. Beyer, R. Holzwarth, A. Maistrou, R. Pohl, K. Predehl, T. Udem, T. Wilken, N. Kolachevsky, M. Abgrall, D. Rovera, C. Salomon, P. Laurent, and T. W. Hänsch. Improved Measurement of the Hydrogen $1S - 2S$ Transition Frequency. *Physical Review Letters*, 107:203001, Nov 2011.

[14] H. Hellwig, R. F. C. Vessot, M. W. Levine, P. W. Zitzewitz, D. W. Allan, and D. J. Glaze. Measurement of the Unperturbed Hydrogen Hyperfine Transition Frequency. *IEEE Transaction on Instrumentation and Measurement*, 19(4):200–209, nov. 1970.

[15] N. F. Ramsey. Experiments with trapped hydrogen atoms and neutrons. *Hyperfine Interactions*, 81:97–103, 1993.

[16] M. Eides, H. Grotch, and V. Shelyuto. *Theory of light hydrogenic bound states*. Springer tracts in modern physics. Springer, 2007.

[17] M. W. Ritter, P. O. Egan, V. W. Hughes, and K. A. Woodle. Precision determination of the hyperfine-structure interval in the ground state of positronium. V. *Physical Review A*, 30(3):1331–1338, Sep 1984.

[18] B. A. Kniehl and A. A. Penin. Order $\alpha^7 \ln(1/\alpha)$ Contribution to Positronium Hyperfine Splitting. *Physical Review Letters*, 85(24):5094–5097, Dec 2000.

[19] A. Ishida, T. Namba, S. Asai, T. Kobayashi, H. Saito, M. Yoshida, K. Tanaka, and A. Yamamoto. New precision measurement of hyperfine splitting of positronium. *Physics Letters B*, 734:338 – 344, 2014.

[20] V. Hughes and C. Wu. *Muon physics*. Number v.2 in Muon Physics. Academic Press, 1977.

[21] R. Faustov. Magnetic moment of the hydrogen atom. *Physics Letters B*, 33(6):422 – 424, 1970.

[22] M. I. Eides. Weak-interaction contributions to hyperfine splitting and Lamb shift. *Physical Review A*, 53:2953–2957, May 1996.

[23] S. G. Karshenboim. Leading logarithmic corrections and uncertainty of Muonium hyperfine splitting calculations. *Zeitschrift fur Physik D Atoms, Molecules and Clusters*, 36:11–15, 1996.

[24] A. Czarnecki, S. I. Eidelman, and S. G. Karshenboim. Muonium hyperfine structure and hadronic effects. *Physical Review D*, 65:053004, Jan 2002.

[25] R. Bluhm, V. A. Kostelecký, and C. D. Lane. *CPT* and Lorentz Tests with Muons. *Phys. Rev. Lett.*, 84:1098–1101, Feb 2000.

[26] G. W. Bennett, B. Bousquet, H. N. Brown, G. Bunce, R. M. Carey, P. Cushman, G. T. Danby, P. T. Debevec, M. Deile, H. Deng, W. Deninger, S. K. Dhawan, V. P. Druzhinin, L. Duong, E. Efstathiadis, F. J. M. Farley, G. V. Fedotovich, S. Giron, F. E. Gray, D. Grigoriev, M. Grosse-Perdekamp, A. Grossmann, M. F. Hare, D. W. Hertzog, X. Huang, V. W. Hughes, M. Iwasaki, K. Jungmann, D. Kawall, M. Kawamura, B. I. Khazin, J. Kindem, F. Krienen, I. Kronkvist, A. Lam, R. Larsen, Y. Y. Lee, I. Logashenko, R. McNabb, W. Meng, J. Mi, J. P. Miller, Y. Mizumachi, W. M. Morse, D. Nikas, C. J. G. Onderwater, Y. Orlov,

C. S. Özben, J. M. Paley, Q. Peng, C. C. Polly, J. Pretz, R. Prigl, G. z. Putlitz, T. Qian, S. I. Redin, O. Rind, B. L. Roberts, N. Ryskulov, S. Sedykh, Y. K. Semertzidis, P. Shagin, Y. M. Shatunov, E. P. Sichtermann, E. Solodov, M. Sossong, A. Steinmetz, L. R. Sulak, C. Timmermans, A. Trofimov, D. Urner, P. v. Walter, D. Warburton, D. Winn, A. Yamamoto, and D. Zimmerman. Search for Lorentz and CPT Violation Effects in Muon Spin Precession. *Phys. Rev. Lett.*, 100:091602, Mar 2008.

[27] V. A. Kostelecký and N. Russell. Data tables for Lorentz and CPT violation. *Rev. Mod. Phys.*, 83:11–31, Mar 2011.

[28] R. Pohl, A. Antognini, F. Nez, F. D. Amaro, F. Biraben, J. M. R. Cardoso, D. S. Covita, A. Dax, S. Dhawan, L. M. P. Fernandes, A. Giesen, T. Graf, T. W. Hänsch, P. Indelicato, L. Julien, C.-Y. Kao, P. Knowles, E.-O. Le Bigot, Y.-W. Liu, J. A. M. Lopes, L. Ludhova, C. M. B. Monteiro, F. Mulhauser, T. Nebel, P. Rabinowitz, J. M. F. d. Santos, L. A. Schaller, K. Schuhmann, C. Schwob, D. Taqqu, J. F. C. A. Veloso, and F. Kottmann. The size of the proton. *Nature*, 466(7303):213–216, jul 2010.

[29] S. J. Brodsky, C. E. Carlson, J. R. Hiller, and D. S. Hwang. Erratum: Constraints on Proton Structure from Precision Atomic-Physics Measurements. *Physical Review Letters*, 94:169902, Apr 2005.

[30] S. G. Karshenboim. Constraints on a long-range spin-dependent interaction from precision atomic physics. *Physical Review D*, 82:113013, Dec 2010.

[31] S. G. Karshenboim and V. V. Flambaum. Constraint on axionlike particles from atomic physics. *Physical Review A*, 84:064502, Dec 2011.

[32] S. G. Karshenboim, D. McKeen, and M. Pospelov. Constraints on muon-specific dark forces. *Physical Review D*, 90:073004, Oct 2014.

[33] V. W. Hughes, D. W. McColm, K. Ziock, and R. Prepost. Formation of Muonium and Observation of its Larmor Precession. *Physical Review Letters*, 5(2):63–65, Jul 1960.

[34] R. Prepost, V. W. Hughes, and K. Ziock. Observation of the Hyperfine Structure Splitting of Muonium by Use of a Static Magnetic Field. *Physical Review Letters*, 6(1):19–21, Jan 1961.

[35] J. M. Bailey, W. E. Cleland, V. W. Hughes, R. Prepost, and K. Ziock. Muonium. II. Observation of the Muonium Hyperfine-Structure Interval. *Physical Review A*, 3(3):871–884, Mar 1971.

[36] R. D. Ehrlich, H. Hofer, A. Magnon, D. Stowell, R. A. Swanson, and V. L. Telegdi. Determination of the Muonium Hyperfine Splitting at Low Pressure from a Field-Independent Zeeman Transition. *Physical Review Letters*, 23(10):513–517, Sep 1969.

[37] W. E. Cleland, J. M. Bailey, M. Eckhause, V. W. Hughes, R. M. Mobley, R. Prepost, and J. E. Rothberg. New Value for the Fine-Structure Constant α from Muonium Hyperfine Structure Interval. *Physical Review Letters*, 13(6):202–205, Aug 1964.

[38] W. E. Cleland, J. M. Bailey, M. Eckhause, V. W. Hughes, R. Prepost, J. E. Rothberg, and R. M. Mobley. Muonium. III. Precision Measurement of the Muonium Hyperfine-Structure Interval at Strong Magnetic Field. *Physical Review A*, 5(6):2338–2356, Jun 1972.

[39] V. W. Hughes. Muonium. *Annual Review of Nuclear Science*, 16(1):445–470, 1966.

[40] P. A. Thompson, J. J. Amato, P. Crane, V. W. Hughes, R. M. Mobley, G. z. Putlitz, and J. E. Rothberg. Determination of Muonium Hyperfine Structure Interval Through Measurements at Low Magnetic Fields. *Physical Review Letters*, 22(5):163–167, Feb 1969.

[41] R. D. Ehrlich, H. Hofer, A. Magnon, D. Y. Stowell, R. A. Swanson, and V. L. Telegdi. Precision Experiments on Muonium. I. Determination of the Muonium Hyperfine Splitting in Low-Pressure Argon from a Field-Independent Zeeman Transition. *Physical Review A*, 5(6):2357–2375, Jun 1972.

[42] R. De Voe, P. M. McIntyre, A. Magnon, D. Y. Stowell, R. A. Swanson, and V. L. Telegdi. Measurement of the Muonium Hfs Splitting and of the Muon Moment by "Double Resonance," and a New Value of α. *Physical Review Letters*, 25(26):1779–1783, Dec 1970.

[43] P. A. Thompson, P. Crane, T. Crane, J. J. Amato, V. W. Hughes, G. z. Putlitz, and J. E. Rothberg. Muonium. IV. Precision Measurement of the Muonium Hyperfine-Structure Interval at Weak and Very Weak Magnetic Fields. *Physical Review A*, 8(1):86, Jul 1973.

[44] D. Favart, P. M. McIntyre, D. Y. Stowell, V. L. Telegdi, R. DeVoe, and R. A. Swanson. Precision Experiments on Muonium. III. Ramsey Resonance in Zero Field. *Phys. Rev. A*, 8:1195–1218, Sep 1973.

[45] D. E. Casperson, T. W. Crane, V. W. Hughes, P. A. Souder, R. D. Stambaugh, P. A. Thompson, H. Orth, G. Zu Putlitz, H. F. Kaspar, H. W. Reist, and A. B. Denison. A new high precision measurement of the muonium hyperfine structure interval . *Physics Letters B*, 59:397–400, November 1975.

[46] D. E. Casperson, T. W. Crane, A. B. Denison, P. O. Egan, V. W. Hughes, F. G. Mariam, H. Orth, H. W. Reist, P. A. Souder, R. D. Stambaugh, P. A. Thompson, and G. z. Putlitz. Erratum: New Precise Value for the Muon Magnetic Moment and Sensitive Test of the Theory of the hfs Interval in Muonium. *Physical Review Letters*, 38(17):956–959, Apr 1977.

[47] D. E. Casperson, T. W. Crane, A. B. Denison, P. O. Egan, V. W. Hughes, F. G. Mariam, H. Orth, H. W. Reist, P. A. Souder, R. D. Stambaugh, P. A. Thompson, and G. z. Putlitz. New Precise Value for the Muon Magnetic Moment and Sensitive

Test of the Theory of the hfs Interval in Muonium. *Physical Review Letters*, 38(25):1504, Jun 1977.

[48] F. G. Mariam, W. Beer, P. R. Bolton, P. O. Egan, C. J. Gardner, V. W. Hughes, D. C. Lu, P. A. Souder, H. Orth, J. Vetter, U. Moser, and G. z. Putlitz. Higher Precision Measurement of the hfs Interval of Muonium and of the Muon Magnetic Moment. *Physical Review Letters*, 49(14):993–996, Oct 1982.

[49] K. Olive et al. Review of particle physics. *Chin.Phys.*, C38:090001, 2014.

[50] N. Kawamura and A. Toyoda. H Line; A Beamline for Fundamental Physics in J-PARC. *JPS Conference Proceedings*, 2, 2014.

[51] K. P. Jungmann. Past, Present and Future of Muonium, 2004.

[52] S. Karshenboim. *The Hydrogen Atom: Precision Physics of Simple Atomic Systems (Lecture Notes in Physics)*. Springer, 2001.

[53] A. Badertscher, S. Dhawan, P. O. Egan, V. W. Hughes, D. C. Lu, M. W. Ritter, K. A. Woodle, M. Gladisch, H. Orth, G. z. Putlitz, M. Eckhause, J. Kane, F. G. Mariam, and J. Reidy. Formation of Muonium in the $2S$ State and Observation of the Lamb Shift Transition. *Physical Review Letters*, 52:914–917, Mar 1984.

[54] A. P. Mills, J. Imazato, S. Saitoh, A. Uedono, Y. Kawashima, and K. Nagamine. Generation of Thermal Muonium in Vacuum. *Physical Review Letters*, 56:1463–1466, Apr 1986.

[55] A. C. Janissen, G. A. Beer, G. R. Mason, A. Olin, T. M. Huber, A. R. Kunselman, T. Bowen, P. G. Halverson, C. A. Fry, K. R. Kendall, G. M. Marshall, and J. B. Warren. Muonium production from fine silica powder. *Physical Review A*, 42:161–169, Jul 1990.

[56] J. R. Musser, R. Bayes, Y. I. Davydov, P. Depommier, J. Doornbos, W. Faszer, C. A. Gagliardi, A. Gaponenko, D. R. Gill, P. Green, P. Gumplinger, M. D. Hasinoff, R. S. Henderson, J. Hu, B. Jamieson, P. Kitching, D. D. Koetke, A. A.

Krushinsky, Y. Y. Lachin, J. A. Macdonald, R. P. MacDonald, G. M. Marshall, E. L. Mathie, L. V. Miasoedov, R. E. Mischke, P. M. Nord, K. Olchanski, A. Olin, R. Openshaw, T. A. Porcelli, J.-M. Poutissou, R. Poutissou, M. A. Quraan, N. L. Rodning, V. Selivanov, G. Sheffer, B. Shin, F. Sobratee, T. D. S. Stanislaus, R. Tacik, V. D. Torokhov, R. E. Tribble, M. A. Vasiliev, and D. H. Wright. Measurement of the Michel Parameter ρ in Muon Decay. *Physical Review Letters*, 94:101805, Mar 2005.

[57] http://www.srim.org/.

[58] D. Pozar. *Microwave engineering*. J. Wiley, 2005.

[59] http://www.ni.com/.

[60] W. Happer. Optical Pumping. *Reviews of Modern Physics*, 44:169–249, Apr 1972.

[61] S. Ray and S. L. Kaufman. Theoretical Interpretation of the Quadratic Hyperfine Pressure Shift. *Physical Review Letters*, 29:895–898, Oct 1972.

[62] D. Casperson, T. Crane, V. Hughes, P. Souder, R. Stambaugh, P. Thompson, H. Orth, G. z. Putlitz, H. Kaspar, H. Reist, and A. Denison. A new high precision measurement of the muonium hyperfine structure interval. *Physics Letters B*, 59(4):397 – 400, 1975.

[63] K. M. Kojima, T. Murakami, Y. Takahashi, H. Lee, S. Y. Suzuki, A. Koda, I. Yamauchi, M. Miyazaki, M. Hiraishi, H. Okabe, S. Takeshita, R. Kadono, T. Ito, W. Higemoto, S. Kanda, Y. Fukao, N. Saito, M. Saito, M. Ikeno, T. Uchida, and M. M. Tanaka. New μSR spectrometer at J-PARC MUSE based on Kalliope detectors. *Journal of Physics: Conference Series*, 551(1):012063, 2014.

[64] S. Kanda and Y. Ueno and K. S. Tanaka for the MuSEUM collaboration. Development of 3D imaging of muon stopping distribution for Muonium HFS measurement. *KEK-MSL Progress Report 2014*, 2015. to be published.

[65] S. Kanda for the MuSEUM collaboration. Development of a new positron counting system with SiPM readout for muon spin spectrometers. *PoS*, PhotoDet2015, 2015. to be published.

[66] C. L. Morgan and E. S. Ensberg. Precise Hyperfine Pressure-Shift Measurements for Hydrogen Isotopes in Argon. *Physical Review A*, 7:1494–1502, May 1973.

[67] W. R. C. (Ed.). *Handbook of Chemistry and Physics (53rd Edn.)*. Springer tracts in modern physics. Chemical Rubber Company, 1972.

[68] W. Liu. *HIGH PRECISION MEASUREMENT OF MUONIUM GROUND STATE HYPERFINE INTERVAL AND MUON MAGNETIC MOMENT*. PhD thesis, Yale University, 1997.

[69] Y. I. Neronov and N. N. Seregin. Precision determination of the difference in shielding by protons in water and hydrogen and an estimate of the absolute shielding by protons in water. *Metrologia*, 51(1):54, 2014.

[70] B. W. Petley and R. W. Donaldson. The Temperature Dependence of the Diamagnetic Shielding Correction for Proton NMR in Water. *Metrologia*, 20(3):81, 1984.

[71] http://www.cobham.com/.

[72] G. A. Clarke. Effects of Helium Buffer Gas Atoms on the Atomic Hydrogen Hyperfine Frequency. *The Journal of Chemical Physics*, 36(8):2211–2216, 1962.

[73] O. Kamigaito. Circuit-model representation of external-Q calculation. *Physical Review ST Accelerators and Beams*, 9:062003, Jun 2006.

[74] D. Nomura and T. Teubner. Hadronic contributions to the anomalous magnetic moment of the electron and the hyperfine splitting of muonium. *Nuclear Physics B*, 867(2):236 – 243, 2013.

[75] M. Niering, R. Holzwarth, J. Reichert, P. Pokasov, T. Udem, M. Weitz, T. W. Hänsch, P. Lemonde, G. Santarelli, M. Abgrall, P. Laurent, C. Salomon, and A. Clairon. Measurement of the Hydrogen $1S$- $2S$ Transition Frequency by Phase Coherent Comparison with a Microwave Cesium Fountain Clock. *Physical Review Letters*, 84(24):5496–5499, Jun 2000.

[76] M. Fischer, N. Kolachevsky, M. Zimmermann, R. Holzwarth, T. Udem, T. W. Hänsch, M. Abgrall, J. Grünert, I. Maksimovic, S. Bize, H. Marion, F. P. D. Santos, P. Lemonde, G. Santarelli, P. Laurent, A. Clairon, C. Salomon, M. Haas, U. D. Jentschura, and C. H. Keitel. New Limits on the Drift of Fundamental Constants from Laboratory Measurements. *Physical Review Letters*, 92(23):230802, Jun 2004.

[77] S. G. Karshenboim. Nuclear structure-dependent radiative corrections to the hydrogen hyperfine splitting. *Physics Letters A*, 225(1-3):97 – 106, 1997.

[78] S. G. Karshenboim, S. I. Eidelman, P. Fendel, V. G. Ivanov, N. N. Kolachevsky, V. A. Shelyuto, and T. W. Hansch. Study of hyperfine structure in simple atoms and precision tests of the bound state QED. *Nucl. Phys. B, Proc. Suppl.*, 162(hep-ph/0608236):260–263, Aug 2006.

[79] D. Favart, P. M. McIntyre, D. Y. Stowell, V. L. Telegdi, R. DeVoe, and R. A. Swanson. Quadratic hfs Pressure Shifts of Muonium in Argon and Krypton. *Physical Review Letters*, 27(20):1340–1342, Nov 1971.

[80] H. G. E. Kobrak, R. A. Swanson, D. Favart, W. Kells, A. Magnon, P. M. McIntyre, J. Roehrig, D. Y. Stowell, V. L. Telegdi, and M. Eckhause. A new precision measurement of the muonium hyperfine interval in argon. *Physics Letters B*, 43(6):526 – 528, 1973.

[81] S. Karshenboim. Simple Atoms, Quantum Electrodynamics, and Fundamental Constants. In *Precision Physics of Simple Atomic Systems*, volume 627 of *Lecture*

Notes in Physics, pages 141–162. Springer Berlin / Heidelberg, 2003. 10.1007/978-3-540-45059-7-8.

[82] F. Jegerlehner and A. Nyffeler. The muon. *Physics Reports*, 477(1-3):1 – 110, 2009.

[83] S. G. and Karshenboim. Precision physics of simple atoms: QED tests, nuclear structure and fundamental constants. *Physics Reports*, 422(1-2):1 – 63, 2005.

[84] P. J. Mohr, B. N. Taylor, and D. B. Newell. CODATA recommended values of the fundamental physical constants: 2006. *Journal of Physical and Chemical Reference Data*, 37(3):1187–1284, 2008.

[85] http://www.fieldp.com/.

[86] http://www.autodesk.com/.

[87] Industrial platinum resistance thermometers and platinum temperature sensors, 2008.

[88] R. S. Van Dyck, P. B. Schwinberg, and H. G. Dehmelt. New high-precision comparison of electron and positron g factors. *Physical Review Letters*, 59:26–29, Jul 1987.

[89] P. J. Mohr, B. N. Taylor, and D. B. Newell. CODATA recommended values of the fundamental physical constants: 2006. *Reviews of Modern Physics*, 80:633–730, Jun 2008.

[90] S. G. Karshenboim. Precision Physics of Simple Atoms and Constraints on a Light Boson with Ultraweak Coupling. *Physical Review Letters*, 104:220406, Jun 2010.

[91] S. Kanda for the MuSEUM collaboration. Development of online muon beam profile monitor for the MuSEUM experiment. *RIKEN Accelerator Progress Report 2014*, 2015.

[92] D. Ciskowski, H. Ahn, R. Dixson, X. Fei, V. Hughes, B. Matthias, C. Pillai, and K. Woodle. A chopped high intensity muon beam at the Stopped Muon Channel at LAMPF. *Nuclear Instruments and Methods in Physics Research Section A: Accelerators, Spectrometers, Detectors and Associated Equipment*, 333(23):260 – 264, 1993.

Acknowledement

修士課程から博士課程に渡り、様々な機会でご指導くださった松田恭幸先生に感謝を致します。また、ミュオニウムの超微細構造という魅力的な研究の機会を与えてくださった高エネルギー加速器研究所の下村浩一郎先生に感謝致します。

山崎泰規先生には修士 1 年次の CERN における実験における研究の機会を与えてくださり、基礎物理に対して志すきっかけとなりました。研究室の鳥居寛之先生には、普段の研究生活を含めたあらゆる面においてご指導いただき、本論文執筆にあたっても貴重な助言を多くいただきました。黒田直史先生には修士 1 年次の CERN における実験において実験から生活面に関してご指導いただきました。理化学研究所岩崎先端中間子研究室の岩崎雅彦先生には博士課程 3 年次より理研の JRA として研究を行う機会を与えてくださり、本研究に打ち込むことができました。石田勝彦先生には本研究の計画段階からたくさんの助言をくださり、大いに励みになりました。

理化学研究所仁科センターの上垣外修一先生、坂本成彦先生、須田健嗣先生には CST microwave studio を使わせていただき、RF キャビティの性能評価のために修士 2 年次にネットワークアナライザ及び実験室をお貸ししていただきました。

本実験の共同研究者である齊藤直人博士、三部勉博士、佐々木憲一博士、豊田晃久博士、David Kawall 博士、Patrick Strasser 博士、深尾祥紀博士は装置開発から実験計画まで多岐にわたって様々な助言を下さりました。小嶋健児博士、幸田章宏博士、河村成肇博士、三宅康博博士にはビーム実験において多大なサポートをしてくださり MLF 施設における実験を円滑に進めることができました。神田聡太郎君、水谷丈洋君、上野恭裕君、東芳隆君は本実験において共同開発を行い多くの場面で助けてもらいました。

高エネルギー加速器研究機構加速器部門の吉田光宏博士、佐藤大輔氏にはゼロ磁場実験用の信号発生器やネットワークアナライザをお貸しいただき、強磁場実験と相補

的にゼロ磁場実験を行うというアイデアを進めることができました。

本テーマではありませんが、修士 1 年次の CERN においては、檜垣浩之先生、永田祐吾博士、榎本嘉範博士、満汐孝治博士には多くのことを教えていただき、本テーマをすすめる上で大きな基礎となりました。

私の研究室の同期にあたる大塚未来さん、藤居甲基君は研究室の様々な場面で支えあってきた仲間であり、大変感謝しています。

また、東京大学総合文化研究科山崎松田研究室の皆さま、高エネルギー加速器研究所の皆さま、理化学研究所の皆さまの他、多くの人々の助けによってこのように博士論文をまとめることができました。厚くお礼申しあげます。

最後に経済的にも精神的にも集中して研究する環境を支えてくれた家族に感謝します。